INTERNATIONAL CENTER FOR AGGREGATES RESEARCH

ICAR

STRUCTURAL CHARACTERISTICS OF UNBOUND AGGREGATE BASES TO MEET AASHTO 2002 DESIGN REQUIREMENTS: INTERIM REPORT

RESEARCH REPORT ICAR - 502-1

Sponsored by the
Aggregates Foundation
for Technology, Research and Education

Technical Report Documentation Page

1. Report No. ICAR/502-1	2. Government Accession No.	3. Recipient's Catalog No.
4. Title and Subtitle STRUCTURAL CHARACTERISTICS OF UNBOUND AGGREGATE BASES TO MEET AASHTO 2002 DESIGN REQUIREMENTS: INTERIM REPORT		5. Report Date July 2001 6. Performing Organization Code
7. Author(s) Alex Adu-Osei, Dallas N. Little, and Robert L. Lytton		8. Performing Organization Report No. Report No. 502-1
9. Performing Organization Name and Address Texas Transportation Institute The Texas A&M University System College Station, Texas 77843-3135		10. Work Unit No. (TRAIS) 11. Contract or Grant No. Project No. 404001
12. Sponsoring Agency Name and Address Aggregates Foundation for Technology, Research, and Education 2101 Wilson Blvd, Suite 100 Arlington, VA 22201-3062		13. Type of Report and Period Covered Interim July 2001 14. Sponsoring Agency Code

15. Supplementary Notes
Research performed in cooperation with International Center for Aggregates Research and Aggregates Foundation for Technology, Research, and Education.
Research Project Title: Structural Characteristics of Unbound Aggregate Bases to Meet AASHTO Design Requirements

16. Abstract

This report gives the results of a study of the properties of unbound aggregate base materials using both laboratory testing data from full scale field tests in Illinois, Georgia, and Texas, and a model of cross-anisotropic elastic materials to characterize the behavior of the base materials under traffic loads. Using the cross-anisotropic model, the stress distribution in a base course is more realistic than that developed when the aggregate base is considered to be linear and isotropic. The stress distribution based on cross-anisotropic analysis is not only more correct, but it is also more favorable to the unbound aggregate in that significant tensile stresses are found not to occur. The analogy is presented in this report that the response of the aggregate base to the load is as if the stress distribution directly under the wheel load due to anisotropy acts as a moving column under the wheel in which the aggregate essentially produces its own confinement and does not enter into tension. Other findings in this report include the following:

- The unbound aggregate base material should be modeled as non-linear and cross-anisotropic to account for stress-sensitivity and the significant differences between vertical and horizontal moduli and Poisson's ratios.
- The ICAR laboratory testing protocol is efficient and precise and should be considered as a candidate to model the unbound aggregate base. The protocol uses three stress regimes and ten stress levels within each regime to determine stress sensitivity and cross-anisotropy. A system identification method is used to select the five material properties based on the tests results necessary to properly characterize the aggregate base and to satisfy the requirements of elastic work potential theory.
- The Fast Industrial Process Controls cell is efficient and should be used to characterize unbound aggregate bases. The ratio of the diameter to the specimen height is 1:1. While testing of such sample sizes is discouraged in the literature, improvements made to the IPC cell minimize frictional development between the sample and loading platens resulting in minimal constraint at the sample ends. This is verified in the report based on comparative triaxial testing and finite element analysis.
- The ICAR testing protocol is an excellent tool for both unbound aggregate characterization and comparative analysis of materials. A compaction study on two very different aggregates (uncrushed river gravel and crushed limestone) was performed in which the aggregates were subjected to impact, kneading gyratory compaction. The difference in the tendency of the compaction techniques to produce varying levels of particle orientation (which affects anisotropy) was evident in the degree of anisotropy measured.

17. Key Words Cross-anisotropic, Unbound Granular Materials, Resilient Modulus,	18. Distribution Statement No restrictions. This document is available to the public through NTIS: National Technical Information Service 5285 Port Royal Road Springfield, Virginia 22161		
19. Security Classif.(of this report) Unclassified	20. Security Classif.(of this page) Unclassified	21. No. of Pages	22. Price

Form DOT F 1700.7 (8-72) **Reproduction of completed page authorized**

STRUCTURAL CHARACTERISTICS OF UNBOUND AGGREGATE BASES TO MEET AASHTO 2002 DESIGN REQUIREMENTS: INTERIM REPORT

by

Alex Adu-Osei
Graduate Research Assistant
Texas A&M University

Dallas N. Little
Senior Research Fellow
Texas A&M University

and

Robert L. Lytton
Research Engineer
Texas A&M University

Report No 502-1

Project No. 404001
Research Project Title: Structural Characteristics of Unbound Aggregate Bases to Meet AASHTO Design Requirements

Sponsored by
Aggregates Foundation for Technology, Research, and Education

July, 2000

Texas A&M University
TEXAS TRANSPORTATION INSTITUTE
College Station, Texas 77840
MS 3135

TABLE OF CONTENTS

TABLE OF CONTENTS (CON'T)

TABLE OF CONTENTS (CON'T)

Page

LIST OF TABLES

LIST OF TABLES (Cont)

LIST OF TABLES (Cont)

Table **Page**

LIST OF TABLES (Cont)

Table **Page**

LIST OF FIGURES

LIST OF FIGURES (Cont)

LIST OF FIGURES (Cont)

Figure **Page**

LIST OF FIGURES (Cont)

Figure **Page**

LIST OF FIGURES (Cont)

Figure **Page**

LIST OF FIGURES (Cont)

Figure **Page**

FINDINGS

1. The unbound aggregate base material should be modeled as non-linear and cross-anisotropic to account for stress-sensitivity and the significant differences between vertical and horizontal moduli and Poisson's ratios.
2. The ICAR laboratory testing protocol is efficient and precise and should be considered as a candidate to model the unbound aggregate base. The protocol uses three stress regimes and ten stress levels within each regime to determine stress sensitivity and cross-anisotropy. A systems identification method is used to select the five material properties based on the test results necessary to properly characterize the aggregate base and to satisfy the requirements of elastic work potential theory.
3. The ICAR laboratory testing protocol is an accurate representation of the stress state under a moving wheel load. However, the stress excursions are small in order to keep principal stress ratios relatively constant. It will be important to compare resilient properties and cross-anisotropic effects at larger stress excursions. This will be done in the final report.
4. The Fast IPC cell is efficient and should be used to characterize unbound aggregate bases. The sample size is currently 1:1 (ratio of diameter to specimen height). While testing of such sample sizes is discouraged in the literature, improvements made to the IPC cell minimize frictional development between the sample and loading plattens resulting in minimal constrain at the sample ends and therefore minimal zones of interference with the failure plane. This is verified in the report based on comparative triaxial testing and finite element analysis.
5. The ICAR testing protocol is an excellent tool for both unbound aggregate characterization and comparative analysis of materials. A compaction study on two very different aggregates (uncrushed river gravel and crushed limestone) was performed in which the aggregates were subjected to impact, kneading gyratory compaction. The differences in the tendency of the compaction techniques to produce varying levels of particle orientation (which affects anisotropy) was evident in the degree of anisotropy measured.

ADDITIONAL WORK TO BE ADDRESED IN THE FINAL REPORT

The final report will address the following additional issues:

1. Performance of selected pavement sections.
2. Modeling of Stockbridge pavement sections.
3. Modeling of TTI pavement sections.
4. A permanent deformation or rutting model for the unbound, granular base.
5. Overall recommendations for characterization and implementation of cross-anisotropy into the AASHTO 2002 Pavement Design Guide.
6. Evaluation of test parameters under larger stress excursions.

Performance of Selected Sections

Data have been collected on the performance of pavement sections in Table 1. These data will be summarized in the final report.

Table 1. Performance Data on Selected Sections

Site	Data Available	Importance and Reasons for Consideration
Gulf Cost Division - Tampa Area	• Comparison of Brooksville and Calica crushed limestone • FWD data obtained on field sections • Typical aggregate properties, gradations and LBR data	• Consider additional field testing as warranted to supplement existing data including seismic surface wave analysis (SASW) and rolling FWD
Southwest Division - Corpus Christi and Pharr County	• Comparison of Calica limestone, Caliche and Lime Rock Asphalt • Extensive materials characterization including: gradation, CBR, triaxial and resilient modulus • FWD data but not complete	• Seek additional information from Irv Dukatz and Chen Fu • Plan to perform SASW and rolling FWD
Livingston County Granular Base Study (Illinois)	• FWD data and backcalculations • Traffic data • Rut depth and crack survey data • Clegg hammer test data • Dynamic cone penetrometer (DCP) data • Aggregate properties • Construction data • Report (1991) by Lippert, Schutzbach and Lyons	• Excellent source of material properties and performance monitoring • Supplement with SASW and rolling FWD testing
Laraway Quarry Entrance (Illinois)	• Deflection testing by IDOT (FWD) • Detailed information on construction • Greater than 50% of aggregate larger than 2- inches	• Excellent case history for large stone base • Use cooperation of IDOT • Perform SASW, Triaxial testing and rolling
Stockbridge (Georgia)	• Heavy truck traffic • 21-inch thick UAB • Thin hot mix asphalt (HMA) surface • Low fines content (about 1.9%) • History of traffic • Report by Dr. Barksdale	• Supplement with additional test data: triaxial, SASW and rolling FWD
GPS Sites	• Reassess GPS sites for available data • Concentrate on Texas locations	• Utilize existing information
Siler City Test Site	• Extensive report exists which has been reviewed by ICAR	• Maintain contact with North Carolina DOT and North Carolina State University on this project • Excellent comparison of various pavement sections including the effect of stabilized subgrades on the UAB

Stockbridge Sections

This interim report documents the development of a methodology to characterize the cross-anisotropic nature of unbound aggregate base materials. This report explains the difference such a characterization makes in terms of stress distribution within the aggregate base. The stress distribution is more realistic than that developed when the aggregate base is considered to be linear and isotropic. The stress distribution based on cross-anisotropic analysis is not only more correct, but it is also more favorable to the unbound aggregate in that significant tensile stresses do not occur. Such tensile stresses can not be accommodated by an aggregate base, and therefore a compensating adjustment is required. The analogy is presented in this report that the response of the aggregate base to the load is as if the stress distribution directly under the wheel load due to anisotropy acts as a moving column under the wheel in which the aggregate essentially produces its own confinement and does not enter into tension.

The final report will employ the cross anisotropic characterization protocol established in this interim report. We will test an aggregate blend placed at Stockbridge, Georgia, in 1978 on a quarry haul road. The haul road was instrumented and a report on the stresses induced under loading as measured by the instrumentation is documented in a report entitled, "A Study of Factors Affecting Crushed Stone Base Performance". This report is authored by Barksdale and Todres. Samples of the Stockbridge aggregate are now being tested at TTI. The cross-anisotropic properties of the aggregate will be input into both TTI-Pave and GTPAVE and both finite element programs will be used to predict stresses and strains within the Stockbridge pavement section as modeled in the two programs. These results will be compared to the in situ measurements recorded in the Stockbridge report of Barksdale et al. The Stockbridge aggregate will also be characterized as isotropic in the conventional manner prescribed by AASHTO T-294. The finite element models will compare predicted stress and strain parameters for both characterization methods: isotropic and cross-anisotropic.

TTI Sections

TTI built test sections in 1997 with a thin asphalt surface and a thick asphalt surface layer. The base course in each pavement is a crushed Texas limestone meeting TxDOT Grade 1, Item 248, aggregate base specifications. These test sections were instrumented with multi-depth deflectometers (MDD's). A Falling Weigh Deflectometer (FWD) was positioned directly over the MDD and at several different positions away from the MDD. The limestone will be characterized in the laboratory according to the ICAR protocol. The results will be input into GTPAVE, TTIpave, and CIRCLY and deflections will be calculated and compared to the MDD data recorded under the FWD at the test sites. This will allow us to evaluate the ability of each of these models to predict deflections within the region of influence of the applied load. Of particular interest will be the comparison of accuracy of deflection prediction of linear elastic isotropic (using a program such a ELSYM5), non-linear elastic isotropic (using a layered elastic program such as KENLAYER and a non-linear finite element program such as either GTPAVE or TTIpave), and non-linear cross-anisotropic systems. In the non-linear cross-anisotropic group, we will consider CIRCLY which, although it has the ability to account for both cross-anisotropy and non-linearity, cannot account for lateral stress-sensitivity as it is a layered elastic model. On the contrary, both GTPAVE and TTIpave can account for cross-anisotropy and stress-sensitivity (both vertical and lateral).

Layered Elastic - Cross Anisotropic Surrogate Model

We understand that the NCHRP 1-37A design team will, in all probability, go with a layered elastic pavement structural model in lieu of a more complex finite element model. Since this research demonstrates the importance of cross-anisotropy to the accuracy of the analysis of unbound aggregate bases and to the manner in which these bases are viewed based on predicted performance, it is important to model the anisotropic response. Fortunately, a layered elastic structural model developed by the Australian Road Research Board (1986) called CIRCLY allows cross-anisotropic modeling of aggregate layers. ICAR has obtained CIRCLY and its source code and will use CIRCLY to model the Stockbridge sections. Results will be compared with linear elastic isotropic and finite element models. ICAR is also looking into modifying CIRCLY to accommodate permanent deformation.

Three-Parameter Permanent Deformation Model

The final report will introduce a three-parameter model of permanent deformation damage which has been developed at TTI. This model characterizes the strain-hardening nature of stable aggregate and stable asphalt mixtures as a hyperbolic relationship in which the rate of accumulated strain decreases with load cycles until it ultimately becomes asymptotic to certain level. This model was tested against the conventionally accepted VESYS model (Kenis, 1978) for aggregate bases in a field trial in which the roadway was subjected to accelerated loading with the Texas Department of Transportation's (TxDOT's) Mobile Loading Simulator (MLS). The MLS results showed the superior ability of the three-parameter model to predict permanent deformation damage. ICAR has modified the three-parameter model to account

for the effects of moisture on mixture stability through the incorporation of a matrix suction term. The three-parameter damage model with the matrix suction term can be incorporated into the TTI-Pave. Therefore, the complete pavement model of the aggregate base layer will be a finite element model which accommodates both cross-anisotropic resilient behavior and permanent deformation damage as defined by the three-parameter model.

Evaluation of Test Parameters under Large Stress Excursions

The ICAR test protocol discussed in this report is based on small stress excursions around a closely controlled constant stress state. We believe that this is the most accurate and realistic approach. However, some may argue that the stress path under a moving wheel load is more realistically depicted by larger stress excursions. Therefore, selected experiments will be repeated under larger stress excursions and the data will be analyzed and compared in volume II.

BACKGROUND

Unbound granular materials are multi-phase materials comprised of aggregate particles, air voids and water. The mathematical characterization of unbound granular materials should ideally be based on the behavior of the individual constituent elements and their interaction. This calls for the use of particulate mechanics. However, such an approach can be rather complex and is not particularly suitable in pavement engineering applications. As faster computers become available, particulate mechanics becomes a more suitable means to characterize the behavior of unbound granular materials. Also, since the scale of practical interest is in the range of tens to hundreds of feet, the microscopic effects of unbound granular materials can be averaged and treated as a continuum.

The mechanical behavior of unbound granular materials, like soils, is influenced by factors such as density, stress history, void ratio, temperature, time, and pore water pressure. It is difficult to adequately incorporate these factors in a simple mathematical model and then to implement the model realistically into a computer-based numerical analysis, within the framework of continuum mechanics. The model developed for this project is based on the generalized Hooke's law of elasticity. It is further assumed that unbound granular materials are hyperelastic and thus their behavior satisfies the energy requirements of thermodynamics. The stress state dependent behavior of unbound granular materials can then be introduced into the generalized elasticity model to form the bases for a numerical analysis of a pavement under traffic load.

CONSTITUTIVE MODEL

For a linear, elastic, homogeneous and continuous material, the general constitutive relation relating stress and strain tensors can be written as:

$$\sigma_{ij} = C_{ijkl}\varepsilon_{kl} \qquad (1)$$

Where:

σ_{ij} = stress tensor;

C_{ijkl} = tensor of elastic constants; and

ε_{ij} = strain tensor.

Repeated indices imply summation. Indices i, j, k take the values 1, 2, 3.

In the most general three-dimensional case, the tensor of elastic constants C_{ijkl} has 81 independent components. However, due to the symmetry of both the strain and stress tensors, there are at most 36 distinct elastic constants. This number is reduced to 21 if the existence of a strain energy function is further assumed. Equation 1 can be rewritten as:

$$\varepsilon_{ij} = A_{ijkl}\sigma_{kl} \tag{2}$$

where:

A_{ijkl} = a tensor of compliance with 21 distinct components, and

A_{ijkl} and C_{ijkl} are symmetric and are inverse to each other in the sense that;

$$C_{ijkl}A_{klrs} = \frac{1}{2}(\delta_{ir}\delta_{js} + \delta_{is}\delta_{jr}) \tag{3}$$

where δ_{ij} is the Kronecker Delta.

If we consider the matrix representation of the tensor ε_{ij}, σ_{kl}, and A_{ijkl} in an arbitrary x, y, z coordinate system, Equation 2 is equivalent to:

$$\varepsilon_{xyz} = [A]\{\sigma\}_{xyz} \tag{4}$$

or

$$\begin{bmatrix} a_{ij} \\ i = 1, 6 \\ j = 1, 6 \end{bmatrix} \begin{Bmatrix} \sigma_x \\ \sigma_y \\ \sigma_z \\ \tau_{yz} \\ \tau_{xz} \\ \tau_{xy} \end{Bmatrix} = \begin{Bmatrix} \varepsilon_x \\ \varepsilon_y \\ \varepsilon_z \\ \gamma_{yz} \\ \gamma_{xz} \\ \gamma_{xy} \end{Bmatrix} \tag{5}$$

The coefficients a_{ij} play different roles and have different physical meanings.

If the material possesses symmetry of any kind, then symmetry can be observed in its elastic properties and the number of independent components of the tensor of compliance or elastic constants is less than 21.

Orthogonal Planes of Elastic Symmetry

A plane of elastic symmetry exists at a point if the elastic constants or compliance have the same values for every pair of coordinate systems that are the reflected image of one another with respect to the plane. Assuming that the Cartesian xOz plane (Figure 1)

is a plane of elastic symmetry and assuming that three orthogonal planes of elastic symmetry pass through each point of the material, and each one is perpendicular to x, y, or z, then Equation 5 reduces to:

$$\begin{bmatrix} \frac{1}{E_x} & -\frac{\nu_{xy}}{E_y} & -\frac{\nu_{xz}}{E_z} & 0 & 0 & 0 \\ & \frac{1}{E_y} & -\frac{\nu_{zy}}{E_z} & 0 & 0 & 0 \\ & & \frac{1}{E_z} & 0 & 0 & 0 \\ & & & \frac{1}{G_{zy}} & 0 & 0 \\ & & & & \frac{1}{G_{xz}} & 0 \\ & & & & & \frac{1}{G_{xy}} \end{bmatrix} \begin{Bmatrix} \sigma_x \\ \sigma_y \\ \sigma_z \\ \tau_{zy} \\ \tau_{xz} \\ \tau_{xy} \end{Bmatrix} = \begin{Bmatrix} \varepsilon_x \\ \varepsilon_y \\ \varepsilon_z \\ \gamma_{zy} \\ \gamma_{xz} \\ \gamma_{xy} \end{Bmatrix} \qquad (6)$$

The number of independent elastic constants or compliance is reduced to 9. There are three Young's moduli E_x, E_y, E_z, three shear moduli G_{yz}, G_{xz}, G_{xy}, and three Poisson's ratios ν_{yx}, ν_{zx}, and ν_{zy}. A material that possesses this type elastic symmetry is called orthotropic.

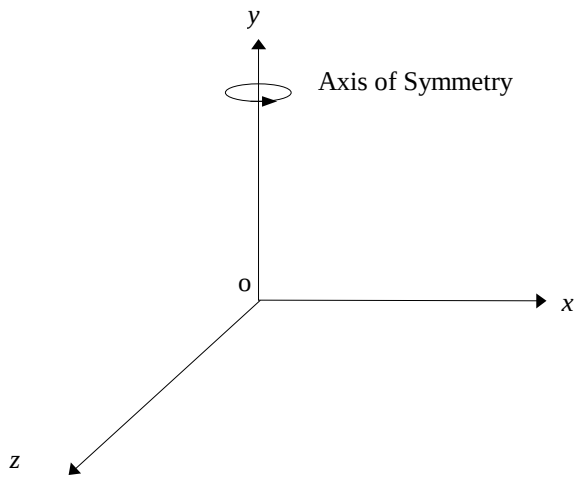

Figure 1. Three-Dimensional Cartesian Coordinate System.

An axis of elastic symmetry *g* of order *n* exists at a point when there are sets of equivalent elastic directions that can be superimposed by a rotation through an angle of $2\pi/n$. An axis of the second order is equivalent to a plane of elastic symmetry. For an axis of the third or fourth order, the number of independent elastic constants or compliances is reduced to 7. For an axis of order larger than or equal to 6, all directions in the planes normal to it are equivalent with respect to the elastic properties. If the y-axis coincides with the axis of elastic symmetry *g*, the material is isotropic within the *x*O*z* plane. The y-axis is defined as axis of radial elastic symmetry or axis of elastic symmetry of rotation. A material with this type of elastic symmetry is called transversely isotropic or cross-anisotropic. Unbound granular materials in pavements can be assumed to possess this type of elastic symmetry. The plane *x*O*z* and each plane perpendicular to it are planes of elastic symmetry. Thus, the number of elastic constants is reduced to 5 as follows:

$$\begin{bmatrix} \frac{1}{E_x} & -\frac{\nu_{xy}}{E_x} & -\frac{\nu_{xx}}{E_x} & 0 \\ & \frac{1}{E_y} & -\frac{\nu_{xy}}{E_x} & 0 \\ & & \frac{1}{E_x} & 0 \\ & & & \frac{1}{G_{xy}} \end{bmatrix} \begin{Bmatrix} \sigma_x \\ \sigma_y \\ \sigma_x \\ \tau_{xy} \end{Bmatrix} = \begin{Bmatrix} \varepsilon_x \\ \varepsilon_y \\ \varepsilon_x \\ \gamma_{xy} \end{Bmatrix} \tag{7}$$

where:

E_y = vertical elastic modulus,

E_x = horizontal elastic modulus,

G_{xy} = shear modulus,

ν_{xy} = vertical Poisson's ratio, and

ν_{xx} = horizontal Poisson's ratio.

The elastic constants have ranges of possible variation that are limited since thermodynamic considerations require that the strain energy be positive. The strain energy is given by:

$$\Omega = \frac{1}{2}\{\sigma\}^T{}_{xyz}[A]\{\sigma\}_{xyz} \tag{8}$$

If this quadratic form is positive definite, the strain energy will be positive as required by thermodynamics. The following conditions must be satisfied (Pickering, 1970):

$$E_y > 0 \quad ; \quad E_x > 0 \quad ; \quad G_{xy} > 0 \quad ; \quad -1 \le \nu_{xx} \le 1 \qquad (9)$$

The constitutive relations defined by Equations 1 or 2 together with the elastic symmetries can be used to model the response of unbound granular layers in pavements. The unbound granular layers which are assumed to be homogeneous, continuous transversely isotropic, thus need 5 elastic independent parameters to fully describe their behavior in pavements. Two parameters, Poisson's ratio and a modulus are needed if the material is assumed to be isotropic.

Anisotropic Work Potential

The elastic work per unit volume (dW) can be expressed as:

$$\oint dW = \oint (\sigma)^T (d\varepsilon) \qquad (10)$$

The law of energy conservation requires that the total work be path independent and Equation 10 can also be written as:

$$\oint dW = \oint \frac{I_1 dI_1}{9E_y}\left[1 + 2\frac{E_y}{E_x} - 4\nu_{xy}\frac{E_y}{E_x} - 2\nu_{xx}\frac{E_y}{E_x}\right] + \frac{dJ_2^{/}}{2G_{xy}} = 0 \qquad (11)$$

According to Green's theorem this can be written as:

$$\oint (P dx + Q dy) = \iint_A \left(\frac{dQ}{dx} - \frac{dP}{dy}\right) dA \qquad (12)$$

where:

$P = dW/dx$, and

$Q = dW/dy$.

The work potential can thus be written as:

$$dW = \frac{dW}{dI_1} dI_1 + \frac{dW}{dJ_2^{/}} dJ_2^{/} = 0 \qquad (13)$$

where:

$$\frac{dW}{dI_1} = \frac{I_1}{9E_y}\left[1 + 2\frac{E_y}{E_x} - 4\nu_{xy}\frac{E_y}{E_x} - 2\nu_{xx}\frac{E_y}{E_x}\right] \qquad (14)$$

and,

$$\frac{dW}{dJ_2^{/}} = \frac{1}{2G_{xy}} \tag{15}$$

But,

$$\frac{d^2W}{dI_1 dJ_2^{/}} = \frac{d^2W}{dJ_2^{/} dI_1} \tag{16}$$

These set of equations will be needed to obtain the five parameters which fully describe the anisotropic behavior of unbound granular materials. The five elastic properties are assumed to be stress dependent.

The Behavior of Unbound Granular Layers in Pavements

The mechanical behavior of unbound granular layers in pavements is complex. A granular layer is particulate, not a continuous medium. The response of an element of granular material in a pavement depends on its stress history, the current stress state, and the degree of saturation.

Granular materials are not elastic but experience some non-recoverable deformation after each load application. In the case of transient loads and after the first few load applications, the increment of non-recoverable deformation is much smaller compared to the increment of resilient/recoverable deformation. The term "resilient" has a precise meaning. It refers to that portion of the energy that is put into a material while it is being loaded that is completely recovered when it is unloaded. This resilient behavior of granular layers is the main justification for using elastic theory to analyze their response to traffic loads. The engineering parameter generally used to characterize this behavior is resilient modulus (M_R). The resilient modulus is defined as the ratio of the repeated axial deviator stress to the recoverable strain. It is obtained from repeated load triaxial tests, and is expressed as:

$$M_R = \frac{\sigma_d}{\varepsilon_r} \tag{17}$$

where:

M_R is the resilient modulus;

σ_d is the applied repeated deviator stress; and

ε_r is the axial recoverable strain.

Conventional flexible pavements are usually analyzed as elastic layered systems resting on a homogeneous semi-infinite half-space. The wheel load applied on the surface of the pavement is considered as a uniform load distributed over a circular area where the contact pressure is taken as the tire pressure. The development of the elastic layered system solution began when Boussinesq (1885) solved for the stress, strain and displacement in a semi-infinite linear elastic homogeneous half-space due to a point load acting on the surface. Foster and Ahlvin (1958) integrated Boussinesq's point load solution over a uniformly distributed circular area for use in flexible pavement analysis. Charts were developed for determining vertical stress, radial stress, tangential stress, shear stress, and vertical strain in the semi-infinite half-space by assuming the half-space to be incompressible with a Poisson's ratio of 0.5. This work was later refined by Ahlvin and Ulery (1962) who presented a series of equations and tables to compute the stresses and strains for any given Poisson's ratio.

A conventional flexible pavement usually consists of an asphalt concrete layer on an unbound granular material base and/or subbase, which rests on a subgrade or foundation. Burmister (1943) developed a true elastic layered theory for a two-layer system and then extended it to a three-layer system (Burmister, 1945). With the advent of computers, the theory can be applied to a multilayer system with any number of layers with specified moduli and Poisson's ratios.

Several computer programs based on Burmister's layered elastic theory have been developed over the years for analyzing pavement systems. The earliest and the best known is the CHEVRON program develop by the Chevron Research Company (Warren and Dieckmann, 1963). The program was modified by the Asphalt Institute in the DAMA program to account for non-linear elastic behavior of granular materials (Hwang and Witczak, 1979). Another well-publicized program is BISAR developed by Shell, which considers not only vertical loads but also horizontal loads (De Jong *et al*., 1973). The University of California, Berkeley (Kopperman *et al*., 1986) also developed a program called ELSYM5. This program has become very popular in the U.S. and is used by many highway agencies for routine flexible pavement design. A recent addition to the layered elastic computer programs is CIRCLY (Wardle *et al*., 1986). The latest version,

CIRCLY4 was programmed in a windows environment, and it can automatically divide layers into sub-layers for material non-linearity. It is the only layered elastic computer program that incorporates granular material anisotropy.

Linear elastic analysis can be used with reasonable confidence for pavements to model and evaluate asphalt (full depth) pavements comprised of multiple asphalt layers, but it is inappropriate for unsurfaced or thinly surfaced flexible pavements unless the nonlinear behavior can be approximated. A full depth bituminous pavement can be assumed to behave in an elastic manner. Conversely, when the pavement response to load is dominated by the resilient properties of the granular materials, their non-linear characteristics must be properly taken into account. The limitation of the layered elastic model is that elastic moduli must be constant within each horizontal layer and thus, the method cannot effectively deal with material non-linearity exhibited by unbound granular materials. To account for the non-linear behavior of granular material, the granular layer(s) are divided into sub-layers to account for variations in resilient modulus caused by the changes in stresses which occur with depth as a result of both traffic and overburden loads. The resilient moduli of the sub-layers are adjusted by iteration until the moduli are compatible with the computed stresses. There are different sub-layering methods available for assigning moduli to granular materials. The sub-layering methods depend on the design method or pavement structure and are totally different from each other. The most widely used ones are the US Army Corps of Engineers method, the Shell Pavement Design (Shell, 1985), and the Austroads Design Guide (1987) methods. The layered elastic process can account for variation in vertical stress through the iteration approach but cannot effectively account for variation in lateral stresses. Since the variation of lateral stresses within a pavement profile is as important as the variation of vertical stresses, the finite element method (FEM) has recently been preferred to analyze pavements.

A number of computer programs have been developed based on the finite element method which most completely accommodates nonlinear stress-strain models. Due to the large amount of computer time and storage required of most finite element method programs, they have not been used for routine design purposes. With the advent of faster

and larger memory computers, it has become possible to use finite element method programs to analyze pavements on personal computers.

A practical nonlinear description of the resilient modulus of unbound granular layers was reported by Hicks and Monismith (1971) and implemented in the 1993 AASHTO Guide for the Design of Pavement Structures. The resilient modulus was described realistically as depending upon the level of the mean principal stresses as expressed by Equation 18.

$$M_R = k\theta^n \tag{18}$$

where:

θ = the mean principal stress (I_1), and

k, n = material properties.

Subsequently, further research work by Uzan (1985) and Witczak and Uzan (1988) and others showed that the resilient modulus also depends upon the shearing stress level as expressed in Equation 19. This added condition can be used to explain why unbound granular layers become less stiff in areas of high shearing stresses such as at the edge of tire loading.

$$M_R = k_1\left(\frac{I_1}{P_a}\right)^{k_2}\left(\frac{\tau_{oct}}{P_a}\right)^{k_3} \tag{19}$$

where:

τ_{oct} = octahedral shear stress,

P_a = atmospheric pressure, and

k_1, k_2, and k_3 = material properties.

ANISOTROPY

The word anisotropy is a synthesis of the Greek words *anisos*, which means unequal, and *tropos*, which means manner. As the derivation of the word indicates, it means in general a different (unequal) manner of response. The mechanical properties of an anisotropic elastic material depend on direction.

The behavior of granular layers, like most geologic materials, depends on particle arrangement which is usually determined by aggregate characteristics, construction methods, and loading conditions. An apparent anisotropy is induced in an unbound

granular layer during construction, becoming stiffer in the vertical direction than in the horizontal direction even before traffic loads impose further anisotropy. Tutumuluer and Thompson (1996) indicated that the non-linear anisotropic approach can effectively account for the dilative behavior of unbound granular layers observed under wheel loads and the effects of compaction induced residual stresses. The main advantage of using anistropic modeling in unbound granular layers is the drastic reduction or elimination of significant tensile stresses generally predicted by using an isotropic approach.

An unbound granular layer in a flexible pavement provides load distribution through aggregate interlock. The load transfer is achieved through compression and shear forces among the particles. Because tensile forces can not be transferred from particle to particle, when such forces act in the horizontal direction, the behavior of the granular layer is significantly affected by a directional dependency of material stiffness which can be accommodated by using an anisotropic approach.

Barksdale, Brown and Chan (1989) observed from instrumented test sections that linear cross-anisotropic modeling of unbound granular base is equal to or better than more complicated nonlinear isotropic models for predicting general pavement response. A cross-anisotropic representation has different material properties in the vertical and horizontal directions. The conventional isotropic models have the same material properties in all directions.

Tutumluer (1995) developed a finite element computer program (GT-PAVE) to predict the resilient response of flexible pavements. The program accounts for:

- material non-linearity,
- horizontal residual stresses due to initial compaction, and
- correction of tensile stresses at the bottom of unbound granular layers obtained in isotropic elastic analysis.

Finite element predictions of response variables such as stress, strain, and deformation at different locations in the pavement were compared to the results obtained from experiments with full-scale test sections. The comparison showed very good agreement when a non-linear elastic analysis is performed with cross-anisotropic material behavior in the unbound granular layers.

A cross-anisotropic representation of the unbound granular layers was shown to reduce the predicted tensile stresses from isotropic elastic analysis in these layers by up to 75%. Tutumluer observed that it was necessary to reduce the horizontal resilient modulus to 15% of the vertical modulus in order to correctly predict the horizontal and vertical measured strain in the unbound granular base. A constant Poisson's ratio was assumed for the analysis.

Porter et. al.(1999) characterized granular layers as cross-anisotropic in the CIRCLY computer program and observed that measured deflection bowls were narrower than those estimated from elastic layer analysis with isotropic characterization. After performing a finite element method (FEM) analysis, Porter obtained similar response when granular materials were modeled as non-linear (stress-dependent) isotropic and linear anisotropic. Upon recommendations from Porter et. al. (1999) The National Association of Australian State Road Authorities (NAASRA) adopted a modular ratio (E_x/E_y) of 0.5 for unbound granular layers in their Guide to the Structural Design of Road Pavements. NAASRA also assumes that vertical and horizontal Poisson's ratios are the same.

For this study it is assumed that the five elastic parameters are stress dependent and that the moduli obey the Uzan model (Equation 19) and thus, the non-linear tangential moduli are smooth functions of the isotropic stress invariants (Equations 20, 21, and 22).

$$E_y = k_1 P_a \left(\frac{I_1}{P_a} \right)^{k_2} \left(\frac{J_2^{/}}{P_a^2} \right)^{k_3} \tag{20}$$

$$E_x = k_4 P_a \left(\frac{I_1}{P_a} \right)^{k_5} \left(\frac{J_2^{/}}{P_a^2} \right)^{k_6} \tag{21}$$

$$G_{xy} = k_7 P_a \left(\frac{I_1}{P_a} \right)^{k_8} \left(\frac{J_2^{/}}{P_a^2} \right)^{k_9} \tag{22}$$

where:

I_1 = first stress invariant (bulk stress),

$J_2^{/}$ = second stress invariant of the deviatoric stress tensor, and

k_i = material parameters.

Based on the thermodynamic requirements and Equations 16, 20, 21 and 22, vertical and horizontal Poisson's ratios can be expressed as:

$$2\frac{\partial \nu_{xy}}{\partial J_2^{/}} - \frac{k_6}{I_1 J_2^{/}}\nu_{xy} = -\frac{\Phi_1(I_1, J_2^{/})}{2I_1} \tag{23}$$

$$2\frac{\partial \nu_{xx}}{\partial J_2^{/}} - \frac{k_6}{I_1 J_2^{/}}\nu_{xx} = -\frac{\Phi_2(I_1, J_2^{/})}{2I_1} \tag{24}$$

where:

$\Phi_i(I_1 , J_2^{/})$ = functions of $I_1 , J_2^{/}$.

TESTING PROTOCOL

The repeated load triaxial test has been used extensively to study the behavior of unbound granular materials, despite its inability to simulate the rotation of principal stresses associated with shear stress reversal under a rolling wheel load. Allen (1973) conducted triaxial tests in which the chamber confining pressure was varied simultaneously with the deviator stress. While the technique did not account for the rotation of principal planes, it attempted to better simulate conditions under a moving wheel load. Stress pulse duration was 0.15 seconds for the primary test series. Results of the variable confining pressure tests yielded slightly lower values of the resilient modulus than did the constant confining pressure tests. However, the difference was not constant and did not appear to be significant. Using a Hollow Cylinder Apparatus (HCA), Chan (1990) demonstrated that resilient strains were unaffected by rotation of principal stress phenomenon. He also showed that the principal planes of strain remained coincident with those of stress. These findings support the use of an invariant approach for pavement analysis and the use of relatively simple resilient strain models derived from triaxial tests rather than a more complex apparatus such as the HCA.

There has been extensive work in the development of the repeated load triaxial test in both Europe and North America. The test has been used in the U.S. since the 1950's (Seed *et al.*, 1955). AASHTO has adopted three procedures for measuring the resilient

modulus of granular materials in the past. The recent AASHTO standard procedure (AASHTO T294-94; "Resilient Modulus of Unbound Granular Base/Subbase Materials and Subgrade Soils" - SHRP Protocol P46) provides specifications for measuring axial deformations on the specimen using externally mounted linear variable differential transducers (LVDTs). The procedure does not provide specifications for measuring the lateral/radial strains. Also, confining stresses are not cycled and only deviator stresses are cycled.

Other researchers (Nazarian 1996, Uzan 1997, and Tutumluer 1998) have recommended changes to AASHTO T-294-94. These changes include:

- measurement of radial strains,
- specimen conditioning, and
- testing sequence.

In Europe, a triaxial apparatus was developed at Nottingham University (Boyce 1976) which has a system for cycling both deviator and confining stresses. Pore water pressure is also measured during the test. Details of the development of the apparatus are outlined in Boyce (1976), Pappin (1979), Boyce et. al. (1976), and Brown et. al. (1989). It can be seen that a single testing protocol has not been universally adopted.

Faster triaxial cells have recently been designed and manufactured. Most notable of which is Industrial Process Control (IPC) of Australia's Rapid Triaxial Tester (RaTT) which has successfully been used at Texas Transportation Institute (TTI), University of Illinois (UI) and elsewhere.

The triaxial testing protocol permits the application of both confining and deviatoric stresses on a compacted cylindrical sample. These stresses can be manipulated to obtain a variety of stress combinations. The direction of the principal stresses (σ_1, σ_2, and σ_3) and strains (ε_1, ε_2, and ε_3) are forced to coincide, and this allows for easy analysis. The particular order of the principal stresses as major, intermediate, and minor stresses depends on the type of triaxial test performed.

The stress tensor, T in a triaxial test is given by:

$$T = \begin{bmatrix} \sigma_2 & 0 & 0 \\ 0 & \sigma_1 & 0 \\ 0 & 0 & \sigma_3 \end{bmatrix} \tag{25}$$

where:

σ_1, σ_2 , and σ_3 are the principal stresses.

Let directions 1, 2, and 3 be equal to y, x, z in the Cartesian coordinates system respectively, then the stress tensor can be expressed as:

$$T = \begin{bmatrix} \sigma_x & 0 & 0 \\ 0 & \sigma_y & 0 \\ 0 & 0 & \sigma_z \end{bmatrix} \tag{26}$$

In a conventional triaxial test on compacted cylindrical samples, the intermediate and minor principal stresses (σ_2, and σ_3) are the same and the stress tensor becomes:

$$T = \begin{bmatrix} \sigma_x & 0 & 0 \\ 0 & \sigma_y & 0 \\ 0 & 0 & \sigma_x \end{bmatrix} \tag{27}$$

This simplification unfortunately reduces the number of equations in Equation 7 from 4 to 3. Also, the shear stress and strain (τ_{xy}, and γ_{xy}) cannot be measured in a cylindrical triaxial set up. Thus, in a conventional cylindrical triaxial set up only 2 equations are available to solve for 4 of the 5 material properties of an anisotropic elastic material (Equation 28).

$$\begin{bmatrix} \frac{1}{E_x} & -\frac{\nu_{xy}}{E_x} & -\frac{\nu_{xx}}{E_x} \\ -\frac{\nu_{xy}}{E_x} & \frac{1}{E_y} & -\frac{\nu_{xy}}{E_x} \end{bmatrix} \begin{Bmatrix} \sigma_x \\ \sigma_y \\ \sigma_x \end{Bmatrix} = \begin{Bmatrix} \varepsilon_x \\ \\ \varepsilon_y \end{Bmatrix} \tag{28}$$

Equation 28 can be written in stress-strain incremental form as:

$$\begin{bmatrix} \frac{1}{E_x} & -\frac{\nu_{xy}}{E_x} & -\frac{\nu_{xx}}{E_x} \\ -\frac{\nu_{xy}}{E_x} & \frac{1}{E_y} & -\frac{\nu_{xy}}{E_x} \end{bmatrix} \begin{Bmatrix} \Delta\sigma_x \\ \Delta\sigma_y \\ \Delta\sigma_x \end{Bmatrix} = \begin{Bmatrix} \Delta\varepsilon_x \\ \\ \Delta\varepsilon_y \end{Bmatrix} \tag{29}$$

In order to numerically solve for the five anisotropic elastic properties, a new testing protocol was developed. A programmed loading sequence involving ten stress states, which represent typical stresses within unbound granular layers in pavements is used in the testing protocol. Three different triaxial regimes were established and implemented within each stress state in the development of the new testing protocol.

Here, it is assumed that the elastic moduli obey the Uzan (1988) model and thus, the non-linear tangential moduli are smooth functions of the isotropic stress invariants (Equations 20, 21, 22). It is also assumed that the variations of these tangential moduli are negligible within infinitesimal changes in stresses at a particular stress state. Thus at a given stress state, the material is assumed to behave linearly elastically within a small excursion of stresses. The three triaxial regimes implemented within each stress state are discussed in the following sections.

Triaxial Compression Regime

In this test regime, a sample is loaded statically to a target stress state (axial stress σ_y, and radial stress, σ_x). Then radial stress is kept constant while the axial stress is dynamically cycled in stress increments of $\Delta\sigma_y$. Equation 29 can then be expressed as:

$$\begin{bmatrix} \frac{1}{E_x} & -\frac{\nu_{xy}}{E_x} & -\frac{\nu_{xx}}{E_x} \\ -\frac{\nu_{xy}}{E_x} & \frac{1}{E_y} & -\frac{\nu_{xy}}{E_x} \end{bmatrix} \begin{Bmatrix} \Delta\sigma_x^c \\ \Delta\sigma_y^c \\ \Delta\sigma_x^c \end{Bmatrix} = \begin{Bmatrix} \Delta\varepsilon_x^c \\ \\ \Delta\varepsilon_y^c \end{Bmatrix} \tag{30}$$

where:

$\Delta\varepsilon_x^c$ is a change in radial strain due to an infinitesimal change in axial stress $)\Phi_y^c$ in triaxial compression,

$\Delta\varepsilon_y^c$ is a change in axial strain due to an infinitesimal change in axial stress $)\Phi_y^c$ in triaxial compression, and

$\Delta\sigma_x^c = 0$

Triaxial Shear Regime

After a sample is loaded to a static stress state (axial stress σ_y, and radial stress σ_x), a small dynamic axial stress increment of $\Delta\sigma_y^S$ is applied to the sample while the radial stress is reduced by a small change in dynamic stress of $\Delta\sigma_x^S$ such that:

$$\Delta\sigma_x^s = -\frac{1}{2}\Delta\sigma_y^s \tag{31}$$

and,

$$\begin{bmatrix} \frac{1}{E_x} & -\frac{\nu_{xy}}{E_x} & -\frac{\nu_{xx}}{E_x} \\ -\frac{\nu_{xy}}{E_x} & \frac{1}{E_y} & -\frac{\nu_{xy}}{E_x} \end{bmatrix} \begin{Bmatrix} \Delta\sigma_x^s \\ \Delta\sigma_y^s \\ \Delta\sigma_x^s \end{Bmatrix} = \begin{Bmatrix} \Delta\varepsilon_x^s \\ \\ \Delta\varepsilon_y^s \end{Bmatrix} \tag{32}$$

The change in first stress invariant, ΔI_1 is zero:

$$\Delta I_1 = \Delta\sigma_y^s + 2\Delta\sigma_x^s = \Delta\sigma_y^s - 2\frac{1}{2}\Delta\sigma_y^s = 0 \tag{33}$$

The change in second invariant of the deviatoric stress tensor, $\Delta J'_2$ is given by:

$$\Delta J_2^{/s} = \frac{1}{3}(\Delta\sigma_y^s - \Delta\sigma_x^s) \tag{34}$$

Substituting Equation 31 into 34,

$$\Delta J_2^{/s} = \frac{3}{4}(\Delta\sigma_y^s)^2 \tag{35}$$

The change in strain energy, ΔE^S is given by:

$$\Delta E^s = \frac{1}{2}(\Delta\sigma_x^s\,\Delta\varepsilon_x^s + \Delta\sigma_y^s\,\Delta\varepsilon_y^s + \Delta\sigma_x^s\,\Delta\varepsilon_x^s) \tag{36}$$

Substituting Equation 31 into 36 yields,

$$\Delta E^s = \frac{1}{2}\Delta\sigma_y^s(\Delta\varepsilon_y^s + \Delta\varepsilon_x^s) \tag{37}$$

But from Equation 11 and since the change in first stress invariant, ΔI_1, is zero, the change in strain energy can be written as:

$$\Delta E^s = \frac{\Delta J_2^{/}}{2G_{xy}} \tag{38}$$

Substituting Equations 35 and 37 into 38 yields,

$$G_{xy} = \frac{3}{4}\frac{\Delta\sigma_y^s}{(\Delta\varepsilon_y^s - \Delta\varepsilon_x^s)} \tag{39}$$

Thus this triaxial stress regime can be used to determine the shear modulus, G_{xy} at any stress state by Equation 39.

Triaxial Extension Regime

In this triaxial regime, the static axial stress, σ_y is reduced by a small change in dynamic stress, $\Delta\sigma_y^e$ while the radial stress, $\Delta\sigma_x$ is increased by a small dynamic stress of $\Delta\sigma_x^e$. Thus, the net change in stress state is in an extension mode but the principal stresses are not reversed. Here, Equation 29 is expressed as:

$$\begin{bmatrix} \frac{1}{E_x} & -\frac{\nu_{xy}}{E_x} & -\frac{\nu_{xx}}{E_x} \\ -\frac{\nu_{xy}}{E_x} & \frac{1}{E_y} & -\frac{\nu_{xy}}{E_x} \end{bmatrix} \begin{Bmatrix} \Delta\sigma_x^e \\ \Delta\sigma_y^e \\ \Delta\sigma_x^e \end{Bmatrix} = \begin{Bmatrix} \Delta\varepsilon_x^e \\ \\ \Delta\varepsilon_y^e \end{Bmatrix} \tag{40}$$

where:

$\Delta\varepsilon_x^e$ is a change in radial strain due to an infinitesimal change in axial stress $\Delta\sigma_y^c$ and radial stress $\Delta\sigma_x^e$, and

$\Delta\varepsilon_y^c$ is a change in axial strain due to an infinitesimal change in axial stress $\Delta\sigma_y^c$ and radial stress $\Delta\sigma_x^e$.

System Identification Method

The objective of the system identification (SID) process is to estimate the system characteristics using only input and output data from the system to be identified (Wang and Lytton, 1993). The simplest method for representing the behavior of a physical process is to model it with a mathematical representation, for example Equation 29. The model is said to be ‘‘identified’’ when the error between the model and the real process is minimized to some acceptable level. Otherwise the model must be modified until the desired level of agreement is achieved.

Figure 2 is a schematic diagram of the SID procedure. The model response, y_k, is compared to the actual response of the system, y, and the error, e, between the two is used to adjust the parameters of the model by means of an algorithm which optimizes some prescribed criterion.

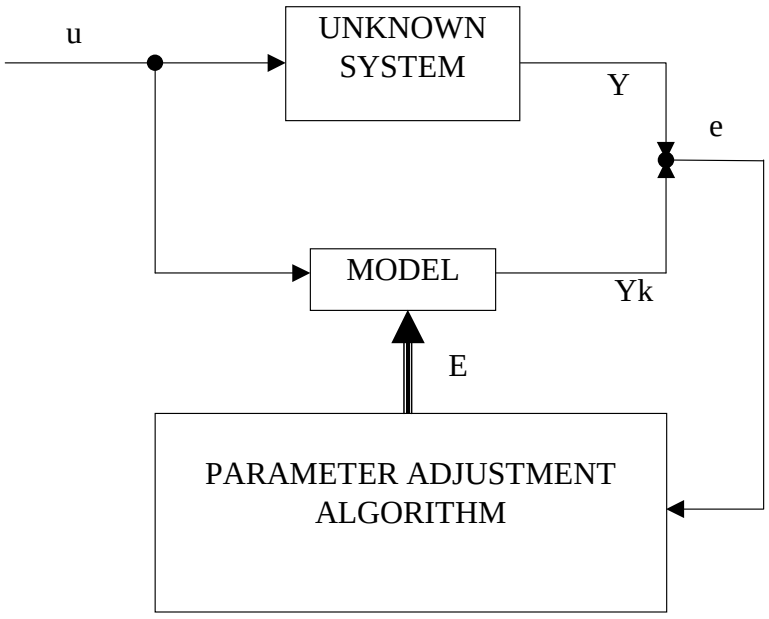

Figure 2. System Identification Scheme.

The SID method requires accurately measured output data of the unknown system, a suitable model to represent the behavior of the system, and an efficient parameter adjustment algorithm that converges accurately and rapidly.

An algorithm can be developed for adjusting model parameters on the basis of Taylor's series expansion. Let the mathematical model of some process be defined by n parameters:

$$f = f(p_1, p_2, \cdots, p_n; x, t) \tag{41}$$

where x and t are independent spatial and temporary variables.

Then any function $f_k(p_1, p_2, \ldots, p_n; x_k, t_k)$ may be expanded in a Taylor's series as:

$$f_k(p + \Delta p) = f_k(p) + \nabla f_k \cdot \Delta p + 0^2 \tag{42}$$

where the parameters have all been collected into a vector

$$p = [p_1, p_2, \ldots, p_n]^T$$

If we assume $f_k(p+\Delta p)$ to be the actual output of the system and $f_k(p)$ the output of the model for the most recent set of parameters, the error between the two outputs becomes:

$$\left.\begin{aligned} e_k &= f_k(p + \Delta p) - f_k(p) \\ &= \nabla f_k \cdot \Delta p \\ &= \frac{\partial f_k}{\partial p_1}\Delta p_1 + \frac{\partial f_k}{\partial p_2}\Delta p_2 + \cdots + \frac{\partial f_k}{\partial p_n}\Delta p_n \end{aligned}\right\} \tag{43}$$

It should be noted that e_k represents the difference between the actual system output and the model output for each observed point k. If the error is evaluated at m values ($m \geq n$) of the independent variables, m equations will be generated as:

$$\left.\begin{aligned} e_1 &= \frac{\partial f_1}{\partial p_1}\Delta p_1 + \frac{\partial f_1}{\partial p_2}\Delta p_2 + \cdots + \frac{\partial f_1}{\partial p_n}\Delta p_n \\ e_2 &= \frac{\partial f_2}{\partial p_1}\Delta p_1 + \frac{\partial f_2}{\partial p_2}\Delta p_2 + \cdots + \frac{\partial f_2}{\partial p_n}\Delta p_n \\ &\vdots \\ e_m &= \frac{\partial f_m}{\partial p_1}\Delta p_1 + \frac{\partial f_m}{\partial p_2}\Delta p_2 + \cdots + \frac{\partial f_m}{\partial p_n}\Delta p_n \end{aligned}\right\} \tag{44}$$

Equation 44 can be conveniently non-dimensionalized by dividing both sides by f_k to give:

$$\frac{e_k}{f_k} = \sum_{\substack{i=1 \\ k=1}}^{\substack{i=n \\ k=m}} \frac{\partial f_k}{\partial p_i} \frac{p_i}{f_k} \frac{\Delta p_i}{p_i} \tag{45}$$

Matrix values *r*, *F*, and α are defined as:

$$r = [r_1\, r_2 \ldots r_m]^T$$

$$r_k = \frac{e_k}{f_k}$$

$$F = [F_{ki}]$$

$$F_{ki} = \frac{\partial f_k}{\partial p_i} \cdot \frac{p_i}{f_k}$$

$$\alpha = [\alpha_1\, \alpha_2 \ldots \alpha_n]^T$$

$$\alpha_i = \frac{\Delta p}{p_i}$$

Then, Equation 45 can be written as:

$$r = F\alpha \tag{46}$$

The vector r is completely determined from the outputs of the model and the real system. The matrix *F* is usually called the sensitivity matrix, because its elements F_{ki} reflect the sensitivity of the output f_k to the parameter p_i. It is generated by the differentials of the output f_k with respect to the parameter p_i.

The unknown vector α reflects the relative changes of the parameters. It can be obtained by using a generalized inverse procedure to solve equation 46. However, there might be column degeneracy in the sensitivity matrix *F*. This condition may be encountered when two or more parameters have similar effects, or any parameter has a negligible effect on the behavior of the model. In these cases Equation 46 may be ill conditioned and more powerful numerical techniques such as the singular value decomposition (SVD) and Han's method (Han, 1976) must be used to give meaningful solutions.

Once the vector α is obtained, a new set of parameters is determined as:

$$p_i^{r+1} = p_i^r (1 + \alpha) \tag{47}$$

where r is the iteration number.

The iteration process is continued until the desired convergence is reached. In order to avoid convergence problems, the new set of parameters are not changed by more than 60% of the adjustment vector α. The value 0.6 acts as a relaxation factor for smooth convergence.

Applying the procedure described above to the triaxial model expressed in Equation 29, there are 4 parameters (E_y , E_x , ν_{xy} , ν_{xx}) and 2 outputs ($\Delta\varepsilon_x$, $\Delta\varepsilon_y$). The actual system outputs are the measured axial and radial strains. The model strains (model output) can be determined from the values of the parameters, which can be guessed initially from the system output. The difference between the measured strains and the model strains (model output) represents the error which can be improved through the parameter adjustment routine until a desired criterion is achieved.

The matrices in Equation 46 may be defined as:

$$F = \begin{bmatrix} \dfrac{\partial(\Delta\varepsilon_x)}{\partial E_x}\cdot\dfrac{E_x}{\Delta\varepsilon_x^{\wedge}} & \dfrac{\partial(\Delta\varepsilon_x)}{\partial \nu_{xy}}\cdot\dfrac{\nu_{xy}}{\Delta\varepsilon_x^{\wedge}} & \dfrac{\partial(\Delta\varepsilon_x)}{\partial \nu_{xx}}\cdot\dfrac{\nu_{xx}}{\Delta\varepsilon_x^{\wedge}} & \dfrac{\partial(\Delta\varepsilon_x)}{\partial E_y}\cdot\dfrac{E_y}{\Delta\varepsilon_x^{\wedge}} \\ \dfrac{\partial(\Delta\varepsilon_y)}{\partial E_x}\cdot\dfrac{E_x}{\Delta\varepsilon_y^{\wedge}} & \dfrac{\partial(\Delta\varepsilon_y)}{\partial \nu_{xy}}\cdot\dfrac{\nu_{xy}}{\Delta\varepsilon_y^{\wedge}} & \dfrac{\partial(\Delta\varepsilon_y)}{\partial \nu_{xx}}\cdot\dfrac{\nu_{xx}}{\Delta\varepsilon_y^{\wedge}} & \dfrac{\partial(\Delta\varepsilon_y)}{\partial E_y}\cdot\dfrac{E_y}{\Delta\varepsilon_y^{\wedge}} \end{bmatrix} \tag{48}$$

$$\alpha = \begin{bmatrix} \dfrac{E_x^{r+1}}{E_x^{r}} & \dfrac{\nu_{xy}^{r+1}}{\nu_{xy}^{r}} & \dfrac{\nu_{xx}^{r+1}}{\nu_{xx}^{r}} & \dfrac{E_y^{r+1}}{E_y^{r}} \end{bmatrix}^T \tag{49}$$

$$r = \begin{Bmatrix} \dfrac{\Delta\varepsilon_x^m - \Delta\varepsilon_x^{\wedge}}{\Delta\varepsilon_x^{\wedge}} \\ \dfrac{\Delta\varepsilon_y^m - \Delta\varepsilon_y^{\wedge}}{\Delta\varepsilon_y^{\wedge}} \end{Bmatrix} \tag{50}$$

where:

$$\frac{\partial\Delta\varepsilon_x}{\partial E_x} = -\frac{1}{E_x^2}\left[(1-\nu_{xx})\Delta\sigma_x - \nu_{xy}\Delta\sigma_y\right],$$

$$\frac{\partial\Delta\varepsilon_x}{\partial \nu_{xy}} = -\frac{1}{E_x}\Delta\sigma_y,$$

$$\frac{\partial \Delta\varepsilon_x}{\partial \nu_{xx}} = -\frac{1}{E_x}\Delta\sigma_x,$$

$$\frac{\partial \Delta\varepsilon_x}{\partial E_y} = 0,$$

$$\frac{\partial \Delta\varepsilon_y}{\partial E_x} = \frac{2\nu_{xy}}{E_x^2}\Delta\sigma_x,$$

$$\frac{\partial \Delta\varepsilon_y}{\partial E_x} = -\frac{2}{E_x}\Delta\sigma_x,$$

$$\frac{\partial \Delta\varepsilon_y}{\partial \nu_{xx}} = 0,$$

$$\frac{\partial \Delta\varepsilon_y}{\partial E_y} = -\frac{1}{E_y^2}\Delta\sigma_y,$$

$\Delta\varepsilon_x^m$ = measured (actual system) radial strain,

$\Delta\varepsilon_y^m$ = measured (actual system) axial strain,

$\Delta\varepsilon_x^{\wedge}$ = calculated (model) radial strain, and

$\Delta\varepsilon_y^{\wedge}$ = calculated (model) axial strain.

In order to generate enough elements in the sensitivity matrix (F) and to control the number of row degeneracy, the three stress regimes (triaxial-compression, -shear, and -extension) were combined to give one F-matrix and one r-matrix at each stress state. Thus, at each stress state, Equation 46 can be rewritten as:

$$\begin{bmatrix} F^{TC} \\ F^{TS} \\ F^{TE} \end{bmatrix} \{\alpha\} = \begin{Bmatrix} r^{TC} \\ r^{TS} \\ r^{TE} \end{Bmatrix} \qquad (51)$$

$6\,X\,4 \quad 4X1 \quad 6X1$

where:

F^{TC} = the sensitivity matrix for triaxial compression regime,

F^{TS} = the sensitivity matrix for triaxial shear regime,

F^{TE} = the sensitivity matrix for triaxial extension regime,

r^{TC} = the r-vector for triaxial compression regime,

r^{TS} = the r-vector for triaxial shear regime, and

r^{TE} = the r-vector for triaxial extension regime.

At a particular stress state, Equation 51 is needed for the parameter adjustment algorithm to determine vertical and horizontal moduli, as well as the vertical and horizontal Poisson's ratios. The shear modulus can be determined from Equation 39.

Preparation of Specimen

The specimens were prepared with a gyratory compactor. Figure 3 shows a picture of the gyratory compactor. The development and validation of the gyratory compactor for use in molding unbound granular materials can be found elsewhere (Milberger and Dunlop, 1966; Moore and Milberger, 1968). Gyratory shear is the means of compaction. The method is widely used in Texas to compact unbound granular materials and bituminous-stabilized bases. One of the major contributions of the Strategic Highway Research Program (SHRP) was the adoption of the gyratory compaction method for molding asphalt concrete mixtures.

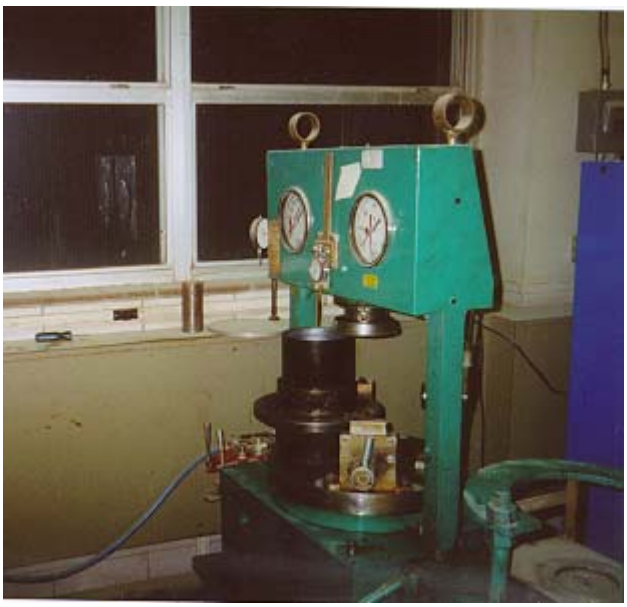

Figure 3. Texas Gyratory Compactor.

The particle distribution and orientation in samples compacted with the gyratory compaction method closely matches field compaction. The method is not widely used for molding unbound granular materials but the Texas Department of Transportation

(TxDOT) has a standard procedure (Test Method Tex-126-E) for compacting unbound and bituminous base materials. Molding of specimen with this method basically involves the application of a known stress to a sample in a rigid mold after the mold has been inclined at an angle, typically 3°. The mold is then gyrated with the applied stress still on the sample until the desired density is achieved.

In this study, 6-in (150-mm) diameter and 6-in (150-mm) height samples were molded for testing. Some samples were also prepared with the vibratory and impact compaction methods. The purpose of using these other compaction methods will be discussed later.

Triaxial Equipment

Triaxial testing data have been traditionally used to provide input for the material properties in pavement structural models. The triaxial test has been used with notable success in the field of geotechnical engineering for applications such as earthquake and tunnel modeling as well as pavements.

Tests are performed on materials to establish their engineering properties and these properties are then used in a structural model to determine the stresses and strains that lead to performance predictions. By setting boundary conditions in the structural model, it is not necessary for a material property test to exactly mimic the field condition. However, the testing should, if practical, span a range of expected conditions so that extrapolations used by the structural model are kept to a minimum.

In the past, the traditional fluid-filled geotechnical type triaxial cell, that enables confining pressure to be applied to a specimen while a range of vertical loads are applied, has been the major apparatus used in this type of testing. However, the amount of time and attention to detail necessary to set up and carry out tests with this equipment make it unsuitable for production use in the field, for Quality-Control/Quality-Assurance purposes (QC/QA). One other problem associated with the traditional triaxial cell is that the membrane around the sample is secured to top and bottom platens with rubber bands. This assembly system induces high shear stresses at the top and bottom of samples tested. To eliminate this problem, it is highly encouraged that sample sizes be maintained at a 2.0 height to diameter ratio.

In this study, the Rapid Triaxial Testing (RaTT) cell system developed by Industrial Process Controls (IPC) Melbourne, Australia, was used for testing. The RaTT cell system is based on a concept that was conceived in Texas Transportation Institute (TTI) and has been in use with the Texas Department of Transportation (TxDOT). Unlike the traditional triaxial cell, the RaTT cell uses a larger diameter confining cylinder around the specimen, which is fitted with an internal rubber membrane that can be inflated to apply confining pressure to the specimen. The rubber membrane is not rigidly fastened to the top and bottom platens and thus there is a relatively uniform distribution of stresses within the height of samples during testing.

The IPC system provides automated control of cell movement to simplify specimen handling, and computer control of both confining and axial stress, together with Linear Variable Differential Transducers (LVDTs) for vertical and horizontal strains. Figures 4 and 5 are pictures with the cell lowered and raised, respectively of the RaTT cell.

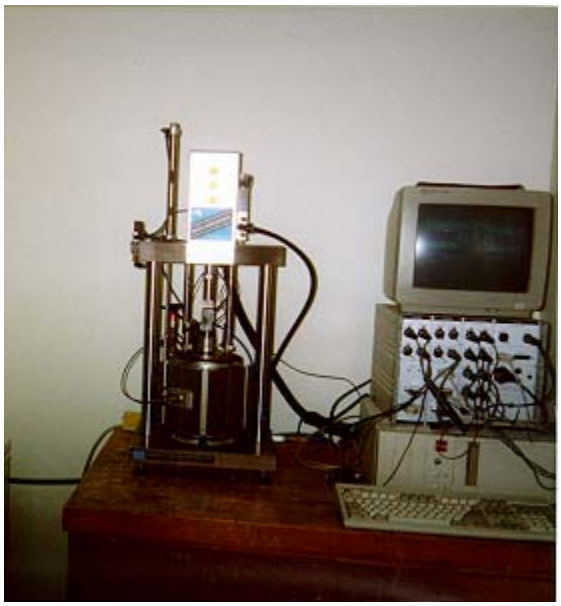

Figure 4. Lowered RaTT Cell.

Figure 5. Raised RaTT Cell.

Automated control of the physical movement of the cell turns the extremely tedious job of getting a specimen in and out of a standard geotechnical cell and positioning all the instrumentation in the standard cell into a quick and easy operation taking less than a minute. Servo-control of the cell pressure enables a vacuum to be applied to the cell, which draws the pressure membrane and the horizontal LVDT away from the sides of the specimen. Once the vacuum has been applied, a pneumatic actuator lifts the entire cell up out of the way so that the previously tested specimen may be removed and the next specimen may be placed in position. The cell may then be lowered over a new specimen on the command of the operator using a single keystroke command to the software.

The apparatus can perform tests at multiple frequencies as well as multiple stress states. This capability enables the machine to quantify not only time-dependent response, but also stress-dependent response of the material, two features that are required for flexible pavement materials characterization.

The IPC RaTT cell is supported by software, which provides researchers and engineers with a tool capable of conducting a range of uniaxial or multiaxial loading tests on both bound and unbound construction materials. The software can be specifically

customized to provide the operator with a unique testing sequence and output. Other researchers to fit their specific needs and purposes have customized the RaTT cell. Examples are the University of Illinois Fast Cell (UIFC) and the TUDelft (The Netherlands) cell.

Triaxial Testing

The stresses used in the triaxial testing were chosen to represent the stress conditions induced in a typical base layer of a flexible pavement by traffic loads. The testing protocol itself involves a programmed loading sequence employing ten static stress states, which represent typical stresses in a pavement. At each static stress state, small dynamic changes in stresses are applied to obtain three triaxial stress regimes such that the net stress changes represent triaxial compression, triaxial shear, and triaxial extension. The resilient axial and radial strains are determined for each stress regime and implemented in the system identification scheme to back-calculate the five anisotropic elastic properties for that particular stress state.

Before each test is started, the specimen is mounted in the RaTT cell as described in the operator's test procedure manuals (IPC, 1998). The loading sequence is outlined in the following steps:

- A mounted sample is loaded to a static stress state (axial stress σ_y, and confining stress σ_x). The confining stress is then kept constant while the axial stress is given a small dynamic stress increment of $\Delta\sigma_y$. The incremental loading is applied for 25 repetitions until a stable resilient strain is achieved. A cycle of loading consists of 1.5 seconds loading followed by 1.5 seconds rest period.
- At the same static stress state (σ_x, σ_y) as in the triaxial compression regime, the axial stress is changed by a small dynamic stress increment of $\Delta\sigma_y$ for 25 repetitions as before, while the radial stress is reduced by $\Delta\sigma_x$ such that the change in the first stress invariant (ΔI_1) is zero in each load cycle.
- At the same controlled static stress state (σ_x, σ_y) as before the axial stress is reduced by a small amount, $\Delta\sigma_y$, while the radial stress is increased by $\Delta\sigma_x$. Thus, the net change in stress state is in an extension mode but the principal stresses are

not reversed. The dynamic stresses are applied for 25 repetitions as before until stable resilient strains are achieved.

- These steps are repeated for the ten different stress states. At each stress state, the resilient axial and radial strains are measured for use as input into the SID scheme.

Table 2 shows the static and dynamic stresses applied at the ten different stress states. At the frequencies tested (1.5 seconds loading and 1.5 seconds rest), it takes about one and a half hours to complete testing at all the ten stress states.

Table 2. Static and Dynamic Stresses.

Stress State	Static Stress (kPa)		Dynamic Stress (kPa)					
			Triaxial Compression		Triaxial Shear		Triaxial Extension	
	σ_y	σ_x	$\Delta\sigma_y$	$\Delta\sigma_x$	$\Delta\sigma_y$	$\Delta\sigma_x$	$\Delta\sigma_y$	$\Delta\sigma_x$
1	40	25	5	0	10	-5	-5	5
2	50	25	10	0	10	-5	-10	5
3	70	40	10	0	10	-5	-10	10
4	130	60	20	0	20	-10	-10	10
5	150	70	20	0	20	-10	-10	10
6	170	100	20	0	20	-10	-20	20
7	220	120	30	0	30	-15	-20	20
8	250	140	30	0	30	-15	-20	20
9	250	120	30	0	30	-15	-20	20
10	250	105	30	0	30	-15	-20	20

The measured axial and radial strains at each stress state are used as input to the parameter adjustment routine, Equation 51, of the system identification scheme. A computer program has been developed that systematically back-calculates the five cross-anisotropic elastic material properties based on the SID method.

MATERIALS TESTED

Four base material types, California granite, Texas crushed limestone, Texas gravel and Minnesota gravel were tested in the laboratory to determine their cross-anisotropic elastic properties.

These materials were selected based on material variability, usage, and on-going research. The California granite and the Texas limestone are rough textured, angular crushed rock, the Texas gravel is rounded pit gravel, and the Minnesota gravel is rounded glacial sandy gravel.

The samples were tested in the IPC Rapid Triaxial Tester. 150-mm diameters by 150-mm height samples were compacted using the Texas Gyratory Compactor. A comprehensive laboratory study was performed to determine the cross-anisotropic elastic properties of the four materials. Three different gradations, well-graded, fine-graded and coarse-graded, were prepared for all aggregate types; and the samples were tested at optimum, wet of optimum, and dry of optimum. Table 3 and Figure 6 show the three gradations batched. Three sample replicates were prepared at each moisture and gradation condition. Table 4 is a laboratory test matrix that was generally followed to complete the testing phase of this study.

Some samples were compacted with the impact compaction method following AASHTO Designation T-180 and tested with the RaTT. A few other samples were compacted with the vibratory compaction method at the University of Illinois and tested with the UIFC.

The purpose of using other compaction methods and triaxial facilities was to validate and access the impact of material, compaction, and testing equipment variability on the model. For each of the three compaction methods, two compaction efforts (high and low) were investigated.

Table 3. Gradation.

Sieve Size (mm)	Percent Passing (%)		
	Fine Graded	Well Graded	Coarse Graded
25.00	100	100	100
19.00	85	85	85
12.50	74	74	72
9.50	70	66	62
4.75	67	54	40
2.36	62	41	25
1.18	52	30	18
0.60	42	23	14
0.30	34	18	10
0.15	28	14	8
0.075	20	10	7

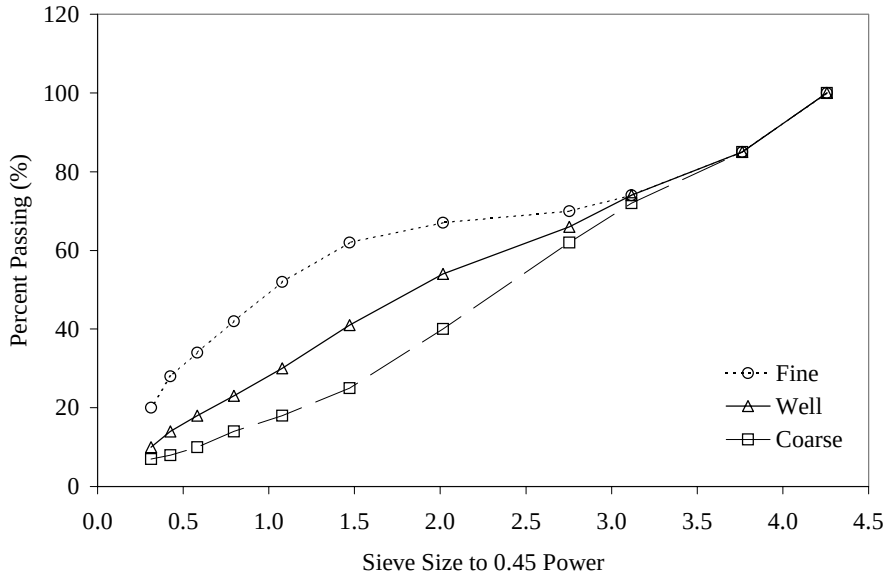

Figure 6. Gradation on a 0.45 Power Sheet.

Table 4. Test Matrix.

Moisture Conditions	Aggregate Source								
	Granite			Limestone			Gravel		
	Gradation								
	Coarse	Well	Fine	Coarse	Well	Fine	Coarse	Well	Fine
Wet	√	√	√	√	√	√	√	√	√
Opt	√	√	√	√	√	√	√	√	√
Dry	√	√	√	√	√	√	√	√	√

ANALYSIS OF DATA

General

The Liquid limits and plasticity indices of the material tested are tabulated in Table 5. The original materials were separated by size down to the #200 sieve, and the individual particle sizes were recombined to obtain well-graded, fine-graded, and coarse-graded samples as discussed in the previous section. It was difficult to compact coarse graded samples of materials with low plasticity indexes (California granite and Minnesota gravel), so coarse graded samples were not molded for these materials.

Table 5. Atterberg's Limits.

Specimen	Liquid Limit (%)	Plasticity Index (%)
Texas Gravel	20.2	11.8
Texas Limestone	14.9	4.4
Minnesota Gravel	18.4	2.0
California Granite	11.6	NP

A three-parameter equation (Fredlund and Xing, 1994) was used to fit the three gradations. This equation allows for a continuos fit and proper definition of the extremes of the gradation curve and is given by:

$$P_p = \frac{100}{\ln\left[\exp(1) + \left(\frac{g_a}{d}\right)^{g_n}\right]^{g_m}} \left[1 - \left[\frac{\ln\left(1 + \frac{d_r}{d}\right)}{\ln\left(1 + \frac{d_r}{d_m}\right)}\right]^7\right] \qquad (52)$$

where:

P_p = percent passing a particular grain-size, d,

g_a = fitting parameter corresponding to the initial break in the grain-size curve,

g_n = fitting parameter corresponding to the maximum slope of the grain-size curve,

g_m = fitting parameter corresponding to the curvature of the grain-size curve,

d = particle diameter (mm),

d_r = residual particle diameter (mm), and

d_m = minimum particle diameter (mm).

Non-linear regression analysis was used to obtain the three parameters of Equation 52 that fit the three gradations considered. The values of the parameters are tabulated in Table 6.

Table 6. Gradation Parameters.

Parameter	Coarse Graded	Well Graded	Fine Graded
g_a	13.272	11.997	4.726
g_n	0.988	0.976	1.361
g_m	2.414	1.544	0.685

At each gradation, three moisture levels were used in molding the samples. The samples were compacted dry of optimum, at optimum and wet of optimum. Three replicate samples were compacted at each moisture and gradation combination. Thus, in the original test matrix, a total of 108 samples (4 materials by 3 gradations by 3 moisture levels by 3 replicates) were to be prepared. As mentioned earlier a few samples were abandoned because they were both difficult to compact at the levels of moisture and gradation or were too soft to test.

The samples were compacted with the Texas Gyratory Compactor (TGC). A few of the samples were compacted with the impact hammer and the vibratory compactor. The purpose of using the impact and vibratory compaction methods was to investigate the effect of compaction method and level on the mechanical properties of the materials. The details of the compaction investigation will be discussed later. The average values of dry densities and molding moisture contents are tabulated in Tables 7 through Table 10.

150-mm diameter by 150-mm height sample were compacted and tested in the IPC Rapid Triaxial Tester. Each sample was tested at ten static stress states as described in the previous section. At each stress state, small stress excursions were applied to the sample so that the net changes in stresses are a triaxial compression, triaxial shear and triaxial extension. The static stresses applied are typical stresses induced in an unbound granular base layer due to traffic loads. These static stresses are well below the failure

envelope of unbound granular materials. Figures 7 and 8 are plots of static stresses and small stress excursions applied to each sample at the ten stress-states in a σ_1-σ_3 and $\sqrt{J_2'}$-I_1 stress space, respectively.

Table 7. Moisture Content and Dry Densities for Texas Limestone.

	Coarse		Well			Fine	
	Optimum	Dry	Optimum	Wet	Dry	Optimum	Wet
Moisture Content (%)	2.8	3.5	4.1	4.9	4.7	5.4	5.9
Dry Density (kg/m^3)	2144	2260	2350	2315	2251	2302	2334

Table 8. Moisture Content and Dry Densities for Texas Gravel.

	Coarse		Well		Fine	
	Optimum	Dry	Optimum	Wet	Dry	Optimum
Moisture Content (%)	5.5	5.5	7.7	9.3	5.4	7.5
Dry Density (kg/m^3)	2020	2062	2240	2079	2075	2210

Table 9. Moisture Content and Dry Densities for Minnesota Gravel.

	Well			Fine	
	Dry	Optimum	Wet	Dry	Optimum
Moisture Content (%)	4.5	6.2	7.7	4.7	7.6
Dry Density (kg/m^3)	2139	2167	2240	2159	2296

Table 10. Moisture Content and Dry Densities for California Granite.

	Well			Fine		
	Dry	Optimum	Wet	Dry	Optimum	Wet
Moisture Content (%)	3.5	4.0	4.6	4.1	4.6	5.9
Dry Density (kg/m^3)	2179	2218	2192	2177	2215	2278

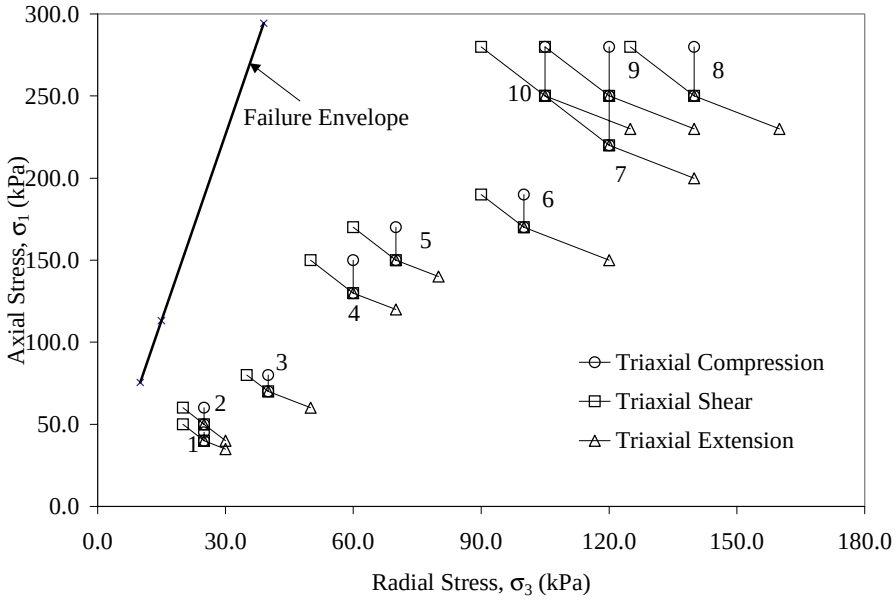

Figure 7. Applied Stresses in a σ_1-σ_3 Stress Space.

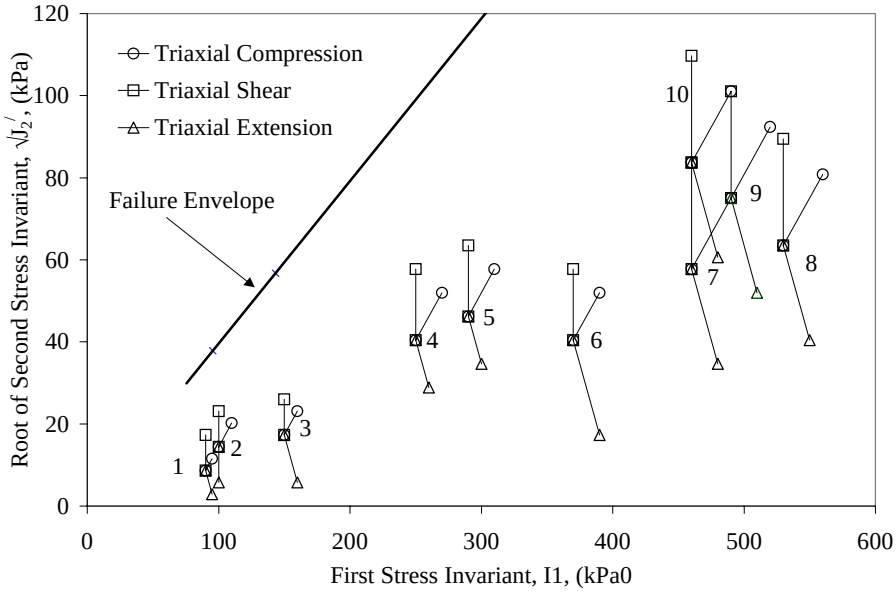

Figure 8. Applied Stesses in a $\sqrt{J_2'}$-I_1 Stress Space.

The resilient axial and radial strains due to small stress excursions were measured at each stress state and used as input into the system idenfication scheme to compute the resilient moduli and Poisson's ratios. The values of static stresses and average resilient

strains (axial and radial) due to small excursions are tabulated in Table 11 for a well graded Texas limestone compacted at optimum moisture. Similar results were obtained for the other combination of gradations and moisture levels in the test matrix and are tabulated in Appendix A.

Table 11. Average Resilient Strains for Texas Limestone at Optimum Moisture.

Stress State		Triaxial Compression		Triaxial Shear		Triaxial Extension	
Stress (kPa)		Strain (με)		Strain (με)		Strain (με)	
Axial	Radial	Axial	Radial	Axial	Radial	Axial	Radial
40.0	25.0	28.6	-12.4	98.0	-78.1	-72.4	51.1
50.0	25.0	51.0	-24.6	78.7	-72.3	-100.3	74.9
70.0	40.0	38.7	-16.7	54.1	-41.5	-97.1	75.4
130.0	60.0	50.5	-22.2	74.4	-67.0	-49.2	46.3
150.0	70.0	44.2	-19.2	64.5	-55.3	-42.7	39.3
170.0	100.0	41.6	-16.2	57.1	-39.3	-89.3	68.1
220.0	120.0	53.7	-19.0	73.4	-53.3	-67.9	53.0
250.0	140.0	47.7	-15.9	64.0	-43.1	-57.6	42.1
250.0	120.0	49.0	-17.4	66.6	-52.9	-60.2	51.5
250.0	105.0	48.3	-19.7	68.8	-63.1	-54.6	49.0

The measured axial and radial resilient strains are the actual system outputs of the system identification method. The measured resilient strains act as a nerve center of the parameter adjustment algorithm of the SID scheme. Therefore, the technique used to measure the axial and radial resilient strains is very important for accurate determination of the five anisotropic resilient properties at a particular stress state. In this study, the resilient strains were measured with externally mounted Linear Variable Differential Transducers (LVDTs). The LVDTs used are very sensitive to changes in deflection and were suitable for this study. Two LVDTs each were used and averaged for measuring axial and radial resilient strains, respectively.

A computer program was developed to determine the cross-anisotropic resilient properties of each sample in the test matrix at the ten stress states using the system

identification method. Figure 9 is a schematic program structure for the system identification method. The input parameters include the static and dynamic stresses and the axial and radial resilient strains. Initial values of the five cross-anisotropic resilient properties are then computed from the dynamic stresses and measured strains. The computed initial properties are then used to calculate the model output (calculated strains) from Equations 30, 32 and 40.

The sensitivity matrices *F* and the *r*-vectors can then be obtained from Equations 48 and 50, respectively, for the three triaxial regimes. The three *F* matrices and three *r*-vectors are then combined to obtain one *F* matrix and one *r*-vector (Equation 51). The α-vector is then determined from Equation 46 and used to compute a new set of model properties. If the initial values of the five cross-anisotropic properties are precise they will be equivalent to the new set of model properties and the measured strains, and calculated strains will also be equivalent to each other. When this occurs, the system is termed 'identified'. The criterion for identification is based on the components of the α-vector. In this study, the criterion is 1%, and this means that the system and model properties are equivalent whenever the difference between the measured and calculated strains is less than 1% of the calculated strain. If the 1% criterion is not satisfied, a new set of model output is calculated and the iteration process is continued until the desired criterion is reached.

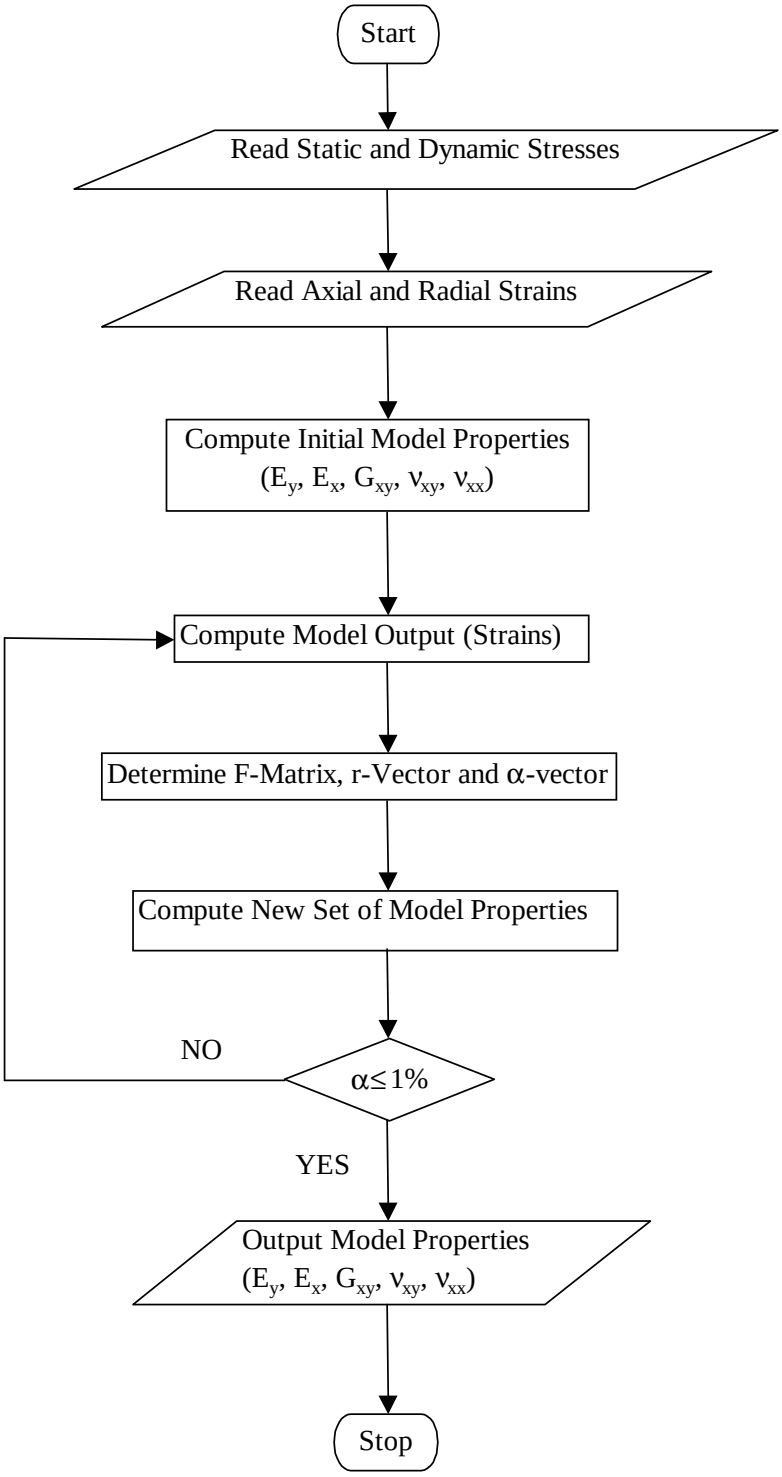

Figure 9. Program Structure for the System Identification Method.

As an example, consider the strains obtained at the first stress state for a well-graded Texas crushed limestone at optimum moisture content (Table 10).

Step 1 Input Data

Static Axial Stress, σ_y = 40.0 kPa

Static Radial Stress, σ_x = 25.0 kPa

Dynamic Change in Axial Stress for Triaxial Compression, $\Delta\sigma_y^c$, = 5 kPa

Dynamic Change in Radial Stress for Triaxial Compression, $\Delta\sigma_x^c$, = 0 kPa

Dynamic Change in Axial Stress for Triaxial Shear, $\Delta\sigma_y^s$, = 10 kPa

Dynamic Change in Radial Stress for Triaxial Shear, $\Delta\sigma_x^s$, = -5 kPa

Dynamic Change in Axial Stress for Triaxial Extension, $\Delta\sigma_y^e$, = -5 kPa

Dynamic Change in Radial Stress for Triaxial Extension, $\Delta\sigma_x^e$, = 5 kPa

Axial Resilient Strain for Triaxial Compression, $\Delta\varepsilon_y^c$ = 28.6E-06

Radial Resilient Strain for Triaxial Compression, $\Delta\varepsilon_x^c$ = -12.4E-06

Axial Resilient Strain for Triaxial Shear, $\Delta\varepsilon_y^s$ = 98.0E-06

Radial Resilient Strain for Triaxial Shear, $\Delta\varepsilon_x^s$ = -78.1E-06

Axial Resilient Strain for Triaxial Extension, $\Delta\varepsilon_y^e$ = -72.4E-06

Radial Resilient Strain for Triaxial Extension, $\Delta\varepsilon_x^e$ = 51.1E-06

Step 2 Initial Model Parameters:

$$E_y = \frac{\Delta\sigma_y^c}{\Delta\varepsilon_y^c} = \frac{5.0}{28.6E-06} = 174825.17\,kPa$$

$$E_x = \frac{\Delta\sigma_x^s}{\Delta\varepsilon_x^s} = \frac{-5.0}{-78.1E-06} = 64020.49\,kPa$$

$$G_{xy} = \frac{3}{4}\frac{\Delta\sigma_y^s}{(\Delta\varepsilon_y^s - \Delta\varepsilon_x^s)} = \frac{3}{4}\frac{10}{(98.0+78.1)E-06} = 42589.44\,kPa$$

$$\nu_{xy} = \left(\frac{\Delta\sigma_y^s}{E_y} - \Delta\varepsilon_y^s\right)\left(\frac{E_x}{2\Delta\sigma_x^s}\right) = \left(\frac{64020.49}{174825.17} - 98.0E-06\right)\left(\frac{64020.49}{2(-5)}\right) = 0.261$$

$$\nu_{xx} = 1 - \left(\left(\Delta\varepsilon_x^s + \frac{\nu_{xy}\Delta\sigma_y^s}{E_x} \right) \left(\frac{E_x}{\Delta\sigma_x^s} \right) \right)$$

$$= 1 - \left(\left(-78.1E-06 + \frac{(0.261)(10)}{64020.49} \right) \left(\frac{64020.49}{-5} \right) \right) = 0.522$$

Step 3 Model Output (Calculated Strains):

Calculated Axial Resilient Strain for Triaxial Compression, $\Delta\varepsilon_y^{c\wedge}$

$$\Delta\varepsilon_y^{c\wedge} = -\frac{2\nu_{xy}\Delta\sigma_x^c}{E_x} + \frac{\Delta\sigma_y^c}{E_y} = -\frac{(2)(0.261)(0)}{64020.49} + \frac{5}{174825.17} = 28.60E-06$$

Calculated Radial Resilient Strain for Triaxial Compression, $\Delta\varepsilon_x^{c\wedge}$

$$\Delta\varepsilon_x^{c\wedge} = \frac{\Delta\sigma_x^c(1-\nu_{xx})}{E_x} - \frac{\nu_{xy}\Delta\sigma_y^c}{E_x} = \frac{(0)(1-0.522)}{64020.49} - \frac{(0.261)(5)}{64020.49} = -20.4E-06$$

Calculated Axial Resilient Strain for Triaxial Shear, $\Delta\varepsilon_y^{s\wedge}$

$$\Delta\varepsilon_y^{s\wedge} = -\frac{2\nu_{xy}\Delta\sigma_x^s}{E_x} + \frac{\Delta\sigma_y^s}{E_y} = -\frac{(2)(0.261)(-5)}{64020.49} + \frac{10}{174825.17} = 98.0E-06$$

Calculated Radial Resilient Strain for Triaxial Shear, $\Delta\varepsilon_x^{s\wedge}$

$$\Delta\varepsilon_x^{s\wedge} = \frac{\Delta\sigma_x^s(1-\nu_{xx})}{E_x} - \frac{\nu_{xy}\Delta\sigma_y^s}{E_x} = \frac{(-5)(1-0.522)}{64020.49} - \frac{(0.261)(10)}{64020.49} = -78.1E-06$$

Calculated Axial Resilient Strain for Triaxial Extension, $\Delta\varepsilon_y^{e\wedge}$

$$\Delta\varepsilon_y^{e\wedge} = -\frac{2\nu_{xy}\Delta\sigma_x^e}{E_x} + \frac{\Delta\sigma_y^e}{E_y} = -\frac{(2)(0.261)(5)}{64020.49} + \frac{-5}{174825.17} = 69.40E-06$$

Calculated Radial Resilient Strain for Triaxial Extension, $\Delta\varepsilon_x^{e\wedge}$

$$\Delta\varepsilon_x^{e\wedge} = \frac{\Delta\sigma_x^e(1-\nu_{xx})}{E_x} - \frac{\nu_{xy}\Delta\sigma_y^e}{E_x} = \frac{(5)(1-0.522)}{64020.49} - \frac{(0.261)(-5)}{64020.49} = 57.7E-06$$

Step 4 Determine *F*-matrix, Equations 48 and 51:

$$F = \begin{bmatrix} F^{TC} \\ F^{TS} \\ F^{TE} \end{bmatrix} = \begin{bmatrix} -1.00 & 1.00 & 0.00 & 0.00 \\ 0.00 & 0.00 & 0.00 & -1.00 \\ -1.00 & 0.52 & -0.52 & 0.00 \\ -0.42 & 0.42 & 0.00 & -0.58 \\ -1.00 & 0.35 & -0.71 & 0.00 \\ -0.59 & 0.59 & 0.00 & -0.41 \end{bmatrix}$$

Step 5 Determine *r*-vector, Equations 50 and 51:

$$r = \begin{Bmatrix} r^{TC} \\ r^{TS} \\ r^{TE} \end{Bmatrix} = \begin{Bmatrix} -0.39 \\ -6.36E-08 \\ 0.00 \\ 0.00 \\ -0.11 \\ 4.32E-02 \end{Bmatrix}$$

Step 6 Solve for α-vector:

From Equations 46 and 51,

$r = F\alpha$

and,

$$\alpha = \begin{Bmatrix} \dfrac{E_x^{r+1} - E_x^r}{E_x^r} \\ \dfrac{\nu_{xy}^{r+1} - \nu_{xy}^r}{\nu_{xy}^r} \\ \dfrac{\nu_{xx}^{r+1} - \nu_{xx}^r}{\nu_{xx}^r} \\ \dfrac{E_y^{r+1} - E_y^r}{E_y^r} \end{Bmatrix} \begin{Bmatrix} 7.19E-02 \\ -18.26E-02 \\ -13.33E-02 \\ -9.36E-02 \end{Bmatrix}$$

Step 7 Compute New Set of Model Properties:

The new anisotropic properties, α^{r+1} are thus:

$$E_x^{r+1} = E_x^r\left(1+(0.6)(\alpha(1))\right) = (64020.49)(1+(0.6)(7.19E-02)) = 66782.04\ kPa$$

$$\nu_{xy}^{r+1} = \nu_{xy}^r\left(1+(0.6)(\alpha(2))\right) = (0.261)(1+(0.6)(-18.26E-02)) = 0.233$$

$$\nu_{xx}^{r+1} = \nu_{xx}^r\left(1+(0.6)(\alpha(3))\right) = (0.522)(1+(0.6)(-13.33E-02)) = 0.481$$

$$E_y^{r+1} = E_y^r\left(1+(0.6)(\alpha(4))\right) = (174825.17)(1+(0.6)(-9.36E-02)) = 174825.20\ kPa$$

Since all the components in the α-vector are not less than 1% for this iteration, the new set of parameters are used to compute a new model output (calculated strains) and steps 3 through 7 are repeated until the convergence criteria is reached ($\alpha \leq 1\%$).

For this particular example, convergence is reached after seven iterations. The α-values and adjusted model properties are tabulated in Table 12. The shear modulus G_{xy} was not included in the parameter adjustment algorithm because its value, once computed from Equation 39 does not need further adjustment. Typical SID converging processes for moduli, and Poisson's ratios at the stress-state in the example are shown in Figures 10 and 11, respectively. Here, the initial estimates of the moduli and Poisson's ratio were close to the system values and the optimum values were achieved after 7 iterations.

Table 12. Model Properties and Parameter Adjustment Values at Stress State 1 for Well Graded Texas Limestone at Optimum Moisture.

Iteration	α(1)	α(2)	α(3)	α(4)	E_x (MPa)	ν_{xy}	ν_{xx}	E_y (MPa)
1	0.072	-0.183	-0.133	-0.094	64.0	0.261	0.522	175.0
2	0.039	-0.116	-0.098	-0.054	66.8	0.233	0.481	165.0
3	0.020	-0.068	-0.064	-0.033	68.3	0.216	0.452	160.0
4	0.010	-0.038	-0.039	-0.020	69.1	0.208	0.435	157.0
5	0.005	-0.021	-0.023	-0.012	69.6	0.203	0.425	155.0
6	0.003	-0.011	-0.013	-0.007	69.8	0.200	0.419	154.0
7	0.001	-0.006	-0.007	-0.004	69.9	0.199	0.416	153.0

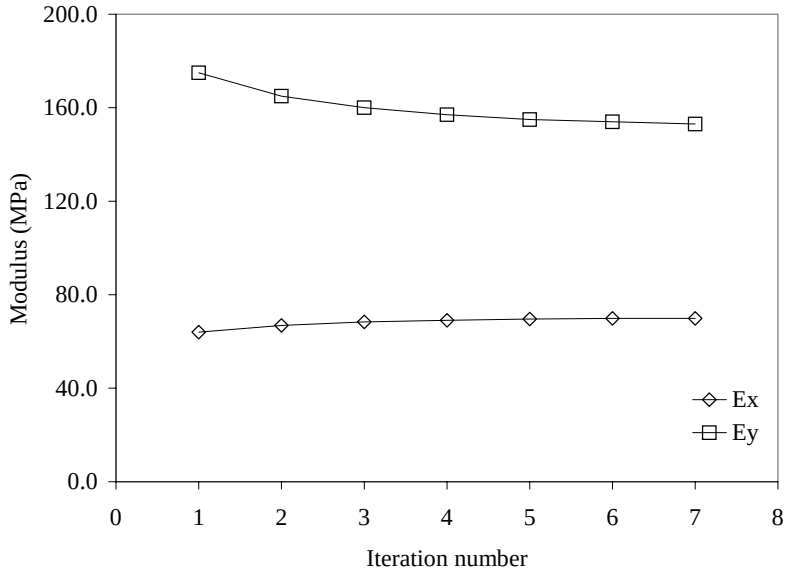

Figure 10. Converging Process for Moduli.

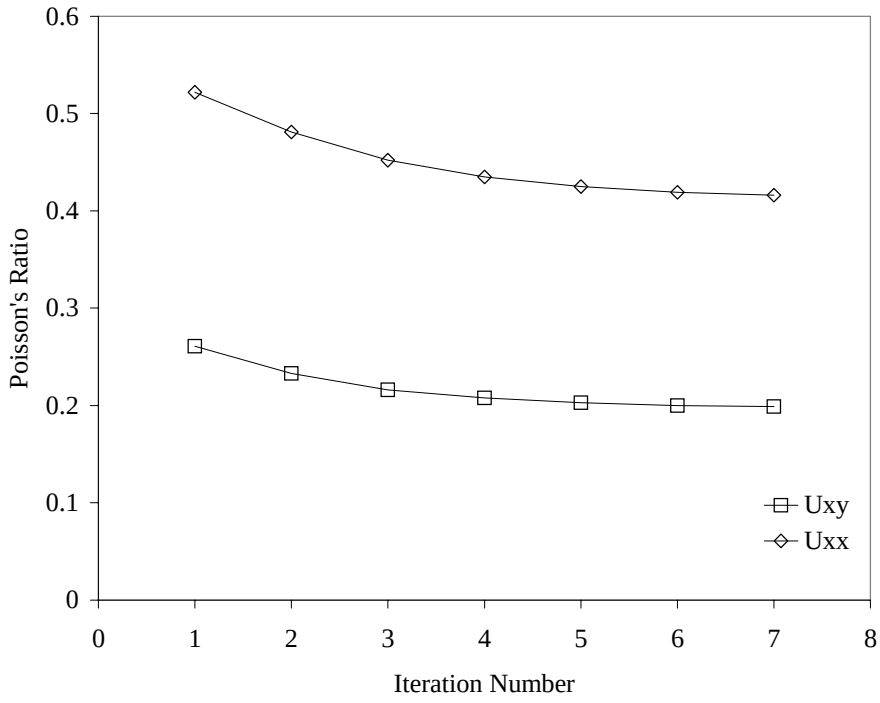

Figure 11. Converging Process for Poisson’s Ratios.

The parameter adjustment algorithm described in steps 1 through 7 was performed on the stresses and strains at all the ten stress states to determine the stress dependent cross-anisotropic resilient properties for all samples. The stresses, moduli and Poisson's ratio obtained using the SID program for a well-graded Texas crushed limestone at optimum moisture is tabulated in Table 13. Similar values were obtained for the other samples and are tabulated in Appendix B. Figures 12 through15 are plots of moduli and Poisson's ratio with normalized stress states ($\sqrt{J'_2}$/Pa and I_1/Pa). Moduli values generally increase with increasing stress levels. Although the moduli values increase with increasing I_1, the moduli tend to peak at high levels of J'_2. This means that resilient moduli values will not increase indefinitely with increasing bulk stresses but will peak at high octahedral shear stresses (Uzan's model).

Table 13. Moduli and Poisson's Ratios for Texas Crushed Limestone at Optimum.

Stress (kPa)		Moduli (MPa)			Poisson's Ratio	
Axial	Radial	Vertical	Horizontal	Shear	Vertical	Horizontal
40.0	25.0	153.0	69.9	42.6	0.199	0.416
50.0	25.0	176.0	69.7	49.7	0.181	0.336
70.0	40.0	241.0	116.0	78.5	0.206	0.385
130.0	60.0	391.0	154.0	106.0	0.176	0.402
150	70.0	448.0	185.0	125.0	0.182	0.406
170	100.0	462.0	249.0	156.0	0.207	0.396
220	120.0	544.0	285.0	178.0	0.187	0.402
250	140.0	616.0	352.0	210.0	0.192	0.417
250	120.0	602.0	288.0	188.0	0.172	0.388
250	105.0	632.0	250.0	171.0	0.166	0.441

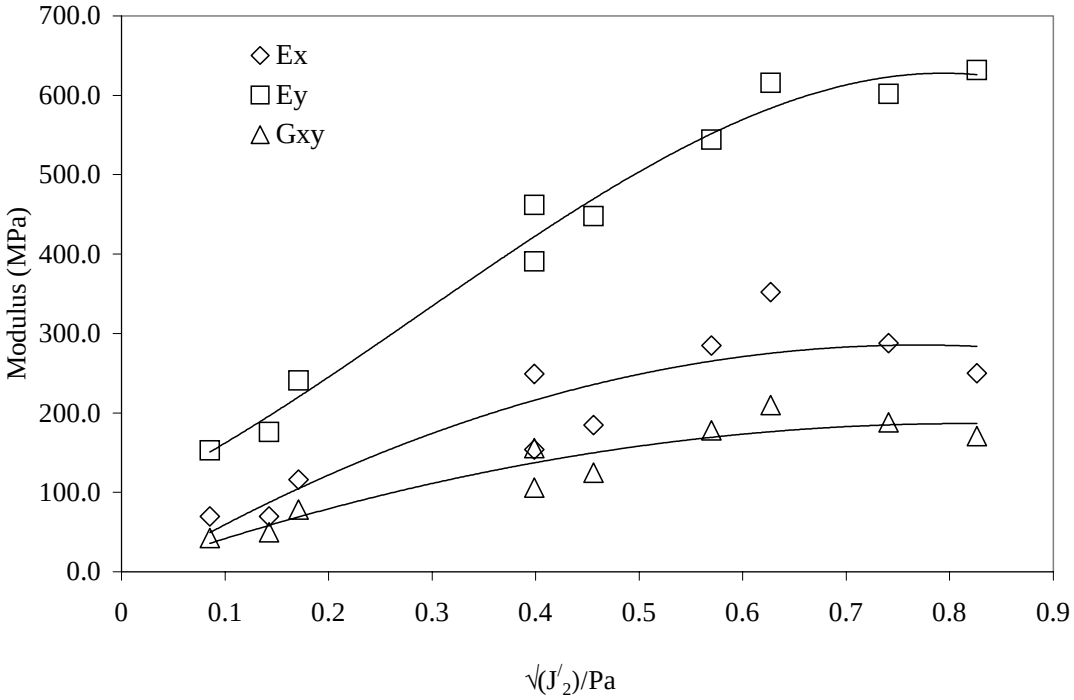

Figure 12. Modulus versus $\sqrt{J'_2}/P_a$.

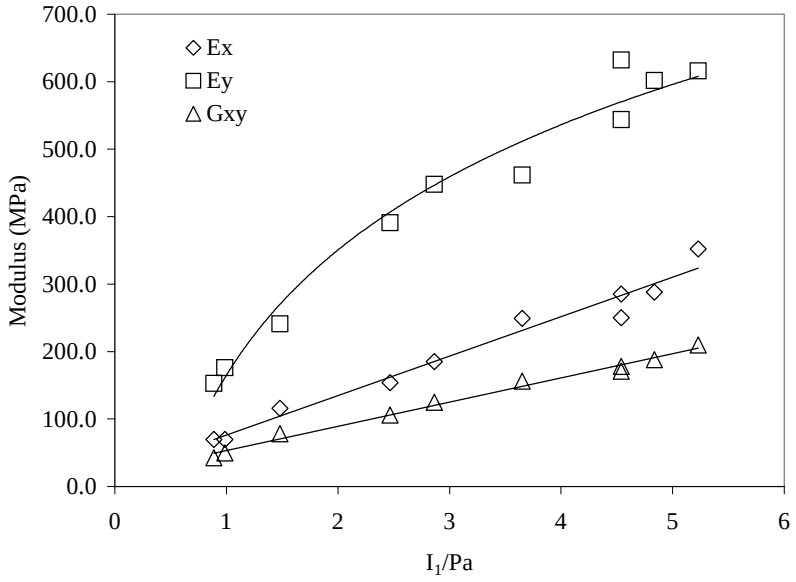

Figure 13. Modulus versus I_1/P_a.

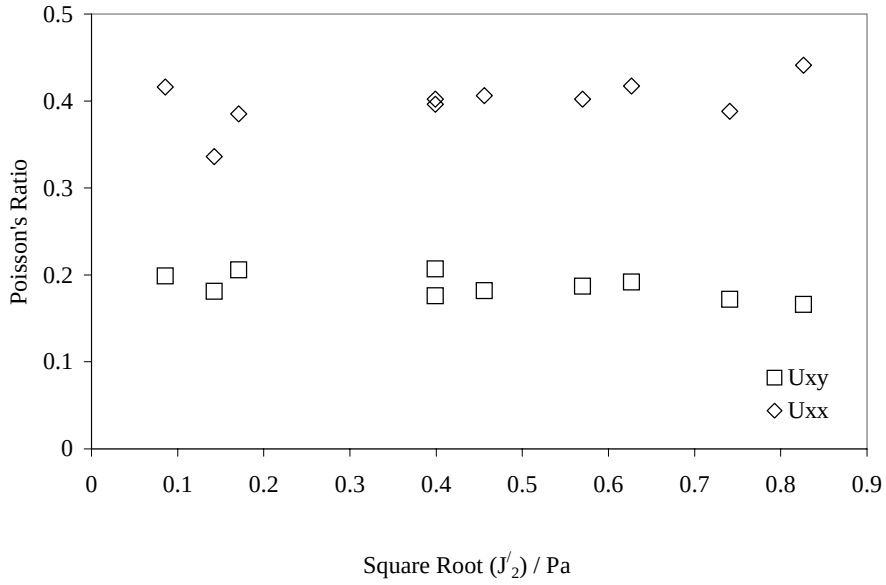

Figure 14. Poisson's Ratio versus Square Root of $(J'_2)/P_a$.

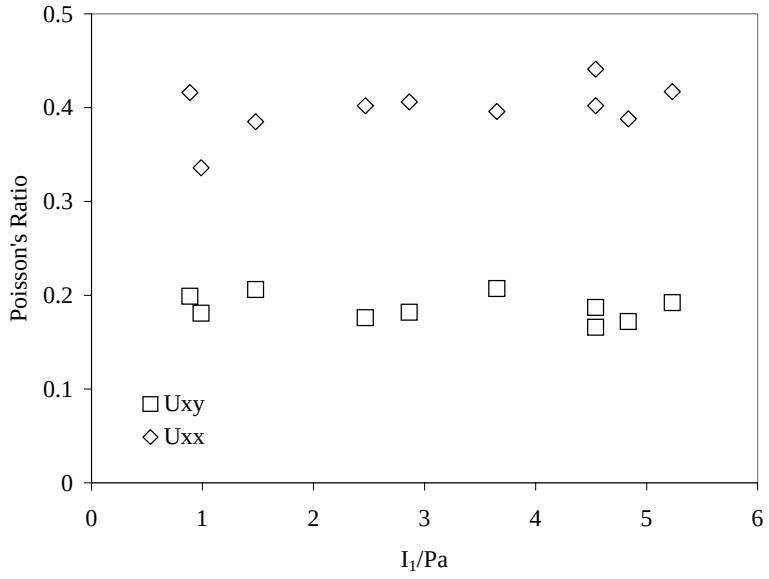

Figure 15. Poisson's Ratio versus I_1/P_a .

In general, resilient modulus values were higher in the vertical direction than in the horizontal direction for all samples. The resilient shear modulus values were the lowest among the three resilient moduli. Also, the horizontal Poisson's ratio always remained greater than the vertical Poisson's ratio.

Gradation, moisture level and material type have different effects on the resilient moduli. For both well- and fine-graded materials compacted at optimum, increased resilient moduli were observed for increasing plasticity index. Figures 14 and 15 are plots of vertical modulus versus $\sqrt{(J'_2)}/P_a$ for well-graded and fine-graded materials at optimum moisture, respectively. California gravel (non-plastic) and Minnesota gravel (PI = 2.0%) recorded lower resilient moduli than Texas gravel (PI = 11.8%) and Texas limestone (PI = 4.4%). However, Texas gravel recorded higher moduli than Texas limestone for well-graded samples and lower values for fine graded samples. Thus, although moduli values increase with increasing plasticity index, there is an optimum plasticity index above which moduli will decrease, especially for fine gradation at wet moisture level.

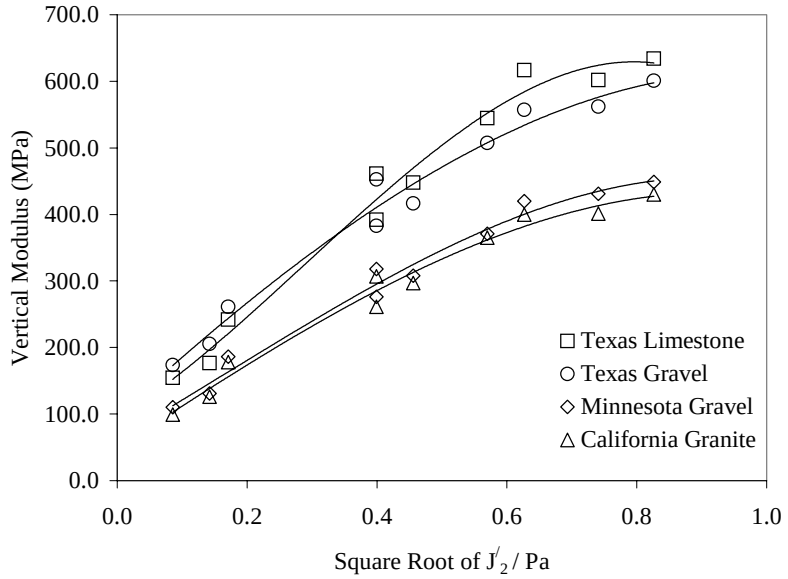

Figure 16. Vertical Modulus for Well-Graded Materials Compacted at Optimum.

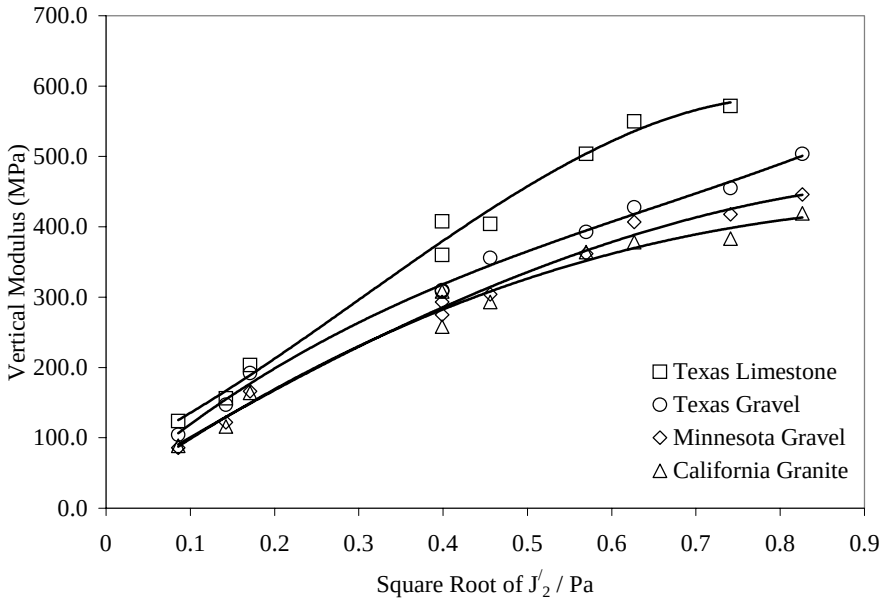

Figure 17. Vertical Modulus for Fine-Graded Materials Compacted at Optimum.

Well-graded samples generally have higher resilient moduli values than coarse graded samples followed by fine graded samples (Figures 18, 19, 20 and 21). This is because the individual particles in well-graded samples are well packed and more stable. The variation in resilient moduli with gradation is more significant in high plasticity materials. Coarse graded samples of Minnesota gravel and California granite could not be compacted and tested because of their low plasticity.

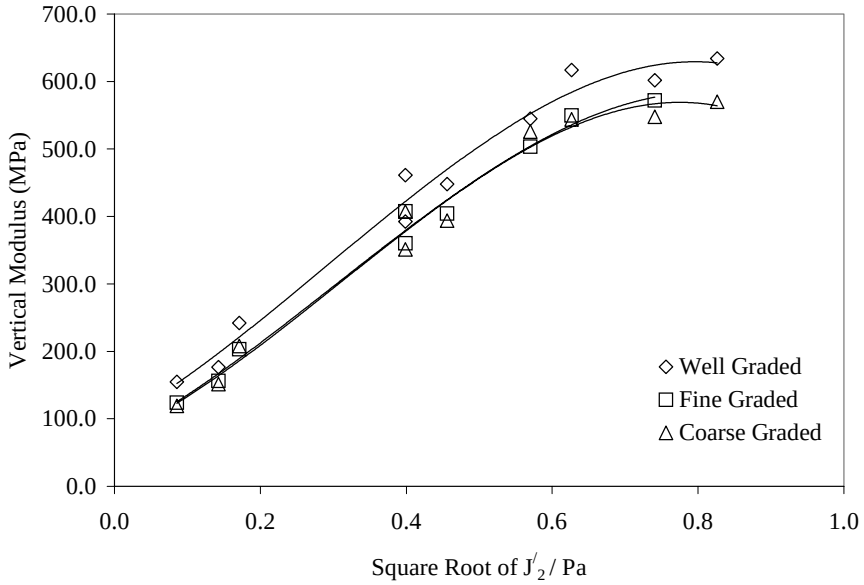

Figure 18. Variation of Vertical Modulus with Gradation for Texas Limestone at Optimum.

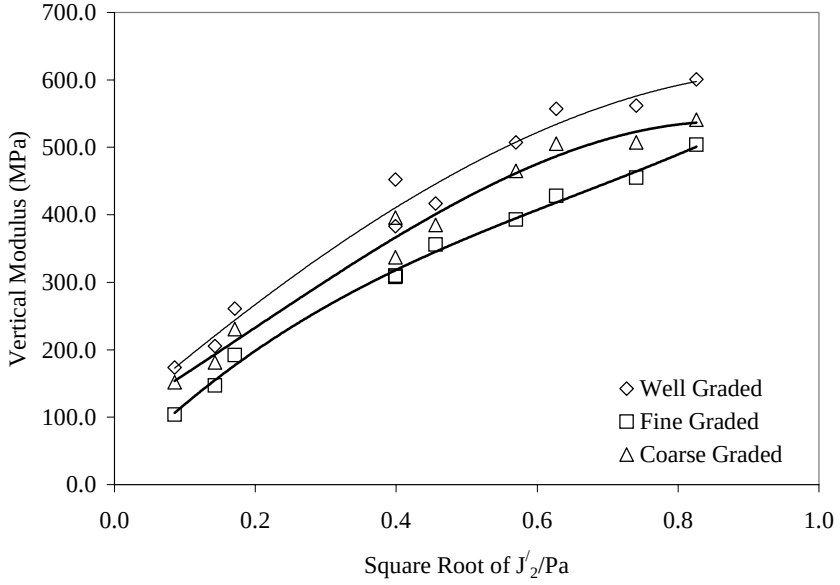

Figure 19. Variation of Vertical Modulus with Gradation for Texas Gravel at Optimum.

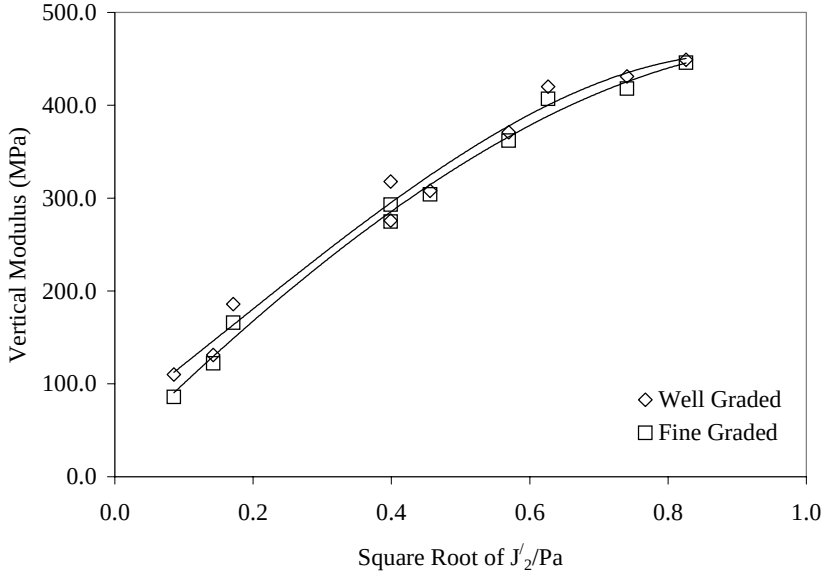

Figure 20. Variation of Vertical Modulus with Gradation for Minnesota Gravel at Optimum Moisture Content.

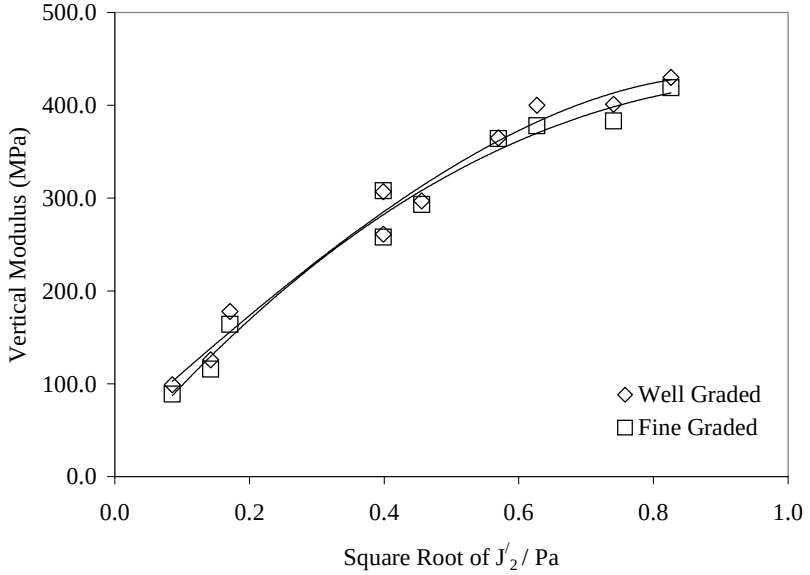

Figure 21. Variation of Vertical Modulus with Gradation for California Granite at Optimum Moisture Content.

For a particular gradation, samples compacted at optimum and dry of optimum generally recorded higher resilient moduli than samples compacted at wet of optimum. The effect of moisture on resilient moduli depends on material and gradation. An increase in plasticity and fine content are generally accompanied by a significant variation in moduli due to moisture. Fine graded Texas gravel and Minnesota gravel samples could not be tested because they were too soft and unstable for the stress levels applied. Figures 22 through 27 illustrate the effect of moisture on resilient moduli. Similar effects were observed for horizontal and shear resilient moduli. The ratios of horizontal to vertical resilient modulus and shear to vertical resilient modulus were fairly constant for all samples tested.

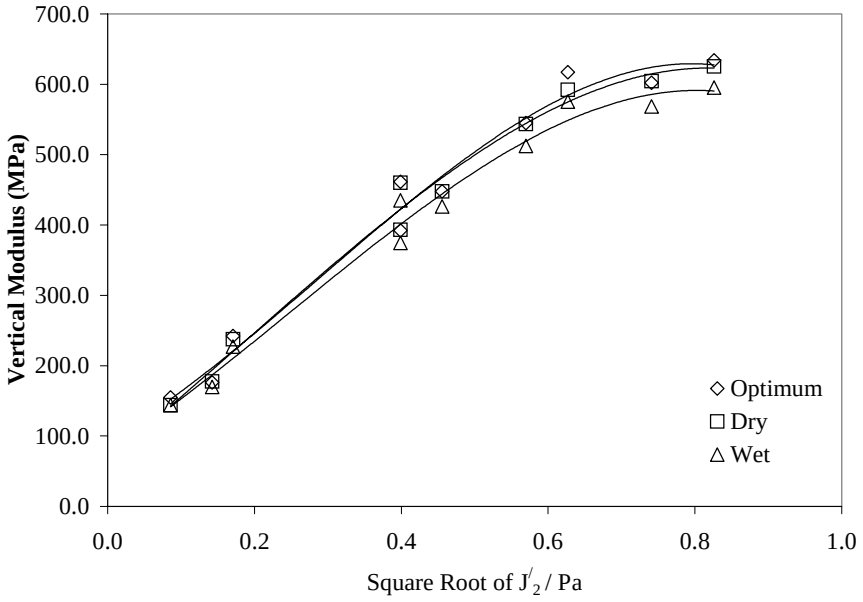

Figure 22. Variation of Vertical Modulus with Moisture for Well Graded Texas Limestone.

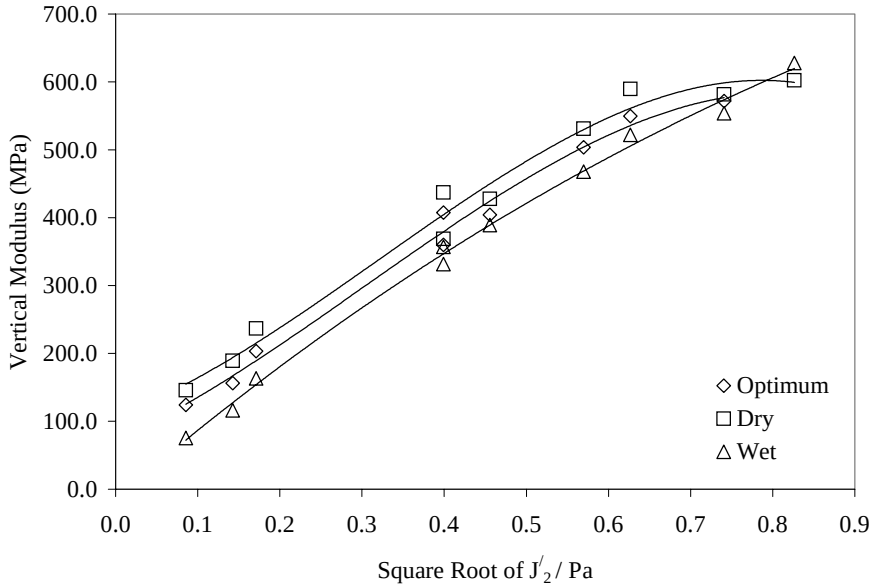

Figure 23. Variation of Vertical Modulus with Moisture for Fine Graded Texas Limestone.

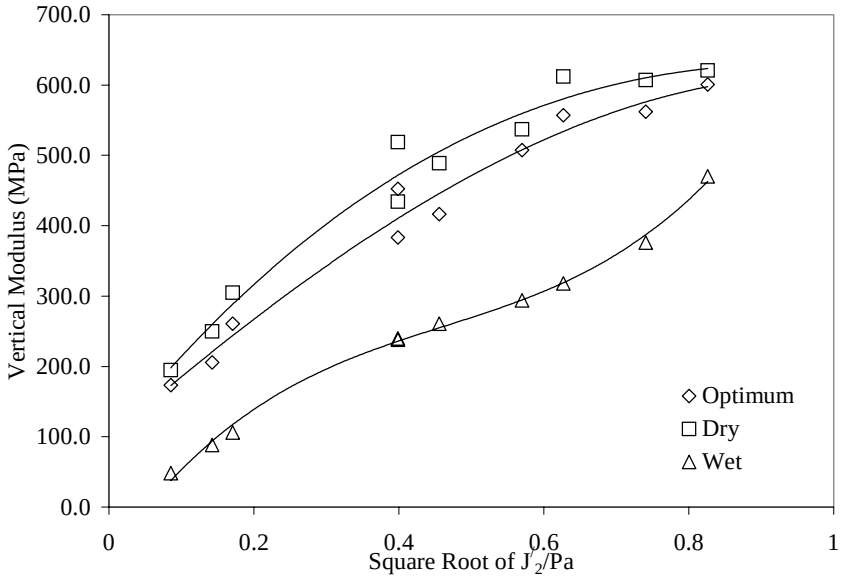

Figure 24. Variation of Vertical Modulus with Moisture for Well Graded Texas Gravel.

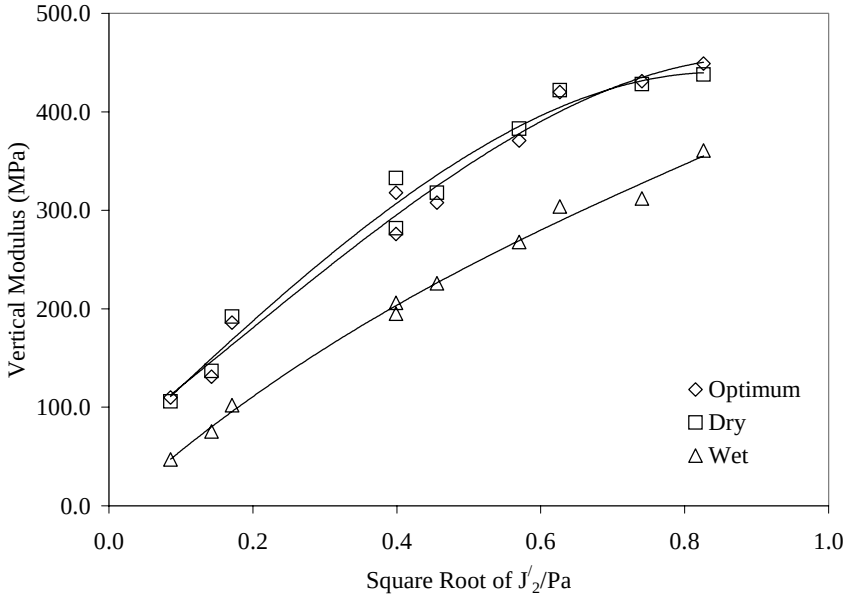

Figure 25. Variation of Vertical Modulus with Moisture for Well Graded Minnesota Gravel.

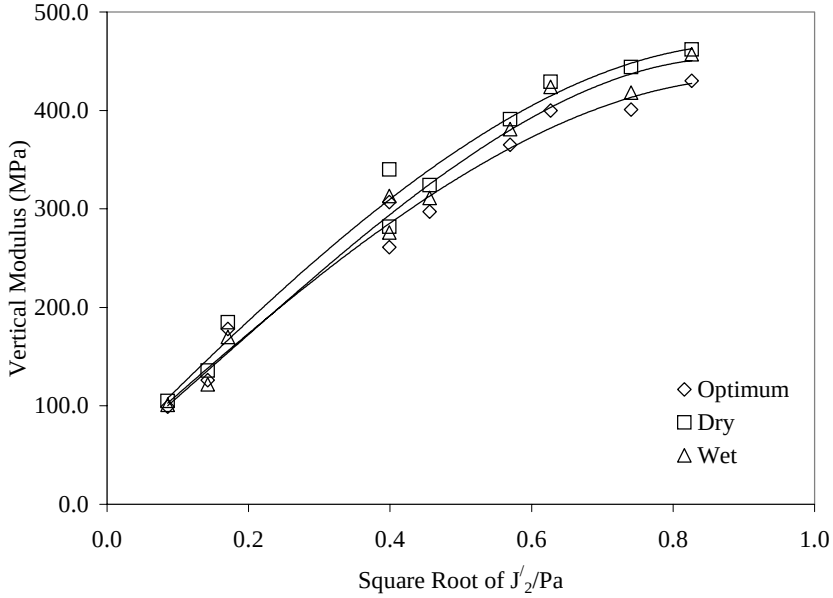

Figure 26. Variation of Vertical Modulus with Moisture for Well Graded California Granite.

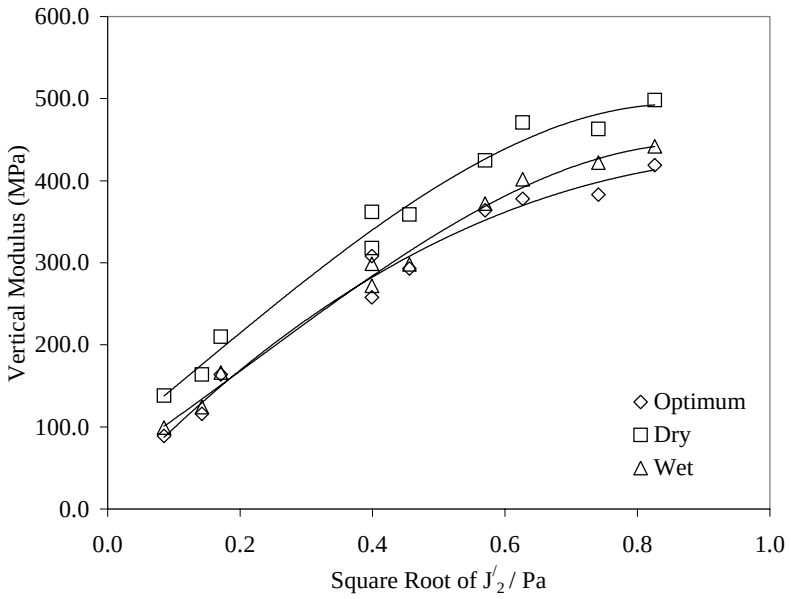

Figure 27. Variation of Vertical Modulus with Moisture for Fine Graded California Granite.

Regression Analysis

It is assumed that the resilient moduli obey the Uzan model and thus, the non-linear tangential moduli are smooth functions of the isotropic stress invariants (Equations 53, 54 and 55). It is also assumed that the variations of these tangential moduli are negligible under infinitesimal changes in stresses at a particular stress state. Thus, the elastic strains generated due to small changes in stresses at a particular stress state depend on the elastic properties at that stress state.

$$E_y = k_1 P_a \left(\frac{I_1}{P_a} \right)^{k_2} \left(\frac{\tau_{oct}}{P_a} \right)^{k_3} \tag{53}$$

$$E_x = k_4 P_a \left(\frac{I_1}{P_a} \right)^{k_5} \left(\frac{\tau_{oct}}{P_a} \right)^{k_6} \tag{54}$$

$$G_{xy} = k_7 P_a \left(\frac{I_1}{P_a} \right)^{k_8} \left(\frac{\tau_{oct}}{P_a} \right)^{k_9} \tag{55}$$

where k_i = material constant determined from regression analysis.

Regression analysis was used to determine the k-values for each gradation and moisture condition. The data fitted well with the Uzan-type models (Equations 53, 54, and 55) and the R-square values determined for the elastic parameters at all conditions were above 0.90. Tables 14, 15, 16 and 17 are summaries of average k-values for the gradation and moisture conditions tested. The negative values of k_6 and k_9 indicate that the horizontal and shear moduli were more sensitive to high shear stress softening.

Table 14. Average k-Values for Texas Limestone.

	Coarse Graded	Well Graded			Fine Graded		
	Optimum	Dry	Optimum	Wet	Dry	Optimum	Dry
k_1	3670	3860	3839	2815	6546	3860	4171
k_2	0.398	0.398	0.369	0.502	0.151	0.398	0.354
k_3	0.314	0.326	0.344	0.154	0.749	0.326	0.362
k_4	426	316	364	180	418	252	429
k_5	1.058	1.281	1.174	1.007	1.132	1.243	1.198
k_6	-0.001	-0.372	-0.303	-0.407	-0.253	0.023	-0.254
k_7	444	380	430	272	302	337	452
k_8	0.878	0.964	0.867	0.899	0.993	0.929	0.910
k_9	-0.068	-0.136	-0.068	-0.150	-0.073	0.159	-0.060

Table 15. Average k-Values for Texas Gravel.

	Coarse Graded	Well Graded		Fine Graded	
	Optimum	Dry	Optimum	Dry	Optimum
k_1	3779	4245	4152	3010	6250
k_2	0.301	0.306	0.299	0.330	0.015
k_3	0.332	0.242	0.316	0.190	0.645
k_4	803	2589	824	1151	416
k_5	0.625	0.483	0.694	0.526	0.961
k_6	-0.053	-0.001	-0.140	-0.247	-0.240
k_7	586	1219	627	680	496
k_8	0.601	0.507	0.642	0.524	0.667
k_9	0.009	0.055	-0.024	-0.103	0.042

Table 16. Average k-Values for Minnesota Gravel.

	Well Graded			Fine Graded	
	Dry	Optimum	Wet	Dry	Optimum
k_1	3879	2834	3232	3779	3462
k_2	0.217	0.360	0.302	0.301	0.248
k_3	0.513	0.310	0.388	0.332	0.372
k_4	169	273	180	280	803
k_5	1.227	1.188	1.267	1.080	0.625
k_6	-0.204	-0.412	-0.405	-0.376	-0.053
k_7	217	322	232	586	331
k_8	0.945	0.861	0.957	0.601	0.791
k_9	-0.066	-0.145	-0.165	0.009	-0.125

Table 17. Average k-Values for California Granite.

	Well Graded			Fine Graded		
	Dry	Optimum	Wet	Dry	Optimum	Wet
k_1	3179	2934	3251	3572	2872	3500
k_2	0.329	0.326	0.313	0.289	0.326	0.262
k_3	0.372	0.366	0.417	0.344	0.376	0.458
k_4	266	266	215	406	366	246
k_5	1.136	1.136	1.229	0.997	0.970	1.123
k_6	-0.404	-0.404	-0.349	-0.356	-0.363	-0.273
k_7	315	277	250	419	379	283
k_8	0.854	0.871	0.951	0.759	0.729	0.866
k_9	-0.146	-0.087	-0.141	-0.132	-0.085	-0.068

DEVELOPMENT OF FINITE ELEMENT PROGRAM

Background

The finite element method has evolved in the past 40 years from a specialized technique for aircraft frame analysis to a general numerical solution to a broad range of physical problems. The historic paper written by Turner, Clough, and Topp (1956) is credited by many for having established the method. Clough (1960) coined the term "finite element method". The finite element method represents an approximate numerical solution of a boundary-value problem described by a differential equation.

Typically engineering problems in mechanics are addressed by deriving differential equations relating the variables of interest to basic principles of physics. These principles include equilibrium, potential energy, strain energy, conservation of total energy, virtual work, thermodynamics, conservation of mass, and many more. Finding a solution that satisfies a differential equation throughout a region, and also yields the boundary conditions is a very difficult and often an impossible task for all but the most elementary problems. The finite element method addresses this difficulty by dividing a region into small sub-regions so that the solution within each sub-region can be represented by a simplified function compared to that required for the entire region. The sub-regions are joined mathematically by enforcing sub-region to sub-region boundary compatibility while satisfying the entire region boundary requirements.

The finite element method is capable of including material and element non-linearity, as well as different types of loading and interface conditions in the solution. This highly efficient and versatile numerical technique has been applied to pavements since the late 1960's. However, one problem that has been identified by many researchers (Duncan *et al.*, 1968; Hicks, 1970) is the false prediction of horizontal tensile stresses within unbound granular layers in flexible pavements. Unbound granular materials are known to have negligible tensile strength aside from that induced by suction and particle interlock. Therefore, they cannot accommodate the high tensile stresses predicted. Contrary to the predicted horizontal tensile stresses, conventional flexible pavements with granular layers have been used to carry traffic loads for decades with a remarkable performance history.

Much research has been directed at improving pavement response models to explain the performance of flexible pavements and to reverse the prediction of horizontal tensile stresses in the unbound granular layers. Three primary approaches have been used to correct the predicted horizontal tensile stresses in unbound granular layers in flexible pavements. These are:

- A no tension analysis based on stress transfer or failure envelop limitations,
- The presence of overburden and compressive residual stresses, and
- Improved constitutive models.

The stress transfer method to correct tension was proposed by Zienkiewicz et al. (1968). In this procedure, equal compressive stresses are applied to counteract predicted horizontal tensile stresses so that equilibrium is maintained. To improve inherent convergence problems in the original stress transfer method, Doddihal and Pandey (1984) modified the technique for pavements.

The Mohr-Coulomb failure envelope criterion has also been incorporated into finite element method programs (ILLI-PAVE and MICH-PAVE) to reverse the prediction of horizontal tensile stresses in unbound granular layers. Here, predicted stresses are adjusted such that they remain within the Mohr-Coulomb failure envelope in the compressive zone.

Residual compressive stresses have also been incorporated into some finite element programs to correct predicted horizontal tensile stresses. Crockford and Bendana (1990) and Tutumluer (1995) successfully incorporated this technique into the TTI-PAVE and GT-PAVE finite element computer programs, respectively. It is believed that residual stresses exist in compacted unbound granular layers. Many researchers (Stewart et al., 1985; Uzan, 1985; Barksdale et al., 1993; Tutumluer, 1995) have investigated the existence of residual stresses. The residual compressive stresses are believed to be in the range of 13.8-kPa to 27.6-kPa (2 to 4-psi).

Some researchers have also worked on improving constitutive models used to describe the dilation behavior of unbound granular materials. Lytton et al. (1993) derived a differential equation describing the variation of Poisson's ratio with stress state. The solution to this differential equation resulted in what is known as the k_1-k_5 model. This model was incorporated in a finite element program (Liu, 1993) and the results were very

impressive. Cross-anisotropy has also been incorporated into finite element programs to improve materials response in unbound granular materials (Zienkiewicz, 1966; Bendana et al., 1989; Tutumluer, 1995). After incorporating anisotropic elastic modeling in the GT-PAVE finite element code, Tutumluer (1995) reported that cross-anisotropic elastic modeling can reduce and even reverse horizontal tensile stresses predicted in unbound granular layers with isotropic elastic model. In his work, Tutumluer (1995) assumed moduli ratios and Poisson's ratios to satisfy strain energy conditions.

Although the no tension correction techniques have been used successfully to reverse predicted horizontal tensile stresses in unbound granular layers, if the constitutive models are accurate enough, such corrections would not be necessary. This research focused much of its attention on improving the cross-anisotropic elastic model (Tutumluer, 1995) with changing Poisson's ratios (Lytton et al., 1993; Liu, 1993). Instead of assuming moduli ratios, one of the main objectives of this project was the development of a laboratory testing protocol for determining the cross-anisotropic elastic parameters of unbound granular materials and correlating the k-values to gradation and moisture parameters, insofar as possible. A triaxial laboratory testing protocol to determine the five cross-anisotropic elastic parameters, which has been elusive to many researchers until now, was developed in this study and discussed earlier.

Finite Element Formulation

A finite element program was developed to model a flexible pavement's response to traffic loads. The finite element procedures and code are derived from the elasto-plastic formulation, originally developed by Owen and Hinton (1980). The code was developed to analyze an axisymmetric problem with material non-linearity. Liu (1993) was the first to modify the original program to analyze pavements. The modification included mesh generation, the implementation of different constitutive models (hypoelastic, hyperelastic, k_1-k_5, and elasto-plastic models), non-symmetric solver and the flexible boundary condition. Park (2000) made further modifications to simplify the code. Both of these modifications included stress dependent Poisson's ratio and non-linear analysis using load increments. The major modification made in this research was to incorporate cross-anisotropic material properties in the code developed by Park (2000).

The principle of virtual work can be used to formulate the finite element method. Consider a solid body Ω, in which the internal stresses σ, the distributed loads per unit volume b and external applied force f form an equilibrium field, to undergo an arbitrary virtual displacement pattern δd^* which results in compatible strains $\delta\varepsilon^*$ and internal displacements δu^*. The principle of virtual work requires that:

$$\int_{\Omega} (\delta\varepsilon^{*T}\ \sigma - \delta u^{*T}\ b) d\Omega - \delta d^{*T}\ f = 0 \tag{56}$$

The expressions for the displacements and strains within any discrete finite element are given by:

$$\delta u^* = N\delta d^* \qquad\qquad \delta\varepsilon^* = B\delta d^* \tag{57}$$

where N is the matrix of shape functions, and B is the elastic strain matrix. Substituting Equation 57 into Equation 56 yields:

$$\int_{\Omega} \delta d^{*T}\ (B^T\sigma - N^T b) d\Omega - \delta d^{*T}\ f = 0 \tag{58}$$

The volume integration over the solid represents the sum of the individual element contributions. Since Equation 58 is true for any arbitrary δd^*, then;

$$\int_{\Omega} B^T\sigma d\Omega - f - \int_{\Omega} N^T b d\Omega = 0 \tag{59}$$

Rewriting Equation 59 in incremental form,

$$\int_{\Omega} B^T d\sigma d\Omega - df - \int_{\Omega} N^T db d\Omega = 0 \tag{60}$$

But the incremental stress-strain relationship is given by:

$$d\sigma = C\delta\varepsilon = CBdu \tag{61}$$

where C is the material constitutive matrix. For an axisymmetric isotropic material model, the matrix C can be written as:

$$C = \frac{E}{(1+\nu)(1-2\nu)} \begin{bmatrix} (1-\nu) & \nu & \nu & 0 \\ \nu & (1-\nu) & \nu & 0 \\ \nu & \nu & (1-\nu) & 0 \\ 0 & 0 & 0 & \dfrac{(1-2\nu)}{2} \end{bmatrix} \tag{62}$$

where E is the elastic modulus and ν is the Poisson's ratio. For an axisymmetric anisotropic material model, the C matrix is given by:

$$C = A\begin{bmatrix} n(1-n\nu_{xy}^{2}) & n(\nu_{xx}-n\nu_{xy}^{2}) & n\nu_{xy}P & 0 \\ n(\nu_{xx}+n\nu_{xy}^{2}) & n(1-n\nu_{xy}^{2}) & n\nu_{xy}P & 0 \\ n\nu_{xy}P & n\nu_{xy}P & (1-\nu_{xx}^{2}) & 0 \\ 0 & 0 & 0 & mPQ \end{bmatrix} \tag{63}$$

where

$$P = (1+\nu_{xx})$$

$$Q = (1-\nu_{xx}-2n\nu_{xy}^{2})$$

$$A = \frac{E_y}{PQ} \tag{64}$$

$$n = \frac{E_x}{E_y}$$

$$m = \frac{G_{xy}}{E_y}$$

Substituting Equation 61 into Equation 60 gives:

$$K_T\,du = df + \int_{\Omega} N^T\,dbd\Omega \tag{65}$$

and,

$$K_T = \int_{\Omega} B^T CBd\Omega \tag{66}$$

In Equation 65, K_T is the global stiffness matrix and the displacement vector du is the only unknown. The solution to Equation 5 can then be solved by conventional matrix inversion methods. The finite element program developed uses an axisymmetric, isoparametric 8-node elements and a 3rd order quadrature with 9 integration points. The material parameters needed to run the finite element program are the non-linear vertical resilient modulus k-values (k_1, k_2, k_3), the moduli ratios (n, m) and the value of the vertical Poisson's ratio as well as the ratio of the horizontal to vertical Poisson's ratios. For the materials tested during this steady, the modular ratios were different for each material but were fairly constant for a particular material at all stress states.

The vertical Poisson's ratio was assumed to be stress-dependent (Lytton et al., 1993; Liu, 1993) as expressed by:

$$\frac{2}{3}\frac{\partial \nu_{xy}}{\partial J_2^{/}} + \frac{1}{I_1}\frac{\partial \nu_{xy}}{\partial I_1} = \nu_{xy}\left[\frac{1}{3}\frac{k_3}{J_2^{/}} + \frac{k_2}{I_1^2}\right] + \left[-\frac{1}{6}\frac{k_3}{J_2^{/}} + \frac{k_2}{I_1^2}\right] \quad (67)$$

A numerical solution to Equation 67 based on the backward difference method was included in the finite element code. Park (2000) described the numerical stepwise solution in detail.

Equation 60 will not generally be satisfied at any stage of computation. An iteration algorithm is included in the program to ensure convergence. There are two convergence criteria in the finite element program. The equilibrium criterion is based on residual force values such that:

$$\frac{\sqrt{\sum_{i=1}^{N}(\psi_i^r)^2}}{\sqrt{\sum_{i=1}^{N}(f_i)^2}} \times 100 \le TOLLER \quad (68)$$

where,

N = the total number of nodal points,

r = the iteration number,

ψ = the total applied force,

f = the applied nodal force, and

TOLLER = tolerance in convergence (percent).

Park (2000) describes the stress dependent criterion in detail. In order to prevent unreasonable predicted moduli values at low stress levels, cutoff values for both the first stress invariant and octahedral shear stress are specified as input in the program. Also the value of the vertical Poisson's ratio was not allowed to exceed 0.48. Although it is common to observe Poisson's ratios above 0.5 for unbound granular materials in the laboratory, the presence of confinement in field conditions prompted the use of 0.48 as the maximum vertical Poisson's ratio.

PAVEMENT ANALYSIS

The elasto-plastic finite element solutions have been observed to be unstable and divergent when the friction angle of unbound granular material is greater than 50º (Liu, 1993). Since the friction angle of unbound granular materials can be greater than 50º, the Uzan's non-linear elastic model (Equation 69) was implemented in the finite element program instead of the elasto-plastic model.

$$E_R = k_1 P_a \left(\frac{I_1}{P_a} \right)^{k_2} \left(\frac{\tau_{oct}}{P_a} \right)^{k_3} \tag{69}$$

The formulation of Equation 69 allows the finite element program to be used to analyze a linear elastic model when the non-dimensional material parameters, k_2, and k_3 are set to zero. Apart from the non-linear material parameters, the moduli ratios (n, m) and the ratio of horizontal to vertical Poisson's ratio (μ) are needed as input parameters. where:

$$\mu = \frac{\nu_{xx}}{\nu_{xy}} \tag{70}$$

A matrix of 27 different pavement sections was analyzed using the finite element program. The pavement sections were selected to investigate the effect of layer thicknesses and subgrade moduli on pavement response using different constitutive models within the unbound granular base course. The pavement matrix is a combination of 50-, 100-, and 150-mm thick hot mix asphalt (HMA) layers on 150-, 300-, and 450-mm thick base courses resting on sub-grades with stiffness of 20.7-, 103.4-, and 206.8-MPa. The pavement structure is shown in Figure 28. A standard wheel load of 40 kN was modeled to the surface of each pavement. The loads are assumed to be uniformly distributed over circular areas with radii of 136-mm each.

The pavements were analyzed using linear isotropic, non-linear isotropic, linear cross-anisotropic and non-linear cross-anisotropic constitutive models for the base course. The base material properties used in the analysis are those of a well-graded crushed limestone, compacted at optimum moisture. For all the pavements analyzed in the matrix, the HMA layers and sub-grades were assumed to be non-linear isotropic. Thus, a total of 108 computer runs were performed using the finite element program to

predict the pavements' response to a standard wheel load. Table 18 is a summary of the material properties used in the analysis.

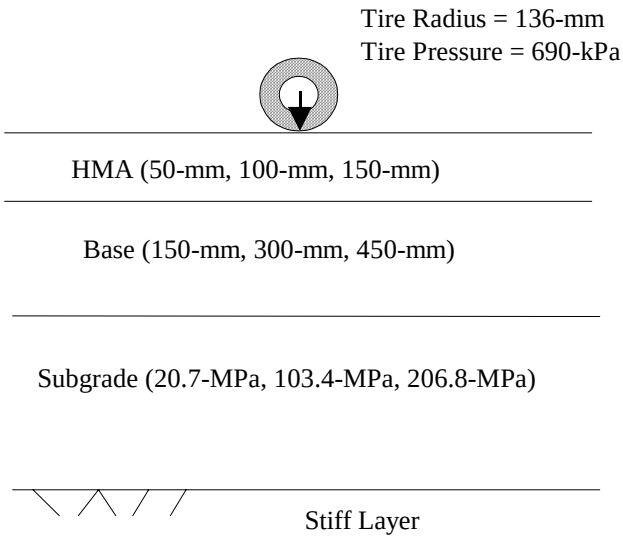

Figure 28. Pavement Structure for Finite Element Analysis.

Table 18. Pavement Material Properties.

HMA Layer (Non-linear Isotropic Model)			
k_1 = 28,000 k_2 = 0.100 k_3 = 0.001			
n = 1.00 (Equation 9) m = 0.38 (Equation 9) ν_{xy} = 0.35 μ = 1.00 (Equation 14)			
Base Course			
Linear Isotropic	Non-Linear Isotropic	Linear Cross-Anisotropic	Non-Linear Cross-Anisotropic
k_1 = 3,500	k_1=3,500	k_1=3,500	k_1=3,500
k_2 =0.0, k_3=0.0	k_2=0.455, k_3=0.295	k_2=0.0, k_3=0.0	k_2=0.455, k_3=0.295
n =1.0, m=0.38	n=1.0, m=0.38	n=0.5, m=0.38	n=0.5, m=0.38
ν_{xy}=0.2, μ = 1.0	ν_{xy}=0.2, μ = 1.0	ν_{xy}=0.2, μ = 1.5	ν_{xy}=0.2, μ = 1.5
Sub-grade (Non-linear Isotropic Model)			
k_1 = 207, 1035, 2070 k_2 = 0.001 k_3 = 0.300			
n = 1.00 m = 0.38 ν_{xy} = 0.35 μ = 1.00			

A typical axisymmetric finite element mesh used in the finite element analysis is shown Figure 29. The nodal radial strains were assumed to be negligible at approximately 10 times R (radius of loaded area) from the area of applied wheel load. Also, the nodal stresses and displacements were assumed to be negligible at 20 times R below the pavement surface.

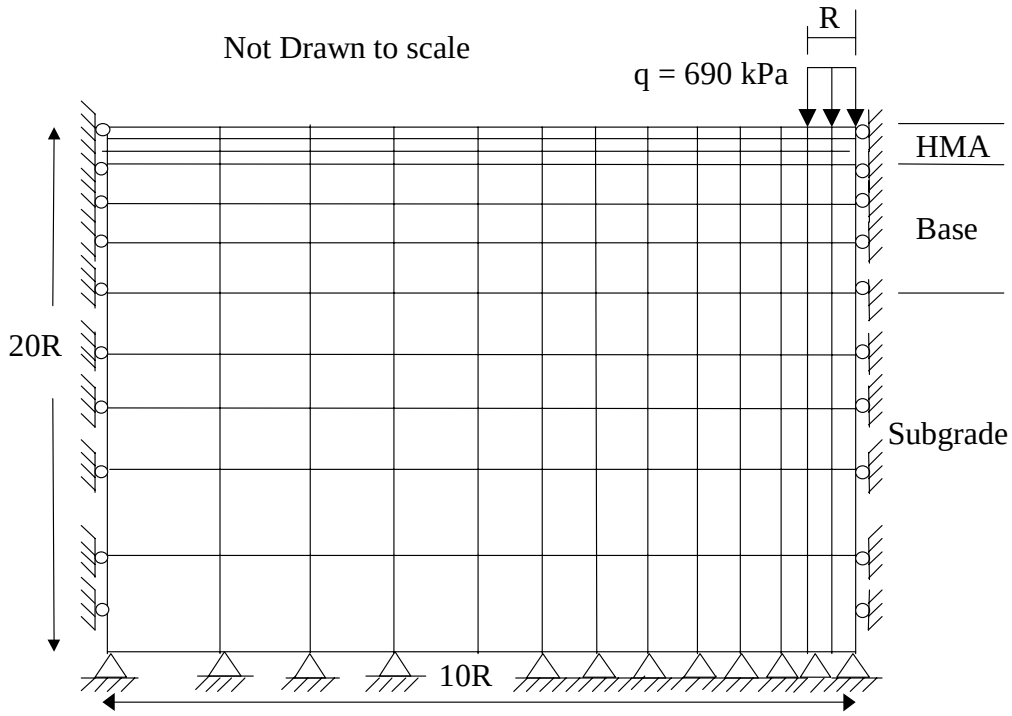

Figure 29. Typical Finite Element Mesh for Pavement Analysis.

Typical plots of vertical and horizontal stress distribution within the unbound granular base course at the center of loaded area are plotted in Figures 30 through 35 for a pavement section with 50-mm HMA layer, 300-mm base layer and 20.7-MPa, 103.4-MPa, and 206.8-MPa moduli sub-grades. Similar trends were obtained on the other pavement sections, and the plots are shown in Appendix C. The finite elements program adopts a compression-is-negative sign convention. Gravity stresses due to overburden load and residual compaction stresses were not included in the finite element analysis because more emphasis was placed on constitutive modeling.

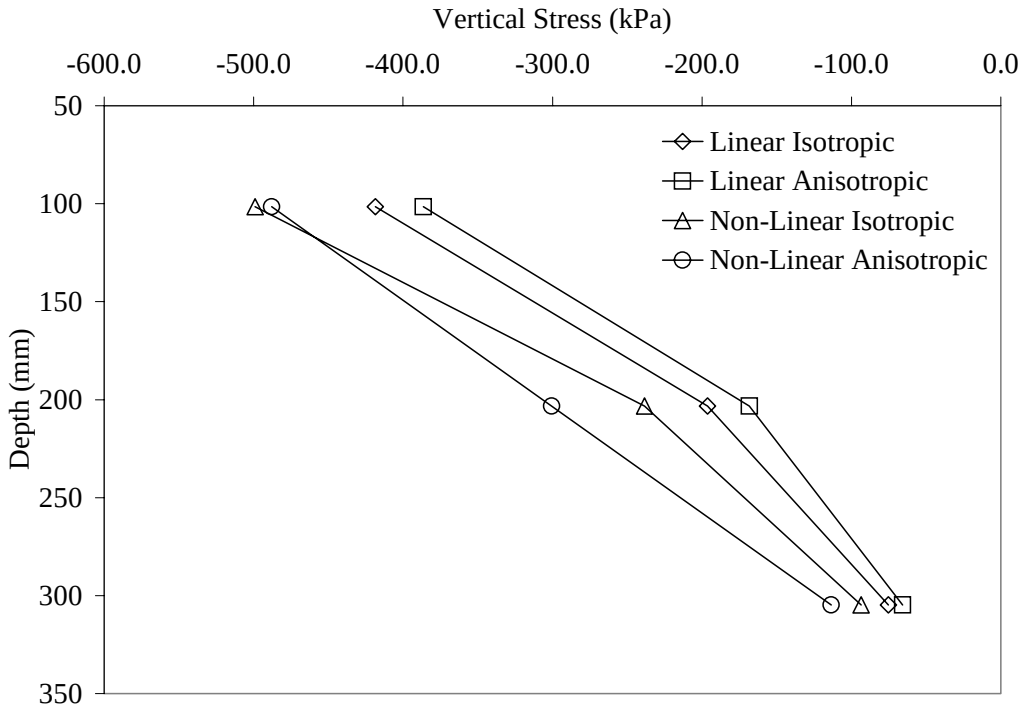

Figure 30. Vertical Stress for 50-mm HMA, 300-mm Base, and 20.7-MPa Sub-grade.

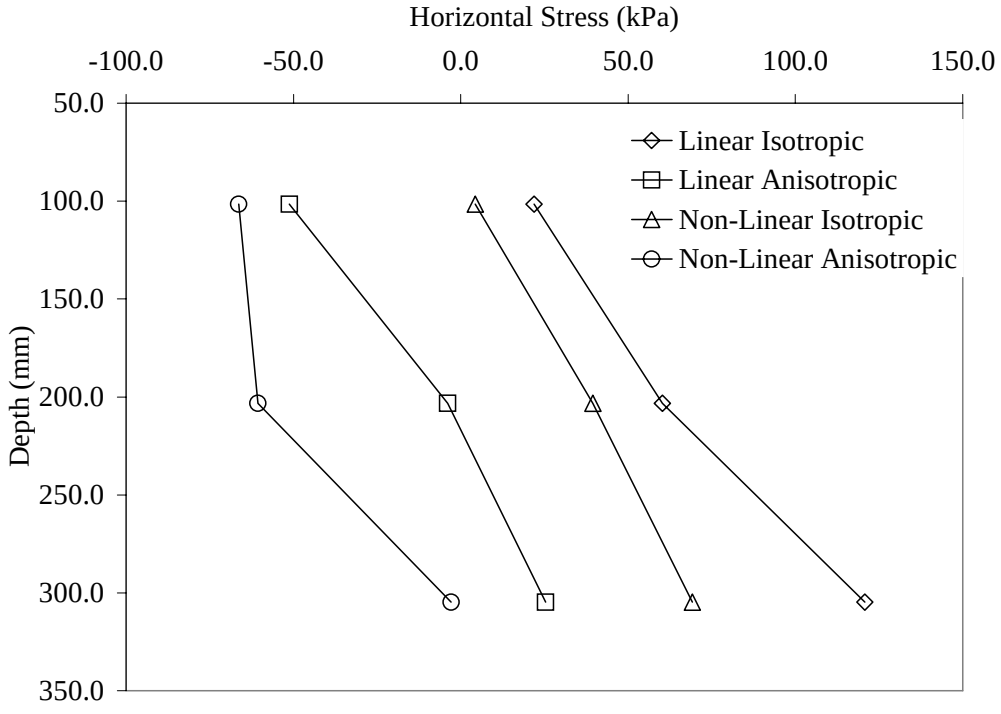

Figure 31. Horizontal Stress for 50-mm HMA, 300-mm Base, and 20.7-MPa Sub-grade.

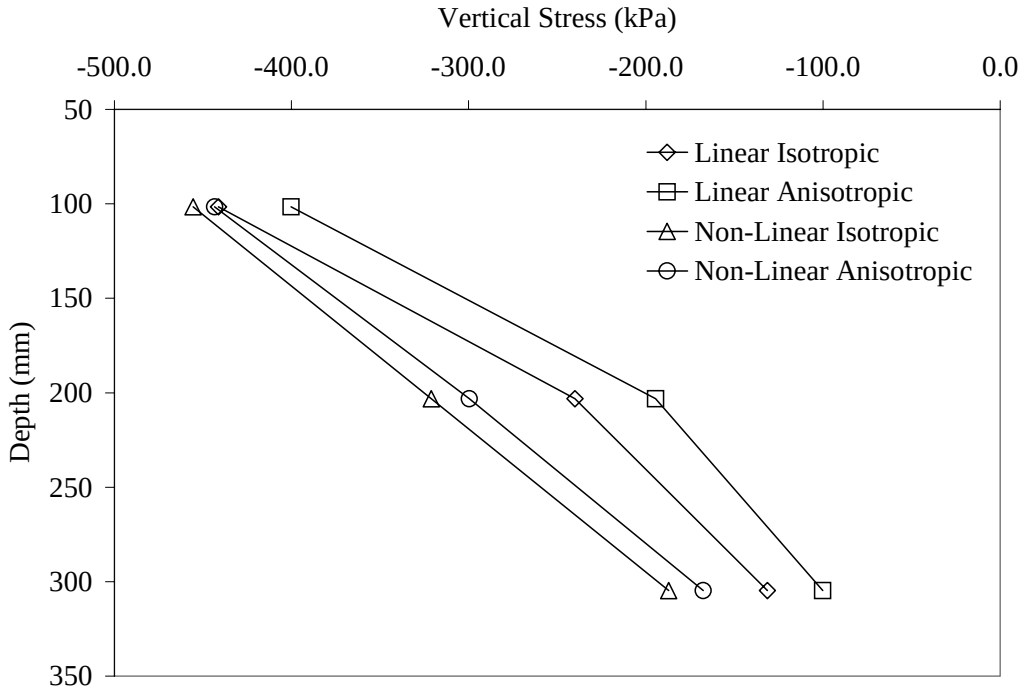

Figure 32. Vertical Stress for 50-mm HMA, 300-mm Base, and 103.4-MPa Sub-grade.

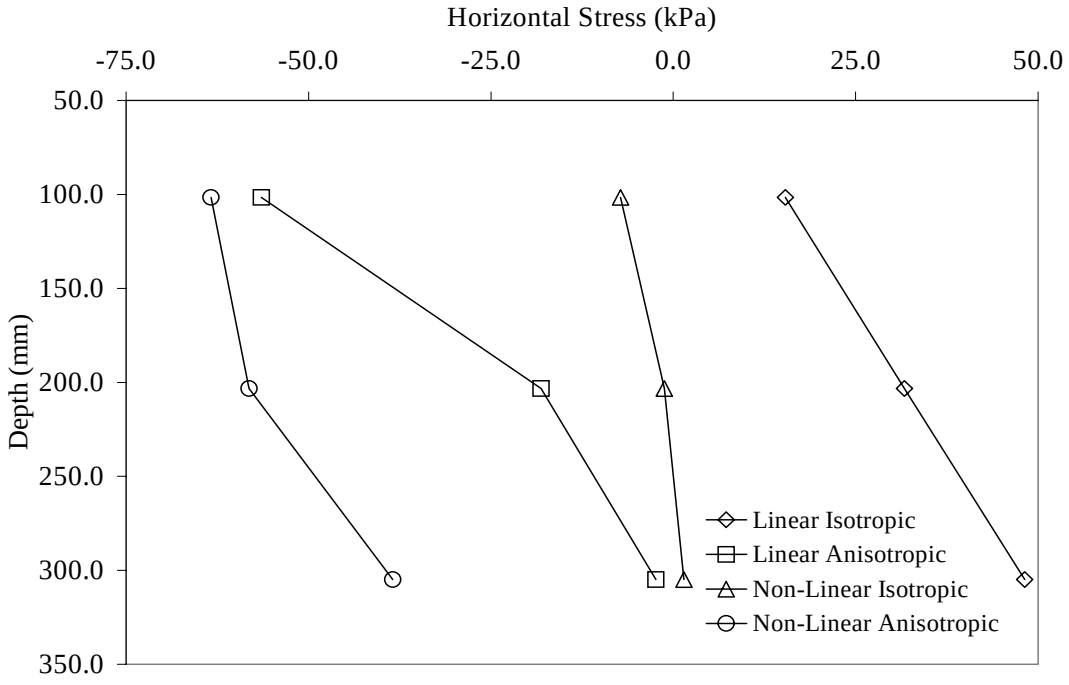

Figure 33. Horizontal Stress for 50-mm HMA, 300-mm Base, and 103.4-MPa Sub-grade.

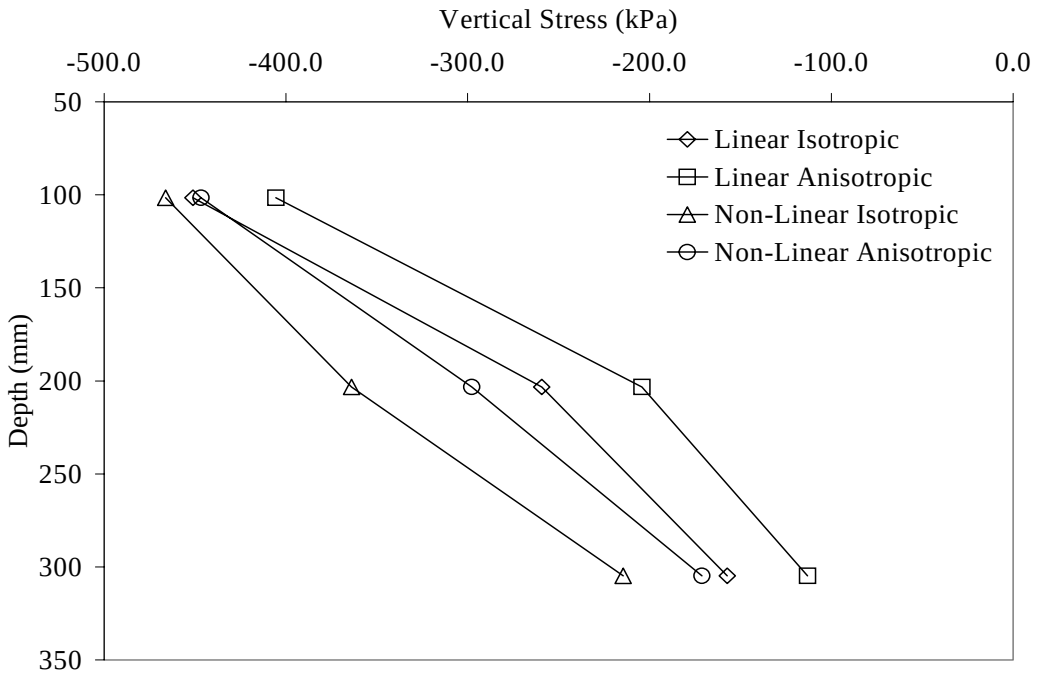

Figure 34. Vertical Stress for 50-mm HMA, 300-mm Base, and 206.8-MPa Sub-grade.

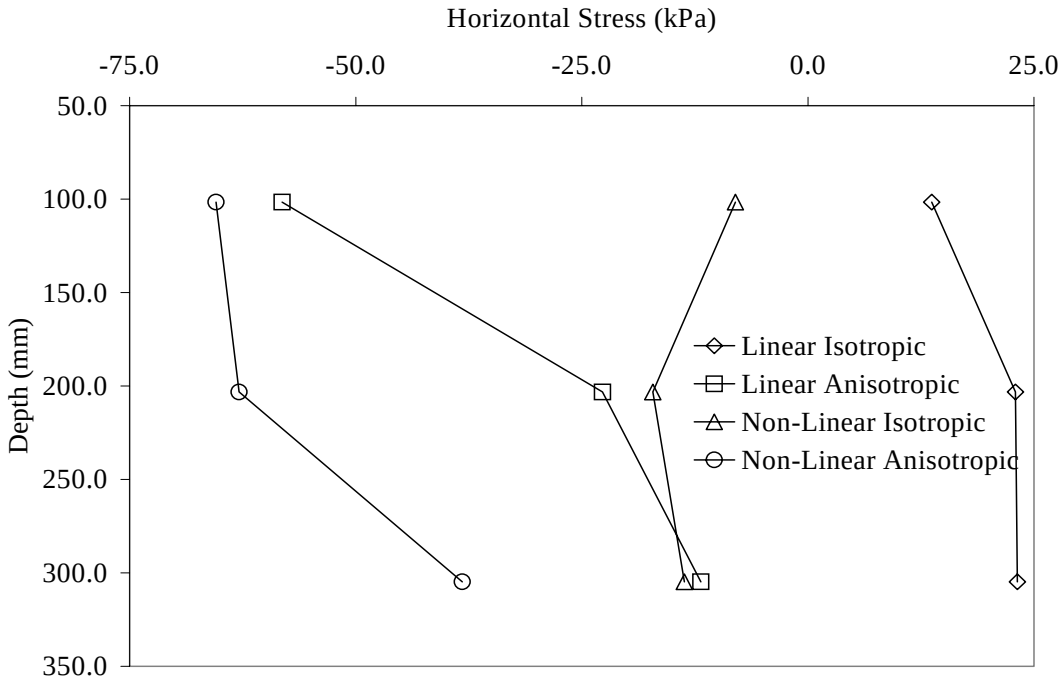

Figure 35. Horizontal Stress for 50-mm HMA, 300-mm Base, and 206.8-MPa Sub-grade.

Different trends were observed in the distribution of vertical and horizontal stresses within the unbound granular base course. Variation in layer thickness, the constitutive model used to characterize the base layer and sub-grade moduli have a significant effect on the distribution of stresses. The contributions of these factors to the way stresses are distributed in the base layer are discussed in the following section.

Constitutive Models

Pavement sections were analyzed using different material constitutive models within the unbound granular base layer. The models considered were:

- Linear isotropic,
- Non-linear isotropic,
- Linear cross-anisotropic, and
- Non-linear cross-anisotropic.

The distributions of vertical compressive stresses within the base layers do not follow an exact trend with respect to the models considered for the pavement sections. In a majority of the pavement sections evaluated, lower vertical stresses were observed with the linear anisotropic model. The layer thickness and sub-grade moduli more significantly affect the distribution of vertical stresses than material constitutive models.

The effect of material constitutive models on pavement response is more pronounced in the distribution of horizontal stresses within the unbound granular base layer. Horizontal stress distribution within the base layer follows a particular trend with respect to material constitutive modeling. The magnitude of the horizontal stress at a point within the base course depends on the layer thickness and subgrade modulus but, whether the stress is compressive or tensile is dictated by the material constitutive model used.

In all the pavement sections analyzed, cross-anisotropic models significantly eliminated the false tension zones predicted by isotropic models. The linear isotropic model always predicted increasing horizontal tensile stresses within the depth of the unbound granular base layer. Although non-linear isotropic modeling significantly reduced the magnitude of the tensile horizontal stresses predicted by linear isotropic modeling, tension zones still existed in the base layer for most of the pavement sections. The only pavement sections where some compressive stresses were observed with the

non-linear isotropic model were pavements with very high sub-grade modulus. Increasing the base layer thickness decreased the magnitude of the horizontal tensile stresses but did not remove the presence of tension zones.

Except for a few pavement sections, especially weak subgrade, horizontal compressive stresses were predicted with linear cross-anisotropic modeling. Non-linear cross-anisotropic models were observed to always predict compressive horizontal stresses, and the magnitudes of these stresses were higher than those predicted by linear anisotropic model.

Modeling the unbound granular base layer as linear isotropic, non-linear isotropic, linear anisotropic and non-linear anisotropic in that order, gradually shifts from a tension zone to a compressive zone. This observation implies that if appropriate models are used to characterize the behavior of unbound granular materials, the base layers are capable of mobilizing enough confinement to withstand wheel loads. This is in agreement with the observation made by Barksdale, Brown & Chan (1989) that linear cross-anisotropy is equal to or better than a more complicated non-linear isotropic model for predicting unbound granular layer response to traffic loads. It is the ability of unbound granular layers to develop confinement that can be used to explain their historic performance in flexible pavements. The confinement can be used to confirm a comment made by Lytton (1998) that immediately beneath a tire load; an unbound granular layer generates its own lateral confining pressure and becomes very stiff almost as if it were forming a moving vertical column that travels along with the load. This is illustrated in Figure 36. The presence of confinement within the unbound granular base layer means that a tension zone does not exist as predicted by isotropic modeling. Also, there is an increase in bulk stress and modulus to facilitate the spread of wheel loads.

Determining the stress profile within a pavement is important for accurate prediction of permanent deformation. Researchers and Engineers agree on the existence of confinement in unbound granular base layers for spreading wheel loads. Non-linear cross-anisotropic modeling has recently been reported (Adu-Osei *et al*., 2000; Tutumluer, 1995, 1999) as a superior model for predicting the behavior of unbound granular materials. It has been difficult to absolutely establish and quantify the extent of confinement in base layers but the non-linear cross-anisotropic elastic model with

changing Poisson's ratio can be used to explain this important phenomenon in unbound granular layers.

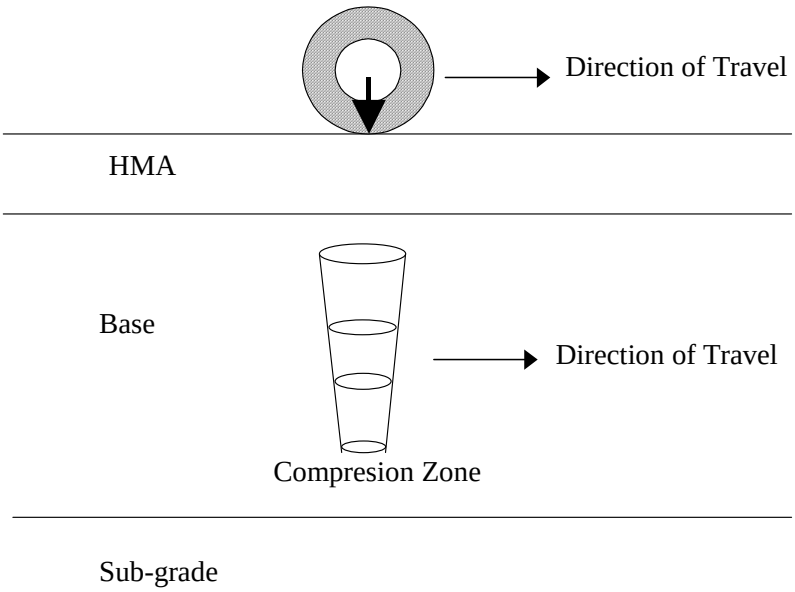

Figure 36. Illustration of Compressive Zone in Unbound Granular Layer.

Layer Thickness

For a given base layer thickness and subgrade modulus, increasing the thickness of the HMA layer decreases the magnitude of the vertical and horizontal stresses at any point in the base layer. Similar trends were observed in increasing the base layer thickness for a given HMA layer and sub-grade modulus.

Increasing the HMA or base layer thickness did not explain the existence of tension or compression zone in the unbound granular base layer. Thus the design philosophy in which the thickness of the unbound granular base layer is increased until the tension zone as predicted by isotropic elastic methods diminishes is too conservative. This design practice would result in pavement sections that are not economical, and are much thicker than base layers that perform well in the field.

Subgrade Modulus

The subgrade moduli values of 20.7-, 103.4-, and 206.8-MPa used in this study represent a weak, strong, and chemically stabilized subgrade, respectively. Increasing the subgrade modulus did not significantly change the distribution of vertical stresses within the base layer.

For a given pavement section, an increase in subgrade modulus did not significantly change the horizontal compressive stresses predicted with the non-linear cross-anisotropic model. However, the following were observed for the other material models:

- Increasing subgrade modulus shifted the few tension zones predicted by the linear cross-anisotropic model into compression zones.
- Increasing subgrade modulus shifted most of the tension zones predicted by non-linear isotropic model into compression zones.
- Although the magnitudes of the stresses in the tension zones predicted by linear isotropic modeling were significantly reduced, increasing the subgrade modulus did not remove the presence of tension zones in the base layer

It must also be noted that magnitudes of the horizontal compressive stresses predicted by the linear cross-anisotropic and non-linear isotropic models, as a result of subgrade improvement, were still lower than the insignificant changes in stresses predicted by the non-linear cross-anisotropic model.

The higher compressive stresses in the non-linear cross-anisotropic predictions predict not only a stiffer base course under load but, also the potential for accelerated rutting due to an incremental build-up of pore-water pressure with repeated traffic loading. This tendency will be greater in those base courses with higher percents of plastic fines.

SPECIAL STUDIES: SAMPLE SIZE EFFECTS

Two special studies were conducted to evaluate the effect of compaction method and effort, and sample size on the resilient properties of unbound granular materials. The details are discussed in the following sections.

Background

The study of the mechanical properties of soils calls for a test in which principal stresses and strains that span the range of expected conditions can be evaluated so that extrapolations used by structural models are kept to a minimum. The most convenient standard test, which allows for the direct measurement of principal stresses and strains, is the cylindrical triaxial test (Figure 37). The shape of the sample required is simple and practical for both field representation and easy laboratory preparation. The minor principal stress, σ_3, and intermediate principal stress, σ_2, equal to the confining stress applied to the sample. The triaxial test has been used with notable success in the field of geotechnical engineering and its principles have been extended to the field of pavement engineering.

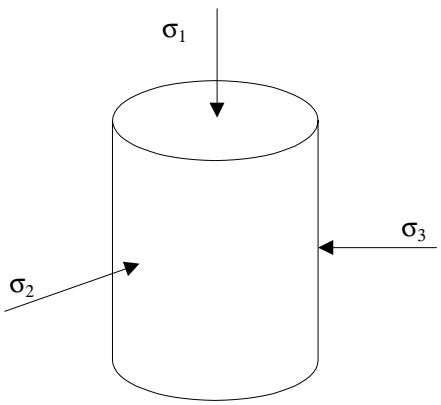

Figure 37. Cylindrical Triaxial Test.

In geotechnical engineering the triaxial test is used to determine the shear strength parameters of soils. The problem being analyzed usually dictates the rate of shear and drainage conditions applied to the cylindrical sample.

Some modifications have been made to the traditional triaxial test for pavement engineering applications. In pavement engineering, the repeated load triaxial test is preferred to the triaxial shear test. The repeated load triaxial test has been developed and used in the U.S. for pavement application since the 1950's (Seed *et al.*, 1955). The measurement of principal stresses and strains are maintained but unlike the traditional triaxial shear test, transient loads which are well below failure stresses are applied to a cylindrical sample of pavement material. Also, strict drainage conditions and sample consolidation are not enforced. Triaxial testing data have been used to provide input for the material properties in pavement structural models to determine the stresses and strains that lead to performance predictions.

In the repeated load triaxial test, a static confining stress is usually applied to the cylindrical sample and a deviatoric stress is axially cycled for a predetermined number of times. The transient loads are chosen so that they best represent typical stress conditions within a pavement. Charts are available that can be used to select the cycle of a transient load (Barksdale, 1971). A typical transient load consists of a 1.0-second cycle sinusoidal load consisting of 0.1-second load duration and a 0.9-second rest. This load cycle simulates the application of traffic loads on the pavement.

Due to the transient nature of loading, strains are separated into an elastic or resilient part, for resilient modulus, and a plastic part, for permanent deformation.

Sample Size

The main disadvantage of the cylindrical triaxial test is the non-uniform distribution of stresses and deformations within specimens. This non-uniformity is mainly caused by the presence of friction at the soil-platen interface (Figure 38). The friction is a result of soil-platen interaction and it is compounded by rubber bands (O-rings) used to rigidly secure the membrane around the sample to the top and bottom platens. This problem has been addressed by using lubricated platens for the triaxial test.

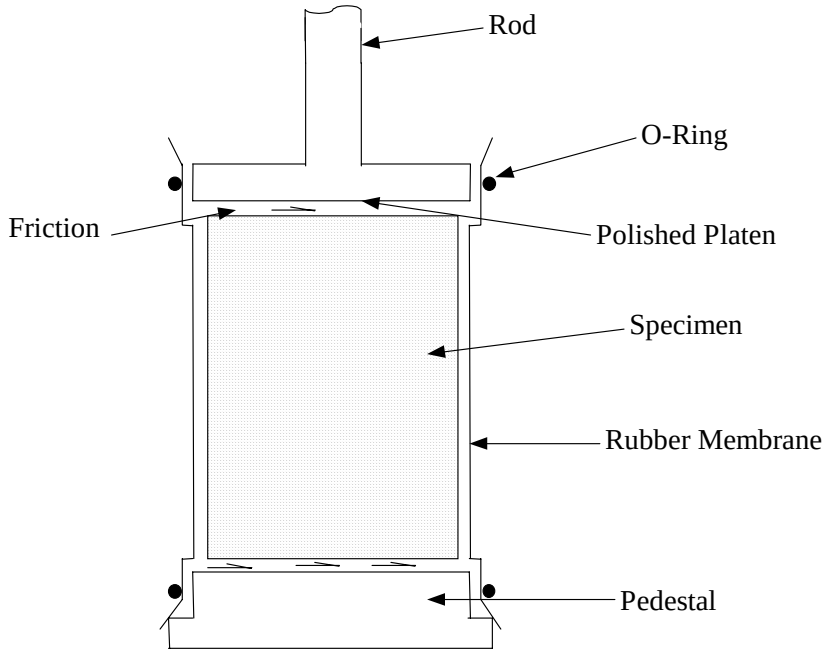

Figure 38. Triaxial Tests Set-up.

Experimental work done by Taylor (1941) indicates that reliable results could be obtained with soil specimens having regular ends provided the slenderness (length to diameter ratio, l/d) is in the range of 1.5 to 3.0. According to Lee (1978) this study established the standard that the slenderness (l/d) of triaxial specimens for soil be limited to 2.0-2.5 for test with regular ends. Since then, many researchers (Rowe *et al*., 1964; Bishop *et al*., 1965; Duncan *et al*., 1968; Lee, 1978) have studied end restraint effects on the shear strength of soils and concluded that sample slenderness can be reduced to l/d = 1 if frictionless platens are used. Rowe and Barden (1964) concluded that if the friction angle between the soil and the end platen can be kept below 1°, end restraint effects can be considered negligible and the end platens can be considered to be ‘‘frictionless’’.

The drained shear strength of soils using regular ends and l/d = 2.0 are reduced by up to 10% when frictionless ends are used. For an undrained test, the shear strength is reduced by about up to 5% when frictionless ends are used. Consider a failed cylindrical soil sample with ϕ-value of 40°, where the failure plane makes an angle θ with the

horizontal, then fundamentals of geometry (Figure 39) suggests that the height to diameter ratio of the sample must be tan (45+ϕ/2) = 2.1.

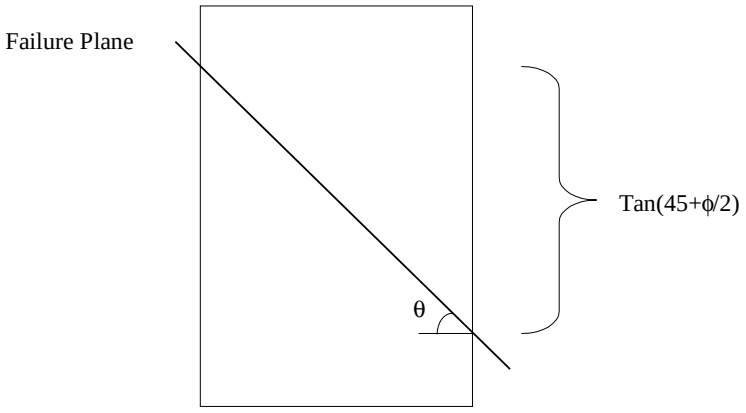

Figure 39. Failed Cylindrical Sample.

Frictionless ends allow the use of shorter sample sizes (l/d = 1) in a triaxial test. Laboratory samples with a height to diameter ratio of 1:1 appear to be more stable and practical for unbound granular layers in pavements. Unbound granular layers in pavements are usually compacted in lifts of 150-mm (6-in) to reduce the existence of density gradients. However, the conventional 2:1 sample height to diameter ratio in the traditional triaxial shear test has been maintained in the development of repeated load triaxial test for pavement application. It is important to know whether maintaining a 2:1 sample size is better than the more stable and practical 1:1 sample size.

Any triaxial set up that can improve and reduce friction at the end platens and allow the use of 1:1 sample sizes would be more practical. Faster triaxial cells have recently been designed and manufactured. Probably the most notable of these is the Industrial Process Control (IPC) of Australia's Rapid Triaxial Tester (RaTT) which has successfully been used at Texas Transportation Institute (TTI), University of Illinois (UI) and else where.

Unlike the traditional triaxial cell, the RaTT cell (Figure 40) uses a larger diameter confining cylinder around the specimen, which is fitted with an internal rubber membrane that can be inflated to apply confining pressure to the specimen. A smooth plastic coated paper is placed in between the soil-platen interfaces to facilitate easy lateral displacement of the sample during testing. The rubber membrane is not rigidly fastened to the top and bottom platens by O-rings and thus there is a relative reduction in friction at the soil-platen interface.

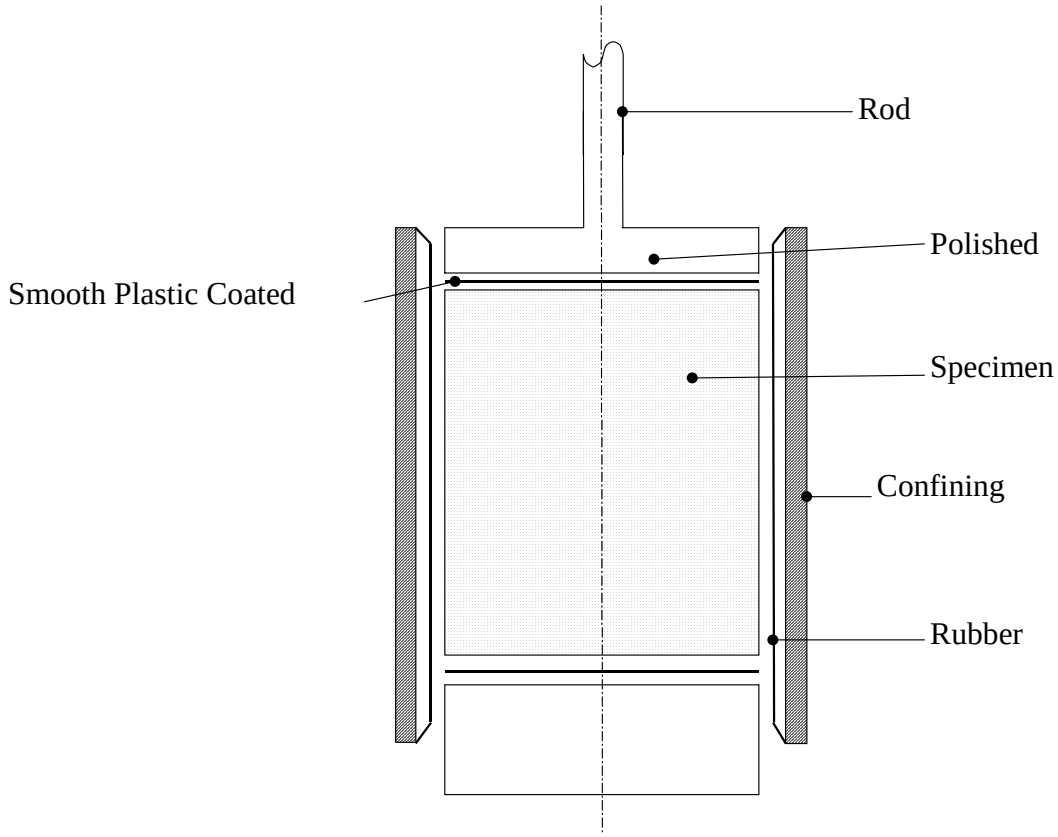

Figure 40. Rapid Triaxial Tester.

Stress Distribution in a Cylindrical Sample

Balla (1960) analytically solved for stresses and strains in a cylindrical specimen with any height to diameter ratio and subjected to axial and radial loads. Balla also studied the influence of end restraint at different degrees of roughness. The modern computer and finite element method have now made it easier to numerically study the distribution of stresses within a triaxial specimen with different sizes.

A finite element method was used to numerically determine the distribution of stresses in a cylindrical sample subjected to unconfined compression (Figure 41). The distribution of stresses was determined for fixed and frictionless platens.

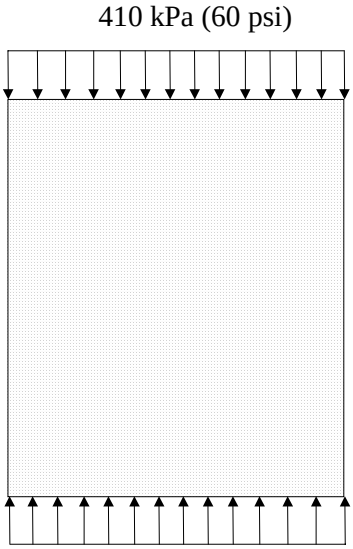

Figure 41. Unconfined Compression.

Figure 42 and 43 are axisymmetric finite element meshes for a frictionless platen and a fully fixed platen, respectively. The frictionless mesh represents a sample with fully lubricated end platens and the fixed mesh represents a sample with maximum friction. The platen conditions of a traditional triaxial sample with regular end caps is assumed to be very similar to the fixed mesh and the RaTT cell is assumed to be more similar to the frictionless mesh. The material was assumed to be linear isotropic.

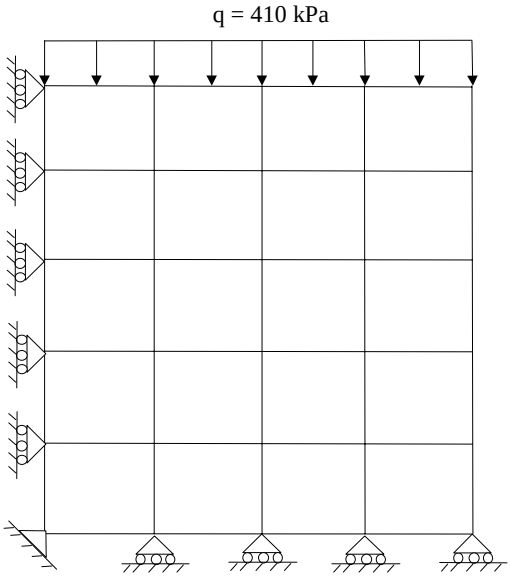

Figure 42. Axisymmetric Mesh for a Frictionless Platen.

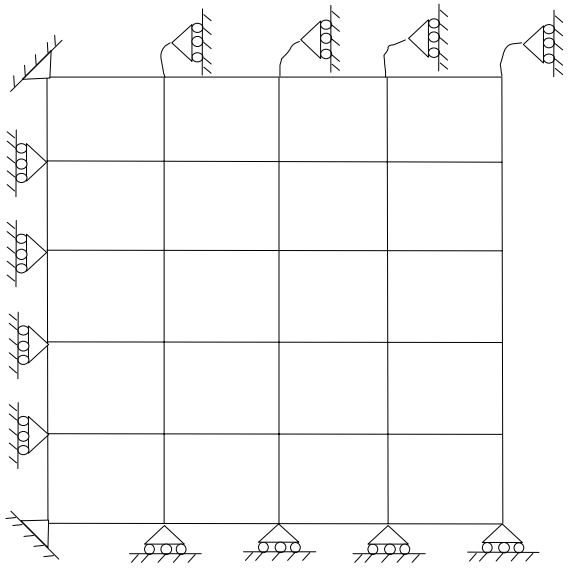

Figure 43. Axisymmetric Mesh for a Fixed Platen.

Figures 44 and 45 are the distribution of vertical and shear stresses, respectively, obtained from the finite element analysis on a 1:1 sample height to diameter. Figures 46 and 47 are plots of vertical and shear stresses, respectively, obtained for a 2:1 sample diameter to height ratio. No shear stresses develop in a sample with frictionless platens

and the distribution of vertical stresses is uniform within the sample. The frictionless platen allows the sample setup to fulfill the main purpose of producing principal stresses and measuring strains in a sample. High shear stresses develop at the ends and diminish at the mid-height of a sample with regular end platens. The developments of high shear stresses at the ends of a regular platen induce a non-uniform distribution of vertical stresses within the sample. The vertical stresses at the ends increase and converge to a uniform value in the middle of the specimen. For a frictionless platen, the distribution of shear and vertical stresses remain the same when the sample dimension is increased from 1:1 to 2:1 height to diameter ratio. When the sample size is changed from 1:1 to 2:1, the mid-portion of the sample, where shear stresses diminish for a uniform distribution of vertical stresses, increases (Figures 44 to 47).

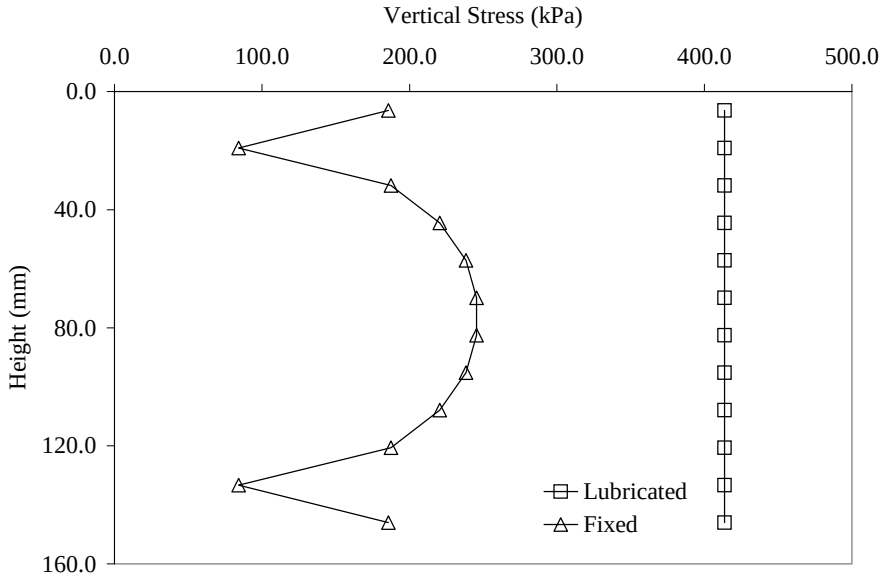

Figure 44. Distribution of Vertical Stresses in 1:1 Sample Size.

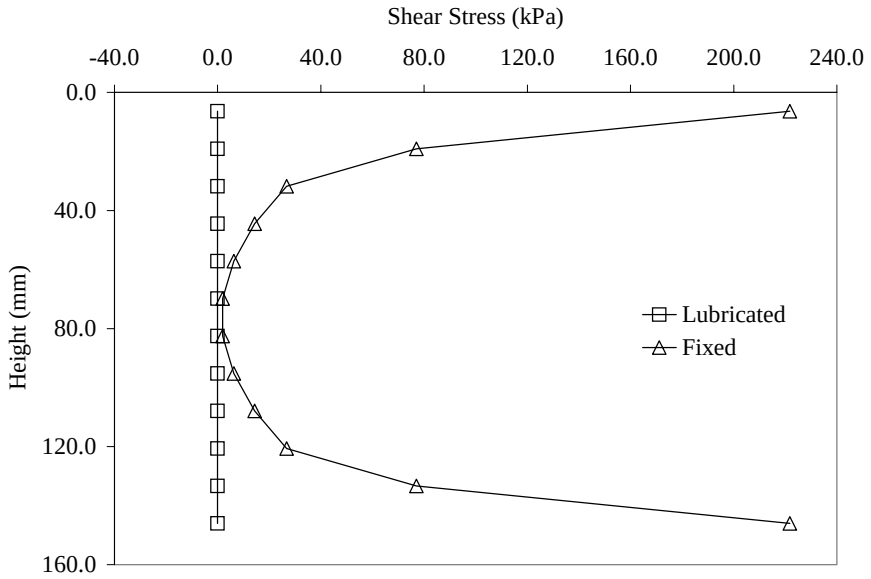

Figure 45. Distribution of Shear Stresses in a 1:1 Sample Size.

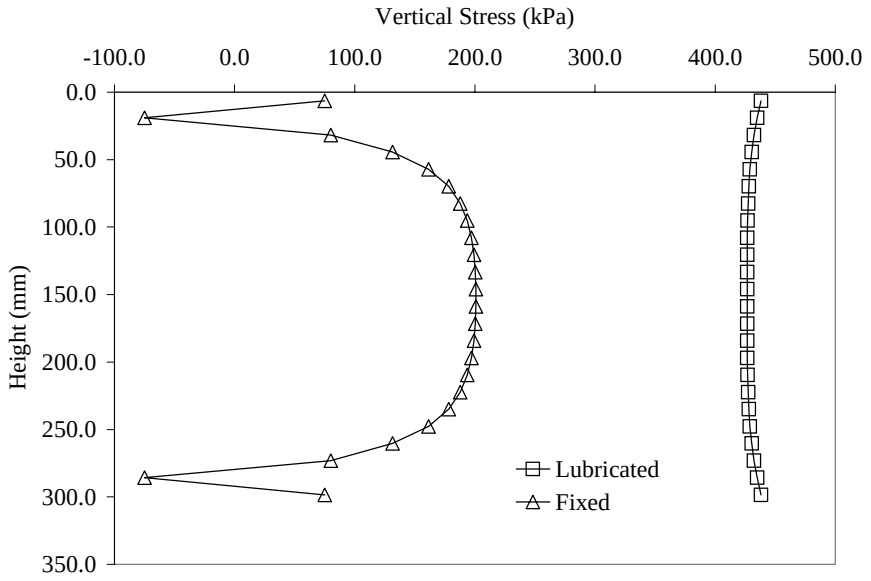

Figure 46. Distribution of Vertical Stresses in a 2:1 Sample Size.

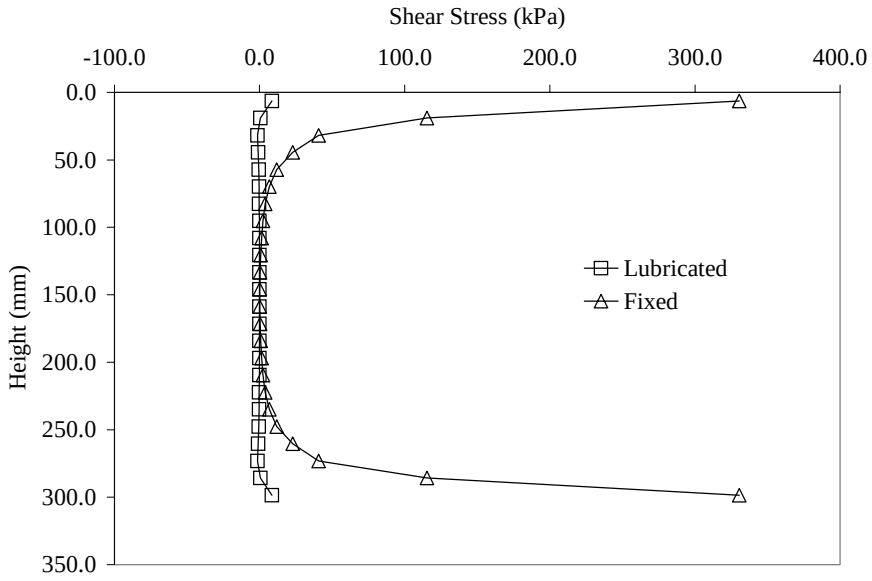

Figure 47. Distribution of Shear Stresses in a 2:1 Sample Size.

Figures 44 through 47 suggest that the presence of friction at the end platens of a triaxial specimen induce non-uniform stresses within the sample. However, if a uniform stress distribution can be induced in the middle portion of the sample, the end restraint effect can be acceptable. Increasing the height to diameter ratio does not eliminate the non-uniform stress distribution but rather increases the portion where shear stresses are acceptably diminished. Lubricating the end platens eliminates non-uniform stress distribution and development of shear stresses.

Laboratory Testing

The effect of reducing the sample height to diameter from 2 to 1 in the repeated load triaxial test was investigated. Since stresses and strains induced in a sample are well below the failure stress, it is expected that reducing the sample size would not have significant effects on the resilient modulus. Although the RaTT cell does not guarantee absolute frictionless platens, the level of friction is relatively lower than the traditional triaxial cell with regular platens.

A base material was tested in general accordance with AASHTO T-294. Two sample sizes were prepared at the same moisture content in accordance with AASHTO T-180. The sample sizes were 300-mm high by 150-mm diameter (2:1) and 150-mm high

by 150-mm diameter (1:1). The samples were tested using the standard triaxial cell with regular end platens. The results of the resilient modulus obtained are tabulated in Tables 19 and 20 for 1:1 and 2:1 sample size respectively. Testing was performed in conjunction with the University of Wisconsin and University of Illinois.

Figure 48 shows plots of resilient modulus versus bulk stress for both sample sizes. This suggests that even in a standard triaxial cell with regular end platens where friction is assumed to exist, resilient modulus values were not affected by the sample size. This observation may be due to the fact that the stresses applied in the resilient triaxial test are well below the failure stress.

As a result, the maximum particle size of a base material must be the limiting factor in choosing sample size rather than the distribution of stresses. Instead of the traditional 2:1 sample height to diameter ratio, the more stable and practical size of 1:1 can be used in repeated load triaxial test. Throughout this study, 1:1 sample height to diameter ratio samples were prepared for testing.

Table 19. Resilient Modulus for 1:1 Sample Size.

Confining Stress (kPa)	Deviator Stress (kPa)	Bulk Stress (kPa)	Modulus (MPa)
20.7	22.3	84.4	185.2
34.5	69.5	172.9	256.0
68.9	208.5	415.4	291.7
103.4	103.1	413.3	261.1
137.9	138.7	552.4	370.2
137.9	283.5	697.1	444.4

Table 20. Resilient Modulus for 2:1 Sample Size.

Confining Stress (kPa)	Deviator Stress (kPa)	Bulk Stress (kPa)	Modulus (MPa)
20.7	22.0	84.0	251.6
34.5	72.8	176.2	215.7
68.9	207.6	414.5	321.1
103.4	103.2	413.5	289.4
137.9	138.2	551.9	395.7
137.9	274.7	688.4	420.4

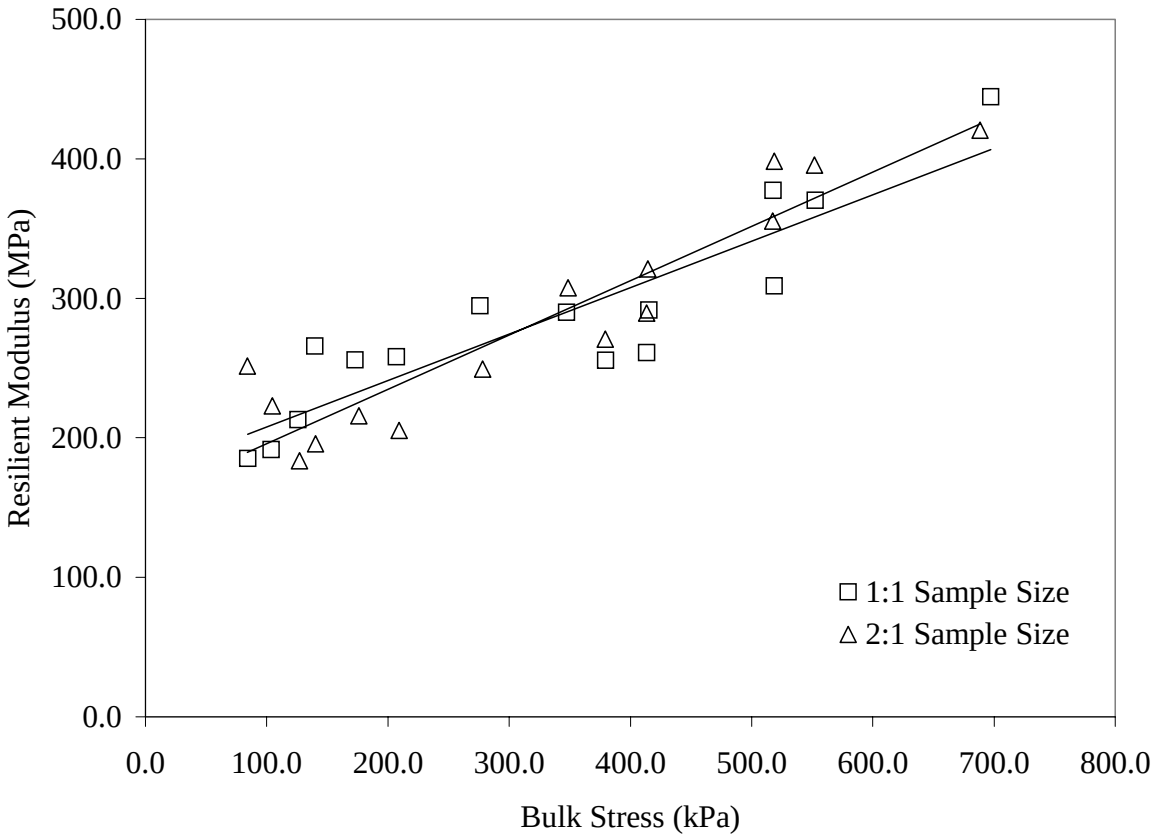

Figure 48. Resilient Modulus versus Bulk Stress.

SPECIAL STUDIES: COMPACTION

Background

The mechanical properties of unbound granular layers are improved through compaction. Compaction forces the individual particles of unbound granular materials together and enhances increased particle-to-particle contact. Increasing densities through compaction is highly beneficial for the load carrying capacity of unbound granular layers. Allen (1973) and Marek *et al*., (1974) demonstrated that the decrease in permanent deformation for small increases in density through compaction is very significant. An apparent anisotropy is induced in an unbound granular layer in a pavement system during construction, making the granular layer stiffer in the vertical direction than in the horizontal direction even before traffic loads impose further anisotropy. A laboratory testing protocol was developed in which the anisotropic properties of an unbound granular material are determined using a triaxial set up. The details of the testing protocol are discussed earlier.

The laboratory compaction characteristics of unbound granular materials are important to the behavior and performance of a flexible pavement. Three different compaction methods; impact, vibratory and gyratory shear; were investigated in this study to determine their effects on the anisotropic properties of unbound granular materials. For each compaction method, two different compactive efforts were investigated.

Compaction Methods

There are five major compaction methods, which are commonly used to fabricate unbound aggregate specimens for laboratory testing. These methods are briefly described below.

Impact Compaction

The first scientific approach to determine laboratory compaction characteristics of soils is credited to R.R Proctor (1933). His procedure was slightly revised and adopted as a standard by the American Association of State Highway Officials in 1939 (AASHTO

Designation: T-99). It was later modified to allow higher compaction effort (AASHTO Designation: T-180). In this method, the sample is compacted in a rigid mold by dropping a hammer of known weight from a specified height. One of the main disadvantages of the impact compaction method is that aggregate orientation and distribution are dissimilar to that achieved in field compaction. As a result, it is difficult to achieve reproducible results, and there are some disparities in the stress-strain distributions predicted in the pavement structure based on the laboratory-derived resilient moduli. The primary variables that can be controlled in impact compaction are the weight of the hammer, the height of hammer drop, and the number of blows per layers. If any of these are increased to achieve high densities at low moisture contents, much of the additional compactive energy is spent in degrading the material rather than in compacting it.

Static Compaction

As the name suggests, samples are compacted in a rigid mold by applying static compressive stresses to plungers on one or both ends of a specimen. There is no standard method for applying this method to unbound granular materials. The compaction characteristics and particle orientation achieved by this method do not reproduce field compaction. Also, friction between the particles and the mold walls tend to produce significant density gradients within the sample.

Kneading Compaction

Conventional field compaction equipment such as the sheepsfoot and rubber-tired rollers apply loads with little or no impact, but they produce some kneading action. The California Highway Department developed a mechanical kneading laboratory compactor in 1937. A revised design of this compactor was adopted in a standard procedure (AASHO T-173). This method of compaction is not widely used by highway agencies. Although particle distribution and orientation closely matches field compaction, some hand finishing is required to prepare samples for testing in the laboratory.

Vibratory Compaction

In this method, the material is confined in a rigid mold, and a surcharge weight is placed on the surface of the material. Either the wall of the mold is tapped or the entire

mold is placed on a vibrating mechanism. Vibratory compaction has been successfully applied to the compaction of dry cohesionless soils, primarily sands. The advent of hand held vibratory equipment has increased the use of vibratory compaction methods for preparing unbound granular material specimens. Here, layers of material, usually 50-mm (2-in layers), are compacted to predetermined densities using hand held vibrators in a rigid mold. Material degradation is prevented.

Shear Gyratory Compaction

In the early 1940's the Texas Highway Department began compacting specimens by gyratory shear action. In this method a known stress is applied to a sample in a rigid mold after the mold has been inclined at an angle. The mold is gyrated with the applied stress still on the sample until the desired density is achieved. Application of gyratory compaction to asphalt concrete mixtures was one of the major contributions of the Strategic Highway Research Program (SHRP). This method is also widely used in Texas to compact unbound granular materials and bituminous-stabilized bases. The Texas Department of Transportation (TXDOT) has a standard procedure (Test Method Tex-126-E) for compacting unbound granular and bituminous base materials. The applied stress and time or number of gyrations can be varied to achieve a desired density at specific moisture contents. Researchers at Texas Transportation Institute (Moore and Milberger 1968) investigated the issue of density gradient, and it was concluded that if the sample height to diameter ratio is kept below about 1.4, a uniformly compacted specimen is generally achieved.

Materials, Specimen Preparation, and Testing

Two well graded base course materials, crushed limestone and siliceous gravel, were used for this study. The materials were compacted using impact, vibratory, and gyratory compaction methods. For each compaction method, a low and a high compaction effort, was used. 150-mm diameters by 150-mm height samples were prepared for all combinations of compaction method and effort.

Samples prepared with the impact compaction method were compacted in general accordance with AASHTO T-180, using a 4.54-kg hammer and a 457-mm drop. The

samples were prepared by applying either 50 blows per 50-mm thick layers or 25 blows per 50-mm thick layers for high and low compaction efforts, respectively.

For the vibratory compaction method, the higher compaction effort samples were prepared in three lifts (50-mm thick per lift). A hand vibrator was used to compact each lift until AASHTO T-180 density was achieved. The lower compaction effort samples were prepared in two lifts (75-mm thick) until 90% of the AASHTO T-180 density was achieved.

Samples prepared with a high compaction effort using the gyratory compaction method were fabricated by applying 275-kPa pressure on samples inclined at 3° and gyrated for 60 seconds. Lower compaction effort samples were prepared by applying 137-kPa pressure on samples inclined at 3° and gyrated for 45 seconds. The gyratory compactor was set to a constant speed of 30 gyrations per minute. Three lifts of the specimen were compacted statically and then the entire specimens were compacted dynamically. After compaction, the top of the samples was leveled with the same stress as applied during gyrations.

The specimens prepared with the impact and gyratory compaction methods were tested with the Texas Transportation Institute (TTI) Rapid Triaxial Tester (RaTT) using a recently developed testing protocol in which the anisotropic properties of an unbound granular material are backcalculated with a system identification routine (Adu-Osei et. al., 2000). The specimens prepared with the vibratory compaction method were tested with the University of Illinois FastCell (UIFC). The differences between these two triaxial cells are the mode of application of confining pressure and the range of linear variable differential transformers (LVDTs). The RaTT uses air for confinement and the UIFC uses oil. Also, the LVDTs on the UIFC have a wider deflection range and need to be adjusted for small and large deflections.

Results of Compaction Study

The moduli are assumed to obey the non-linear universal (Uzan, 1985; 1992) material model (Equations 53, 54, 55).

The k-values, model parameters, were determined from regression analysis for each combination of material type, compaction method and compaction effort. The

molding moisture contents and the resulting dry densities for each combination are shown in Table 21. The k-values are shown in Tables 22 and 23 for siliceous gravel and crushed limestone, respectively. The recorded moduli values at low, medium and high stress states are tabulated in Tables 24 and 25 for siliceous gravel and crushed limestone, respectively.

In this study a low stress state is equivalent to a confining stress of 40 kPa and a deviator stress of 30 kPa. A medium stress state is equivalent to a confining stress of 100 kPa and a deviator stress of 70 kPa. A high stress state is equivalent to a confining stress of 120 kPa and a deviator stress of 130 kPa.

Table 21. Molding Moisture Content and Dry Density.

	Crushed Limestone					
	Impact		Vibratory		Gyratory	
	Low Effort	High Effort	Low Effort	High Effort	Low Effort	High Effort
Moisture Content, %	6.0	6.0	6.0	6.0	5.0	5.0
Dry Density, kg/m^3	2150	2160	1944	2160	2180	2200
	Siliceous Gravel					
	Impact		Vibratory		Gyratory	
	Low Effort	High Effort	Low Effort	High Effort	Low Effort	High Effort
Moisture Content, %	5.0	5.0	5.0	5.0	4.0	4.0
Dry Density, kg/m^3	2300	2350	2115	2350	2350	2360

Table 22. Model Parameters for Siliceous Gravel.

	Impact		Vibratory		Gyratory	
	Low Effort	High Effort	Low Effort	High Effort	Low Effort	High Effort
k_1	2553	3736	3910	2517	4726	4057
k_2	0.327	0.220	0.058	0.378	0.218	0.269
k_3	0.071	0.103	0.148	0.080	0.139	0.061
k_4	1195	838	465	771	358	992
k_5	0.637	0.797	0.745	0.652	1.242	0.556
k_6	-0.089	-0.083	-0.036	-0.031	-0.057	-0.030
k_7	696	695	621	559	500	754
k_8	0.550	0.593	0.449	0.638	0.799	0.522
k_9	-0.012	-0.004	0.060	0.019	0.019	-0.005
ν_{xy}	0.18	0.17	0.06	0.14	0.16	0.17
ν_{xx}	0.36	0.35	0.11	0.32	0.31	0.40

Table 23. Model Parameters for Crushed Limestone.

	Impact		Vibratory		Gyratory	
	Low Effort	High Effort	Low Effort	High Effort	Low Effort	High Effort
k_1	3112	4663	2315	2109	4533	5085
k_2	0.312	0.344	0.452	0.604	0.257	0.241
k_3	0.124	0.084	0.062	0.057	0.134	0.099
k_4	441	639	271	622	267	781
k_5	1.053	1.068	0.925	0.899	1.254	0.960
k_6	0.019	-0.063	-0.058	-0.028	-0.025	-0.044
k_7	447	635	319	676	366	691
k_8	0.785	0.813	0.793	0.666	0.895	0.736
k_9	0.042	-0.011	-0.007	0.046	0.026	-0.003
ν_{xy}	0.15	0.20	0.05	0.12	0.19	0.18
ν_{xx}	0.30	0.42	0.09	0.27	0.41	0.40

Table 24. Resilient Moduli for Siliceous Gravel.

Stress State	Vertical Resilient Modulus, MPa					
	Impact		Vibratory		Gyratory	
	Low Effort	High Effort	Low Effort	High Effort	Low Effort	High Effort
Low	192.0	208.0	148.0	169.0	232.0	305.0
Medium	305.0	349.0	258.0	321.0	411.0	464.0
High	394.0	449.0	315.0	415.0	531.0	581.0
	Horizontal Resilient Modulus, MPa					
Low	277.0	201.0	91.1	152.0	111.0	152.0
Medium	376.0	306.0	160.0	200.0	232.0	214.0
High	395.0	345.0	142.0	225.0	263.0	258.0
	Resilient Shear Modulus, MPa					
Low	105.0	99.3	55.0	71.8	78.3	101.0
Medium	152.0	157.0	99.8	134.0	145.0	159.0
High	173.0	183.0	101.0	146.0	167.0	178.0

Table 25. Resilient Moduli for Crushed Limestone.

Stress State	Vertical Resilient Modulus, MPa					
	Impact		Vibratory		Gyratory	
	Low Effort	High Effort	Low Effort	High Effort	Low Effort	High Effort
Low	161.0	326.0	174.0	174.0	231.0	323.0
Medium	298.0	550.0	349.0	391.0	428.0	503.0
High	411.0	707.0	421.0	514.0	588.0	642.0
	Horizontal Resilient Modulus, MPa					
Low	64.9	165.0	70.9	120.0	104.0	178.0
Medium	156.0	312.0	121.0	247.0	232.0	310.0
High	238.0	391.0	127.0	250.0	271.0	387.0
	Resilient Shear Modulus, MPa					
Low	54.3	111.0	49.6	71.2	71.5	111.0
Medium	112.0	198.0	99.8	147.0	145.0	189.0
High	145.0	234.0	108.0	178.0	180.0	222.0

It is observed from Table 24 that compaction method and effort generally affect the dry unit weight of a compacted sample. These increases in density obtained going from a lower compactive effort to a higher one resulted in higher values of resilient moduli. Samples prepared with the vibratory compaction method at low compaction effort recorded the lowest values in moduli. The highest moduli values were recorded from samples prepared with gyratory compaction method at high compaction effort.

The materials were generally stiffer in the vertical direction. However, the horizontal resilient modulus values were slightly higher at each stress state than the vertical resilient modulus for gravel samples compacted with the impact compaction method at low effort (25 blows per layer). When the compaction effort was increased to 50 blows per layer the horizontal resilient moduli were lower, but the average value was 80% of the vertical modulus as compared to 46%-60% in the case of the other compaction methods and efforts. Thus, the induced anisotropy by the impact compaction method was not significant. Samples compacted with the vibratory compaction method recorded unusually low Poisson's ratios. This may be due to the differences in LVDT range between RaTT and UIFC as mentioned earlier.

The non-linear anisotropic properties (k-values) are useful in determining pavement response with a finite element code. The anisotropic model generally reduces and/or reverses the horizontal tensile stresses predicted in the base course with isotropic elastic properties. Horizontal tensile stresses predicted within a base course suggests that negative values of bulk stress exist within the base layer. This anomaly will predict unrealistic resilient moduli within the entire base course and cross-anisotropic model can effectively correct it (Tutumluer, 1995).

REFERENCES

1. AASHTO Guide for Design Pavement Structures, (1993), American Association of State and Highway Officials, Washington DC.
2. Adu-Osei, A., Lytton, R. L. and Little, D. N., (2000), System Identification Method for Determining the Anisotropic Resilient Properties of Unbound Aggregates. Unbound Aggregates in Roads.
3. Allen, J. J., (1973), The Effects of Non-Constant Lateral Pressures on Resilient Response of Granular Materials. Ph.D., Dissertation. University of Illinois at Urbana-Champaign, IL.
4. Alvin, R. G., and Ulery, H. H., (1962), Tabulated Values for Determining the Complete Pattern of Stresses, Strains and Deflections Beneath A Uniform Circular Load on a Homogeneous Half Space, Bulletin 342, Highway Research Board, pp. 1-13.
5. Amadei, B., (1983), Rock Anisotropy and the Theory of Stress Measurements. Lecture Notes in Engineering 2, Springer-Verlag.
6. Barksdale, Richard D. and Todres, H. A., (1983), A Study of Factors Affecting Crushed Stone Base Performance, Final Report Georgia DOT HPR 7603, Atlanta, Georgia.
7. Barksdale, R. D., (1971), Compressive Pulse Times in Flexible Pavements for Use in Dynamic Testing, Highway Research Record No. 345, Highway Research Board, National Research Council, Washington, DC.
8. Barksdale, R. D., and Alba, J. L., (1993), Laboratory Determination of Resilient Modulus for Flexible Pavements Design, Interim Report No. 2, NCHRP, Transportation Research Board, National Research Council, Washington, DC.
9. Barksdale, R. D., Brown, S. F. and Chan, F., (1989), Potential Benefits of Geosynthetics in Flexible Pavements, NCHRP Report 315, Transportation Research Council, Washington, DC.
10. Bishop, A. W., and Green, G. E., (1965), The Influence of End Restraint on the Compression Strength of a Cohesionless Soil, Geotechnique, Vol. 15, No.3, pp.243-265.

11. Boussinesq, J., (1885), Application des Potentiels a L'etude de L'equilibre et du Mouvement des Solids Elastiques, Gauthier-Villars, Paris.
12. Boyce, J. R., (1976), The Behavior of a Granular Material under Repeated Load. Ph.D. Thesis, University of Nottingham, Department of Civil Engineering, U.K.
13. Boyce, J. R., Brown, S. F. and Pell, P. S., (1976), The resilient Behaviour of a Granular Material Under Repeated Loading, Proceedings, Australia Road Research Board, 28, pp. 8-19.
14. Brown, S. F., O'Reilly, M. P., and Pappin, J. W., (1989), A Repeated Load Triaxial Apparatus for granular Materials, Unbound Aggregates in Roads, London, Butterworth, pp. 143-158.
15. Burmister, D. M., (1943), The Theory of Stresses and Displacements in Layered Systems and Applications to the Design of Airport Runways, Proceedings, Highway Research Board, Vol. 23, pp. 126-144.
16. Burmister, D. M., (1945), The General Theory of Stresses and Displacements in Layered Soil Systems, Journal of Applied Physics, Vol. 16, pp. 84-94, 126-127, 296-302.
17. Chan, F. W. K., (1990), Permanent Deformation Resistance of Granular Layers in Pavements. Ph.D. Thesis, University of Nottingham, UK.
18. Clough, R. W., (1960), The Finite Element Method in Plane Stress Analysis, Proceedings, 2nd Conference on Electronic Computation, ASCE.
19. Crockford, W. W., Bendana, L. J., Yang, W. S., Rhee, S. K., and Senadheera, S. P., (1990), Modeling Stress and Strain States in Pavement Structures Incorporation Thick Granular Layers. Final Report, Texas Transportation Institute, College Station, Texas.
20. De Jong, D. L., Peatz, M., G. F. and Korswagen, A. R., (1973), Computer Program Bisar, Layered Systems Under Normal and Tangential Loads, Konin Klijke Shell-Laboratorium, Amsterdam, External Report AMSR.0006.73.
21. Doddihal, S. R., and Pandey, B. B., (1984), Stresses in Full Depth Granular Pavements, Transportation Research Record No. 954, Transportation Research Board, National Research Council, Washington, DC, pp. 94-100.

22. Duncan, J. M. and Dunlop, P., (1968), The Significance of Cap and Base Restraint, Journal of the Soil Mechanics and Foundations Division, ASCE, Vol. 94, SM1, pp. 271-290.
23. Duncan, J. M., Monismith C. L., and Wilson, E. L., (1968), Finite Element Analysis of Pavements, Highway Research Record NO. 228, Highway Research Board, Washington, DC, pp. 18-33.
24. Foster, C. R. and Alvin, R. G., (1958), Development of Multiple-Wheel CBR Design Criteria, Journal of the Soil Mechanics and Foundation Division, ASCE, Vol. 84, No. SM2, May, pp. 1647-1 to 1647-12.
25. Fredlund, D. G. and Xing, A., (1994), Equations for the Soil-Water Characteristic Curve, Canadian Geotechnical Journal, 31, 521-532.
26. Hicks, R. G. and Monismith, C. L., (1971), Factors Influencing the Resilient Properties of Granular Materials, Transportation Research Record 345, Transportation Research Board, National Research Council, Washington, DC, pp. 15-31.
27. Hicks, R.G., (1970), Factors Influencing the Resilient Properties of Granular Materials, Ph.D. Dissertation, University of California, Berkeley, CA.
28. Hwang, D. and Witczak, M. W., (1979), Program DAMA (Chevron) User's Manual, Department of Civil Engineering, University of Maryland, MD.
29. Industrial Process Control, (1998), Universal Testing Machine Manual, Australia.
30. Kopperman, S., Tiller, G. and Tseng, M., (1986), ELSYM5, Interactive Microcomputer Version, User's Manual, Report No. FHWA-TS-87-206, Federal Highway Administration, Washington, DC.
31. Lee, K. L. and Frank J. Vernese, (1978), End Restraint Effects on Cyclic Triaxial Strength of Sand, Journal of the Geotechnical Division, ASCE, GT6, pp. 705-719.
32. Liu, M., (1993), Numerical Prediction of Pavement Distress with Geotechnical Constitutive Laws. Ph.D. Dissertation, Texas A&M University, College Station, Texas.
33. Lytton, R. L., (1995), Foundations and Pavements on Unsaturated Soils. 1st International Conference on Unsaturated Soils, Paris.

34. Lytton, R. L., Uzan, J., Fernando, E., Roque, R., Hiltunen, D., and Stoffels, S. M., (1993), Development and Validation of Performance Prediction Models and Specifications for Asphalt Binders and Paving Mixes, Strategic Highway Research Program, SHRP A-357, National Research Council, Washington, DC.
35. Marek, C. R., and Jones, T. R., Jr., (1974), Compaction-An Essential Ingredient for Good Base Performance, Proceedings, Conference on Utilization of Graded Aggregate Base Materials in Flexible Pavements, Oak Brook, IL.
36. Milberger, L. J. and Dunlop, W. A., (1966), A Gyratory Compactor for Molding Large Diameter Triaxial Specimens of Granular Materials, Texas Transportation Institute Report No. 99-2.
37. Moore, W. M. and Milberger, L. J., (1968), Evaluation of the TTI Gyratory Compactor, Texas Transportation Institute Report No. 99-3.
38. National Association of Australian State Road Authorities, (1987), A Guide to the Structural Design of Road Pavements, Australia.
39. Nazarian, S., Pezo, R., Melarkode, S., and Picornell, M., (1996), Testing Methodology for Resilient Modulus of Base Materials, Transportation Research Record 1547, TRB, National Research Council, Washington DC.
40. Owen, D. R. J. and Hinton, E., (1980), Finite Elements in Plasticity: Theory and Practice, Pineridge Press, Swansea, U.K.
41. Pappin, J. W., (1979), Characteristics of a Granular Material for Pavement Analysis. Ph.D. Thesis, University of Nottingham, Department of Civil Engineering, U.K.
42. Park, S. W., (2000), Evaluation of Accelerated Rut Development in Unbound Pavement Foundations and Load Limits on Load-Zoned Pavements, Ph.D. Dissertation, Texas A&M University, College Station, Texas.
43. Pickering, D. J., (1970), Anisotropic Elastic Parameters for Soil, Geotechnique 20, No. 3, pp 271-276.
44. Porter, D. W., (1999), Technical Basis of the 1992 Austroads pavement Design Guide (Flexible Pavements), ARRB Transport Research No. RC7095-2, Australia.
45. Rowe, P. W. and Barden, L., (1964), Importance of Free Ends in Triaxial Testing, Journal of the Soil Mechanics and Foundations Division, ASCE, SM1, pp. 1-27.

46. Seed, H. B., Chan, C. K., and Monismith, C. L., (1955), Effects of Repeated Loading on the Strength and Deformation of Compacted Clay, Proceedings, Highway Research Board, 34, Washington, DC, pp. 541-558.
47. Stewart, E. H., Selig, E. T., and Norman-Gregory, G. H., (1985), Failure Criteria and Lateral Stresses in Track Foundations, Transportation Research Record No. 1022, Transportation Research Board, National Research Council, Washington, DC, pp. 59-64.
48. Sweere, G. T. H., (1990), Unbound Granular Bases for Roads. Ph.D. Dissertation, Delft University of Technology, The Netherlands.
49. Taylor, D. W., (1941), 7th Progress Report on Shear Strength to U.S. Engineers, Massachusetts Institute of Technology.
50. Texas Department of Transportation, (1995), Molding, Testing, and Evaluation of Bituminous Black Base Materials, TxDOT Manual of Testing Procedures, Test Method Tex-126-E.
51. Turner, M. J., Clough, R. W., Martin, H. C., and Topp, L. J., (1956), Stiffness and Deflection Analysis of Complex Structures, Journal of Aeronautical Sciences, Vol. 23, No. 9, pp. 805-823.
52. Tutumluer, E., (1995), Predicting Behavior of Flexible Pavements with Granular Bases. Ph.D. Thesis, Georgia Institute of Technology, GA.
53. Tutumluer, E., (1998), Anisotropic Behavior of Unbound Aggregate Bases. Proceedings, 6th Annual Symposium, International Center for Aggregate Research, St. Louis, MO.
54. Tutumluer, E., and Thompson, M. R., (1997), Anisotropic Modeling of Granular Bases in Flexible Pavements, Transportation Research Record, No. 1577. Transportation Research Board, National Research Council, Washington, DC.
55. Uzan J., (1992), Resilient Characterization of Pavement Materials, International Journal for Numerical and Analytical Methods in Geomechanics, Vol.16.
56. Uzan, J., (1985), Characterization of Granular Material, Transportation Research Record 1022, TRB, National Research Council, Washington DC, pp. 52-59.

57. Wang, F. and Lytton R. L., (1993), System Identification Method for Backcalculating Pavement Layer Properties, Transportation Research Record 1384, TRB, National Research Council, Washington, DC, pp. 1-7.
58. Wardle, L. J, (1986), Computer Program CIRCLY, User's Manual. MINCAD Systems Pty Ltd, Richmond, Australia.
59. Warren, H., and Dieckman, W. L., (1963), Numerical Computation of Stresses and Strains in a Multiple-Layer Asphalt Pavement System, International Report, Chevron Research Corporation, Richmond, CA.
60. Witczak, M. W. and Uzan, J., (1988), The Universal Airport Pavement Design System Report I of V: Granular Material Characterization, University of Maryland, Department of Civil Engineering, MD.
61. Zienkiewicz, O. C., Cheung, Y. K., and Stagg, K. G., (1966), Particular Reference to Problems of Rock Mechanics, Journal of Strain Analysis, Vol. 1, No.2, pp. 172-182.
62. Zienkiewicz, O. C., Valliappan, S., and King, I. P., (1968), Stress Analysis of Rock as a No Tension Material, Geotechnique, Vol. 18, pp.56-66.

APPENDIX A

TABLES OF AVERAGE RESILIENT STRAIN

Table 26. Average Resilient Strains for Well Graded Texas Limestone at Dry of Optimum.

Stress State		Triaxial Compression		Triaxial Shear		Triaxial Extension	
Stress (kPa)		Strain (με)		Strain (με)		Strain (με)	
Axial	Radial	Axial	Radial	Axial	Radial	Axial	Radial
40.0	25.0	29.6	-10.9	103.7	-84.7	-71.3	46.6
50.0	25.0	50.2	-23.7	79.5	-72.3	-98.8	69.0
70.0	40.0	39.1	-14.8	53.8	-38.3	-93.6	68.8
130.0	60.0	49.0	-21.2	74.1	-65.4	-51.1	43.5
150.0	70.0	43.8	-17.3	63.4	-51.6	-41.7	35.8
170.0	100.0	41.6	-15.2	56.1	-35.4	-87.1	61.7
220.0	120.0	53.3	-18.0	74.1	-49.5	-67.3	48.8
250.0	140.0	49.9	-14.7	64.4	-40.0	-57.5	39.5
250.0	120.0	47.6	-15.8	65.8	-46.9	-59.8	45.4
250.0	105.0	47.2	-16.1	66.9	-54.2	-53.8	42.2

Table 27. Average Resilient Strains for Well Graded Texas Limestone at Wet of Optimum.

Stress State		Triaxial Compression		Triaxial Shear		Triaxial Extension	
Stress (Kpa)		Strain (με)		Strain (με)		Strain (με)	
Axial	Radial	Axial	Radial	Axial	Radial	Axial	Radial
40.0	25.0	30.8	-14.4	105.3	-85.7	-81.1	56.3
50.0	25.0	53.7	-26.4	81.4	-72.5	-105.5	76.8
70.0	40.0	41.2	-19.4	58.8	-43.6	-107.7	81.5
130.0	60.0	53.3	-25.3	77.4	-69.7	-54.1	49.1
150.0	70.0	46.7	-20.0	65.4	-54.9	-45.7	39.1
170.0	100.0	43.6	-18.2	62.1	-40.8	-97.3	72.0
220.0	120.0	56.8	-20.3	77.4	-56.6	-74.1	56.7
250.0	140.0	51.4	-17.4	68.5	-46.8	-62.4	47.5
250.0	120.0	51.1	-19.3	72.3	-58.6	-67.4	58.8
250.0	105.0	50.7	-20.0	72.6	-63.5	-58.4	50.6

Table 28. Average Resilient Strains for Fine Graded Texas Limestone at Optimum.

Stress State		Triaxial Compression		Triaxial Shear		Triaxial Extension	
Stress (kPa)		Strain (με)		Strain (με)		Strain (με)	
Axial	Radial	Axial	Radial	Axial	Radial	Axial	Radial
40.0	25.0	36.7	-24.6	137.7	-163.3	-123.2	119.6
50.0	25.0	57.1	-36.9	93.1	-111.4	-133.6	126.0
70.0	40.0	44.1	-24.3	67.6	-65.5	-150.6	143.1
130.0	60.0	54.1	-30.6	88.4	-103.0	-64.1	70.3
150.0	70.0	48.0	-24.2	75.2	-79.7	-53.4	55.8
170.0	100.0	45.6	-21.2	66.5	-54.6	-120.1	104.7
220.0	120.0	57.3	-25.6	85.1	-75.4	-83.8	75.7
250.0	140.0	53.3	-20.6	74.5	-59.7	-70.5	59.7
250.0	120.0	50.6	-22.4	75.6	-74.0	-73.3	73.6
250.0	105.0	48.8	-23.1	74.8	-84.0	-63.2	65.1

Table 29. Average Resilient Strains for Fine Graded Texas Limestone at Dry of Optimum.

Stress State		Triaxial Compression		Triaxial Shear		Triaxial Extension	
Stress (kPa)		Strain (με)		Strain (με)		Strain (με)	
Axial	Radial	Axial	Radial	Axial	Radial	Axial	Radial
40.0	25.0	29.5	-11.9	107.4	-82.9	-68.8	46.7
50.0	25.0	53.1	-24.1	74.0	-62.9	-83.0	56.9
70.0	40.0	39.3	-16.4	56.0	-39.3	-95.2	71.0
130.0	60.0	53.4	-22.9	78.6	-68.0	-52.4	44.0
150.0	70.0	46.3	-19.1	66.4	-54.3	-43.9	37.3
170.0	100.0	44.1	-16.5	58.1	-39.1	-93.3	67.8
220.0	120.0	55.4	-20.5	77.3	-53.3	-70.1	53.1
250.0	140.0	50.4	-16.8	67.1	-43.6	-59.0	43.3
250.0	120.0	50.0	-17.3	70.2	-50.3	-61.6	48.7
250.0	105.0	49.4	-18.3	71.1	-58.3	-57.1	45.1

Table 30. Average Resilient Strains for Fine Graded Texas Limestone at Wet of Optimum.

Stress State		Triaxial Compression		Triaxial Shear		Triaxial Extension	
Stress (kPa)		Strain (με)		Strain (με)		Strain (με)	
Axial	Radial	Axial	Radial	Axial	Radial	Axial	Radial
40.0	25.0	58.1	-53.6	226.4	-343.1	-479.5	545.4
50.0	25.0	69.9	-60.8	121.1	-190.1	-249.9	291.7
70.0	40.0	52.6	-37.3	88.4	-105.6	-279.0	295.6
130.0	60.0	58.0	-37.9	98.8	-137.3	-80.5	98.6
150.0	70.0	49.5	-29.4	81.8	-105.3	-64.1	77.2
170.0	100.0	50.3	-27.1	76.6	-73.3	-165.7	155.7
220.0	120.0	59.9	-30.8	94.8	-97.7	-105.8	103.3
250.0	140.0	55.2	-24.6	80.8	-75.5	-85.4	78.0
250.0	120.0	51.8	-25.2	79.0	-87.4	-82.9	89.8
250.0	105.0	47.5	-25.3	75.5	-94.6	-65.6	73.6

Table 31. Average Resilient Strains for Coarse Graded Texas Limestone at Optimum.

Stress State		Triaxial Compression		Triaxial Shear		Triaxial Extension	
Stress (kPa)		Strain (με)		Strain (με)		Strain (με)	
Axial	Radial	Axial	Radial	Axial	Radial	Axial	Radial
40.0	25.0	34.9	-11.0	113.5	-84.1	-82.9	51.5
50.0	25.0	59.2	-24.1	87.7	-73.7	-109.7	69.2
70.0	40.0	44.1	-16.0	61.6	-42.3	-102.1	72.1
130.0	60.0	55.4	-21.4	78.8	-68.8	-54.0	48.3
150.0	70.0	49.4	-18.1	68.6	-56.6	-47.3	41.3
170.0	100.0	47.3	-15.2	61.2	-40.1	-92.0	67.9
220.0	120.0	60.4	-18.6	76.6	-55.0	-58.2	44.6
250.0	140.0	53.8	-16.7	71.6	-46.5	-63.2	48.4
250.0	120.0	53.5	-16.8	71.2	-53.8	-63.6	54.9
250.0	105.0	52.7	-17.8	71.8	-60.1	-58.4	48.8

Table 32. Average Resilient Strains for Well Graded Texas Gravel at Optimum.

Stress State		Triaxial Compression		Triaxial Shear		Triaxial Extension	
Stress (kPa)		Strain (με)		Strain (με)		Strain (με)	
Axial	Radial	Axial	Radial	Axial	Radial	Axial	Radial
40.0	25.0	28.5	-7.3	86.6	-48.8	-44.5	29.4
50.0	25.0	51.4	-16.3	67.6	-43.8	-67.4	38.5
70.0	40.0	39.2	-14.5	51.7	-32.1	-73.1	57.5
130.0	60.0	53.5	-21.9	76.3	-62.9	-44.9	41.5
150.0	70.0	49.5	-16.8	65.9	-51.4	-37.6	35.6
170.0	100.0	45.3	-17.6	56.5	-39.1	-83.8	73.2
220.0	120.0	59.0	-20.4	79.3	-60.0	-68.2	60.6
250.0	140.0	54.6	-17.7	70.7	-49.8	-59.0	51.3
250.0	120.0	53.5	-17.0	70.3	-55.5	-58.9	55.9
250.0	105.0	51.7	-17.3	68.9	-60.9	-51.3	46.3

Table 33. Average Resilient Strains for Well Graded Texas Gravel at Dry of Optimum.

Stress State		Triaxial Compression		Triaxial Shear		Triaxial Extension	
Stress (kPa)		Strain (με)		Strain (με)		Strain (με)	
Axial	Radial	Axial	Radial	Axial	Radial	Axial	Radial
40.0	25.0	24.6	-3.8	60.7	-21.8	-34.5	13.1
50.0	25.0	39.8	-7.4	47.8	-19.4	-47.3	16.8
70.0	40.0	32.6	-6.0	37.0	-14.3	-47.4	23.6
130.0	60.0	45.7	-9.6	57.5	-28.5	-32.1	19.9
150.0	70.0	40.2	-9.0	52.2	-23.3	-28.6	17.9
170.0	100.0	38.6	-7.7	44.5	-19.4	-55.9	33.1
220.0	120.0	54.2	-9.0	63.8	-28.5	-53.5	29.5
250.0	140.0	48.5	-8.6	56.5	-25.6	-46.0	27.7
250.0	120.0	48.6	-7.6	57.1	-26.8	-44.2	28.7
250.0	105.0	48.3	-7.8	56.3	-28.4	-43.0	22.6

Table 34. Average Resilient Strains for Fine Graded Texas Gravel at Optimum.

Stress State		Triaxial Compression		Triaxial Shear		Triaxial Extension	
Stress (kPa)		Strain (με)		Strain (με)		Strain (με)	
Axial	Radial	Axial	Radial	Axial	Radial	Axial	Radial
40.0	25.0	39.0	-14.9	146.0	-103.9	-97.1	67.8
50.0	25.0	57.5	-20.0	87.2	-68.8	-109.3	73.2
70.0	40.0	41.2	-14.6	62.3	-46.1	-127.1	109.3
130.0	60.0	58.1	-20.6	94.1	-90.9	-59.4	60.1
150.0	70.0	51.2	-16.9	79.3	-69.7	-48.9	50.8
170.0	100.0	51.9	-14.9	73.8	-49.8	-137.3	116.3
220.0	120.0	65.7	-19.9	100.0	-80.5	-96.0	84.5
250.0	140.0	62.7	-17.8	89.2	-63.2	-83.8	67.8
250.0	120.0	60.3	-17.8	84.4	-75.4	-79.9	76.8
250.0	105.0	56.8	-16.8	81.4	-83.0	-63.7	62.7

Table 35. Average Resilient Strains for Fine Graded Texas Gravel at Dry of Optimum.

Stress State		Triaxial Compression		Triaxial Shear		Triaxial Extension	
Stress (kPa)		Strain (με)		Strain (με)		Strain (με)	
Axial	Radial	Axial	Radial	Axial	Radial	Axial	Radial
40.0	25.0	29.8	-6.8	74.5	-26.7	-38.1	16.8
50.0	25.0	49.7	-11.5	59.9	-23.5	-67.6	23.4
70.0	40.0	38.7	-10.1	47.0	-19.0	-63.6	31.7
130.0	60.0	64.6	-18.0	83.4	-43.4	-44.4	27.9
150.0	70.0	58.1	-16.6	74.2	-39.3	-41.0	25.2
170.0	100.0	51.6	-14.5	62.8	-31.6	-82.5	50.3
220.0	120.0	72.9	-21.2	92.3	-50.3	-72.2	45.7
250.0	140.0	67.3	-18.6	83.6	-44.1	-66.9	40.3
250.0	120.0	64.8	-20.0	85.7	-50.5	-67.6	46.0
250.0	105.0	64.9	-19.9	84.1	-55.7	-63.6	40.0

Table 36. Average Resilient Strains for Coarse Graded Texas Gravel at Optimum.

Stress State		Triaxial Compression		Triaxial Shear		Triaxial Extension	
Stress (kPa)		Strain (με)		Strain (με)		Strain (με)	
Axial	Radial	Axial	Radial	Axial	Radial	Axial	Radial
40.0	25.0	31.8	-10.6	93.5	-60.0	-54.1	35.0
50.0	25.0	54.0	-17.2	71.1	-50.1	-77.0	45.8
70.0	40.0	42.6	-14.7	54.0	-36.5	-83.4	66.8
130.0	60.0	59.9	-25.6	86.8	-83.2	-55.9	56.8
150.0	70.0	52.7	-19.9	72.2	-63.7	-46.0	46.4
170.0	100.0	50.0	-20.1	65.6	-50.7	-103.4	93.3
220.0	120.0	64.2	-23.8	87.6	-70.8	-80.6	75.2
250.0	140.0	59.7	-20.8	79.5	-61.1	-70.5	63.9
250.0	120.0	58.7	-21.4	81.5	-68.8	-71.6	72.4
250.0	105.0	56.9	-20.5	79.6	-69.2	-59.7	57.5

Table 37. Average Resilient Strains for Well Graded Minnesota Gravel at Optimum.

Stress State		Triaxial Compression		Triaxial Shear		Triaxial Extension	
Stress (kPa)		Strain (με)		Strain (με)		Strain (με)	
Axial	Radial	Axial	Radial	Axial	Radial	Axial	Radial
40.0	25.0	42.3	-18.2	131.6	-121.9	-98.4	80.7
50.0	25.0	68.5	-37.9	111.7	-121.4	-140.7	121.2
70.0	40.0	49.2	-23.7	75.2	-67.9	-136.0	122.1
130.0	60.0	70.5	-36.5	114.1	-120.5	-76.3	80.3
150.0	70.0	64.6	-29.7	96.8	-95.7	-62.3	66.7
170.0	100.0	61.8	-25.9	84.5	-66.6	-128.7	112.5
220.0	120.0	79.1	-31.6	113.4	-92.3	-103.1	90.9
250.0	140.0	71.3	-27.1	98.0	-75.9	-85.8	75.3
250.0	120.0	68.8	-29.4	99.8	-93.3	-88.8	91.8
250.0	105.0	67.9	-32.0	101.7	-108.9	-81.2	84.1

Table 38. Average Resilient Strains for Well Graded Minnesota Gravel at Dry of Optimum.

Stress State		Triaxial Compression		Triaxial Shear		Triaxial Extension	
Stress (kPa)		Strain (με)		Strain (με)		Strain (με)	
Axial	Radial	Axial	Radial	Axial	Radial	Axial	Radial
40.0	25.0	42.7	-12.4	122.8	-82.4	-84.7	55.0
50.0	25.0	67.2	-23.4	95.3	-74.8	-110.8	69.8
70.0	40.0	48.3	-16.0	65.2	-44.9	-104.8	78.0
130.0	60.0	70.5	-25.7	99.3	-85.7	-60.8	57.4
150.0	70.0	62.3	-21.9	88.5	-68.9	-52.3	49.0
170.0	100.0	58.4	-19.5	76.8	-49.6	-110.4	82.3
220.0	120.0	76.3	-23.6	102.8	-69.6	-88.9	67.9
250.0	140.0	70.2	-20.5	93.1	-57.5	-75.6	58.0
250.0	120.0	68.8	-21.0	93.0	-67.5	-76.2	67.1
250.0	105.0	68.2	-23.9	95.0	-84.5	-77.0	64.7

Table 39. Average Resilient Strains for Well Graded Minnesota Gravel at Wet of Optimum.

Stress State		Triaxial Compression		Triaxial Shear		Triaxial Extension	
Stress (kPa)		Strain (με)		Strain (με)		Strain (με)	
Axial	Radial	Axial	Radial	Axial	Radial	Axial	Radial
40.0	25.0	96.1	-77.4	311.8	-395.6	-483.4	534.8
50.0	25.0	105.5	-83.3	180.7	-262.0	-364.3	413.7
70.0	40.0	88.0	-73.2	151.7	-218.8	-497.1	604.3
130.0	60.0	99.2	-86.2	186.1	-327.6	-171.1	269.8
150.0	70.0	87.5	-69.2	151.8	-259.0	-128.0	216.6
170.0	100.0	87.9	-61.7	151.1	-206.2	-354.0	431.5
220.0	120.0	105.4	-60.9	174.0	-237.6	-203.7	262.5
250.0	140.0	93.5	-52.6	153.2	-196.4	-168.7	215.4
250.0	120.0	90.5	-54.7	149.5	-224.3	-175.1	253.4
250.0	105.0	84.2	-56.2	137.6	-228.5	-129.9	199.4

Table 40. Average Resilient Strains for Fine Graded Minnesota Gravel at Optimum.

Stress State		Triaxial Compression		Triaxial Shear		Triaxial Extension	
Stress (kPa)		Strain (με)		Strain (με)		Strain (με)	
Axial	Radial	Axial	Radial	Axial	Radial	Axial	Radial
40.0	25.0	51.7	-31.8	175.7	-221.0	-189.8	216.1
50.0	25.0	68.4	-42.1	111.5	-156.2	-178.4	195.8
70.0	40.0	52.6	-30.6	82.1	-97.6	-202.6	229.7
130.0	60.0	70.1	-43.6	120.3	-170.2	-91.5	128.5
150.0	70.0	64.4	-37.7	103.9	-135.0	-76.4	99.8
170.0	100.0	63.1	-30.8	92.0	-91.0	-176.1	175.7
220.0	120.0	78.6	-35.7	117.2	-123.6	-123.0	128.0
250.0	140.0	71.0	-30.7	103.2	-98.3	-102.6	102.1
250.0	120.0	68.2	-33.1	106.7	-121.5	-106.5	125.5
250.0	105.0	66.7	-32.5	102.2	-128.1	-89.1	105.2

Table 41. Average Resilient Strains for Fine Graded Minnesota Gravel at Dry of Optimum.

Stress State		Triaxial Compression		Triaxial Shear		Triaxial Extension	
Stress (kPa)		Strain (με)		Strain (με)		Strain (με)	
Axial	Radial	Axial	Radial	Axial	Radial	Axial	Radial
40.0	25.0	40.2	-12.0	116.4	-86.0	-72.2	56.2
50.0	25.0	63.0	-23.5	89.2	-77.0	-104.1	69.8
70.0	40.0	46.4	-17.1	65.7	-49.2	-101.1	87.1
130.0	60.0	70.5	-30.5	101.4	-98.5	-62.3	63.3
150.0	70.0	63.2	-26.6	90.3	-81.2	-53.1	54.4
170.0	100.0	60.1	-20.8	79.7	-57.1	-114.9	95.5
220.0	120.0	79.5	-27.9	109.6	-83.3	-94.6	80.0
250.0	140.0	70.8	-24.6	97.3	-68.7	-82.9	67.2
250.0	120.0	70.2	-24.8	97.0	-80.2	-85.2	76.9
250.0	105.0	67.9	-27.0	98.3	-94.2	-76.1	70.1

Table 42. Average Resilient Strains for Well Graded California Granite at Optimum.

Stress State		Triaxial Compression		Triaxial Shear		Triaxial Extension	
Stress (kPa)		Strain (με)		Strain (με)		Strain (με)	
Axial	Radial	Axial	Radial	Axial	Radial	Axial	Radial
40.0	25.0	47.1	-18.8	148.0	-130.4	-97.4	76.6
50.0	25.0	70.4	-32.9	107.9	-112.2	-141.3	110.1
70.0	40.0	49.7	-19.9	73.7	-62.6	-131.6	111.7
130.0	60.0	76.0	-35.9	113.2	-120.8	-76.3	82.2
150.0	70.0	67.5	-31.3	98.6	-97.3	-65.7	68.4
170.0	100.0	63.0	-23.9	88.0	-68.7	-134.7	111.9
220.0	120.0	79.7	-30.7	113.5	-92.8	-103.6	90.0
250.0	140.0	72.1	-24.8	101.3	-75.7	-90.9	75.6
250.0	120.0	73.0	-26.7	102.7	-88.3	-91.7	88.6
250.0	105.0	69.6	-29.7	103.5	-103.5	-84.1	81.8

Table 43. Average Resilient Strains for Well Graded California Granite at Dry of Optimum.

Stress State		Triaxial Compression		Triaxial Shear		Triaxial Extension	
Stress (kPa)		Strain (με)		Strain (με)		Strain (με)	
Axial	Radial	Axial	Radial	Axial	Radial	Axial	Radial
40.0	25.0	40.4	-11.0	118.8	-84.4	-90.2	61.1
50.0	25.0	62.5	-20.9	90.2	-77.5	-120.5	77.9
70.0	40.0	46.8	-15.0	64.5	-47.0	-116.3	92.5
130.0	60.0	66.7	-24.1	99.8	-96.8	-65.8	66.2
150.0	70.0	62.0	-25.4	88.5	-77.4	-54.8	58.7
170.0	100.0	56.0	-18.2	74.4	-54.7	-112.9	96.5
220.0	120.0	73.5	-23.0	100.5	-77.9	-90.6	78.6
250.0	140.0	67.5	-19.4	89.8	-64.9	-78.2	67.7
250.0	120.0	64.5	-21.4	91.0	-77.8	-79.5	79.5
250.0	105.0	66.3	-25.2	91.6	-87.9	-72.9	70.7

Table 44. Average Resilient Strains for Well Graded California Granite at Wet of Optimum.

Stress State		Triaxial Compression		Triaxial Shear		Triaxial Extension	
Stress (kPa)		Strain (με)		Strain (με)		Strain (με)	
Axial	Radial	Axial	Radial	Axial	Radial	Axial	Radial
40.0	25.0	42.0	-16.2	140.4	-124.8	-108.5	82.8
50.0	25.0	67.8	-33.2	111.3	-117.5	-155.8	124.0
70.0	40.0	52.2	-21.7	76.0	-64.1	-142.5	123.2
130.0	60.0	70.1	-32.9	109.5	-111.9	-74.0	76.5
150.0	70.0	62.1	-25.7	92.7	-91.3	-62.0	64.9
170.0	100.0	60.5	-20.9	82.2	-61.6	-127.9	106.7
220.0	120.0	75.2	-27.3	108.2	-87.2	-98.7	85.9
250.0	140.0	69.4	-23.5	93.7	-71.8	-83.4	72.6
250.0	120.0	68.0	-25.2	100.8	-88.2	-88.7	85.8
250.0	105.0	66.2	-28.3	97.6	-97.6	-77.5	76.2

Table 45. Average Resilient Strains for Fine Graded California Granite at Optimum.

Stress State		Triaxial Compression		Triaxial Shear		Triaxial Extension	
Stress (kPa)		Strain (με)		Strain (με)		Strain (με)	
Axial	Radial	Axial	Radial	Axial	Radial	Axial	Radial
40.0	25.0	47.7	-10.8	134.2	-74.7	-99.1	48.4
50.0	25.0	74.3	-20.9	103.2	-68.2	-131.0	66.1
70.0	40.0	55.7	-15.7	72.6	-42.4	-116.7	73.5
130.0	60.0	74.2	-24.2	107.3	-81.3	-65.6	53.3
150.0	70.0	67.3	-20.0	91.5	-68.0	-53.5	47.6
170.0	100.0	61.8	-17.6	80.5	-49.1	-114.9	83.4
220.0	120.0	79.0	-23.3	107.7	-68.1	-91.8	67.8
250.0	140.0	77.4	-25.2	105.5	-69.1	-91.3	68.5
250.0	120.0	75.7	-25.4	105.0	-80.3	-92.7	79.1
250.0	105.0	71.9	-25.9	100.4	-84.1	-79.4	68.7

Table 46. Average Resilient Strains for Fine Graded California Granite at Dry of Optimum.

Stress State		Triaxial Compression		Triaxial Shear		Triaxial Extension	
Stress (kPa)		Strain (με)		Strain (με)		Strain (με)	
Axial	Radial	Axial	Radial	Axial	Radial	Axial	Radial
40.0	25.0	33.6	-9.2	93.8	-62.1	-61.7	43.0
50.0	25.0	54.7	-15.1	72.4	-55.6	-91.4	53.9
70.0	40.0	42.9	-11.9	55.7	-36.9	-91.4	68.4
130.0	60.0	62.2	-21.7	87.8	-71.7	-52.2	50.7
150.0	70.0	55.1	-18.6	77.7	-59.8	-45.3	42.5
170.0	100.0	53.2	-15.4	66.7	-45.7	-98.8	80.5
220.0	120.0	68.2	-20.5	93.2	-64.4	-78.3	64.3
250.0	140.0	62.2	-17.6	81.8	-54.1	-70.1	54.8
250.0	120.0	63.0	-18.6	84.7	-66.0	-71.6	64.3
250.0	105.0	61.8	-22.0	83.7	-75.2	-65.4	59.7

Table 47. Average Resilient Strains for Fine Graded California Granite at Wet of Optimum.

Stress State		Triaxial Compression		Triaxial Shear		Triaxial Extension	
Stress (kPa)		Strain (με)		Strain (με)		Strain (με)	
Axial	Radial	Axial	Radial	Axial	Radial	Axial	Radial
40.0	25.0	47.4	-23.3	151.1	-136.6	-118.1	91.3
50.0	25.0	67.4	-33.8	113.1	-110.7	-149.7	118.7
70.0	40.0	53.0	-21.0	76.5	-67.7	-145.3	123.8
130.0	60.0	69.8	-31.4	112.3	-116.3	-72.9	81.3
150.0	70.0	63.8	-27.4	99.3	-98.2	-66.1	68.1
170.0	100.0	61.1	-22.2	87.4	-68.0	-139.5	121.7
220.0	120.0	76.1	-29.4	112.6	-95.9	-104.5	95.8
250.0	140.0	72.5	-23.9	99.1	-78.7	-89.4	79.1
250.0	120.0	67.4	-26.5	101.1	-92.0	-90.6	92.5
250.0	105.0	67.9	-28.2	99.9	-105.6	-79.5	81.6

APPENDIX B

TABLE OF MODULI AND POISSON'S RATIO

Table 48. Moduli and Poisson's Ratios for Well Graded Texas Crushed Limestone at Dry of Optimum.

Stress (kPa)		Moduli (MPa)			Poisson's Ratio	
Axial	Radial	Vertical	Horizontal	Shear	Vertical	Horizontal
40.0	25.0	144.0	68.1	40.1	0.173	0.403
50.0	25.0	177.3	72.0	49.7	0.180	0.350
70.0	40.0	237.7	128.0	81.9	0.202	0.373
130.0	60.0	393.3	160.0	107.7	0.180	0.414
150.0	70.0	447.7	200.7	130.3	0.181	0.404
170.0	100.0	460.3	275.7	164.0	0.216	0.405
220.0	120.0	543.3	311.0	182.7	0.196	0.407
250.0	140.0	592.3	377.3	215.3	0.189	0.414
250.0	120.0	604.3	329.7	199.7	0.182	0.392
250.0	105.0	625.3	296.3	185.7	0.166	0.425

Table 49. Moduli and Poisson's Ratios for Well Graded Texas Crushed Limestone at Wet of Optimum.

Stress (kPa)		Moduli (MPa)			Poisson's Ratio	
Axial	Radial	Vertical	Horizontal	Shear	Vertical	Horizontal
40.0	25.0	143.7	63.2	39.4	0.207	0.438
50.0	25.0	169.7	68.7	48.8	0.190	0.359
70.0	40.0	227.3	109.8	73.5	0.225	0.404
130.0	60.0	374.7	145.3	102.1	0.186	0.430
150.0	70.0	426.7	183.3	125.0	0.186	0.430
170.0	100.0	435.0	241.3	145.7	0.228	0.409
220.0	120.0	512.3	266.7	168.0	0.189	0.406
250.0	140.0	575.3	322.0	195.0	0.191	0.407
250.0	120.0	568.3	261.7	172.0	0.176	0.374
250.0	105.0	595.3	250.0	165.3	0.170	0.435

Table 50. Moduli and Poisson's Ratios for Fine Graded Texas Crushed Limestone at Optimum.

Stress (kPa)		Moduli (MPa)			Poisson's Ratio	
Axial	Radial	Vertical	Horizontal	Shear	Vertical	Horizontal
40.0	25.0	124.0	33.6	25.3	0.185	0.402
50.0	25.0	156.3	44.5	36.9	0.175	0.325
70.0	40.0	203.3	72.8	56.8	0.202	0.319
130.0	60.0	360.0	102.2	78.7	0.166	0.390
150.0	70.0	404.3	131.3	97.0	0.167	0.384
170.0	100.0	407.7	179.0	124.0	0.203	0.354
220.0	120.0	503.7	204.7	140.7	0.183	0.392
250.0	140.0	549.7	256.3	168.0	0.182	0.394
250.0	120.0	571.7	210.0	151.0	0.166	0.362
250.0	105.0	211.3	232.3	142.3	0.152	0.412

Table 51. Moduli and Poisson's Ratios for Fine Graded Texas Crushed Limestone at Dry of Optimum.

Stress (kPa)		Moduli (MPa)			Poisson's Ratio	
Axial	Radial	Vertical	Horizontal	Shear	Vertical	Horizontal
40.0	25.0	145.7	69.8	39.4	0.191	0.421
50.0	25.0	189.3	75.5	55.6	0.182	0.455
70.0	40.0	237.0	124.3	78.7	0.218	0.390
130.0	60.0	368.7	153.0	102.3	0.182	0.434
150.0	70.0	428.0	189.3	124.3	0.186	0.425
170.0	100.0	437.3	245.7	154.7	0.208	0.411
220.0	120.0	531.0	284.3	172.3	0.202	0.420
250.0	140.0	589.7	345.7	203.3	0.198	0.424
250.0	120.0	581.7	307.7	187.0	0.186	0.395
250.0	105.0	602.3	274.0	174.0	0.174	0.442

Table 52. Moduli and Poisson's Ratios for Fine Graded Texas Crushed Limestone at Wet of Optimum.

Stress (kPa)		Moduli (MPa)			Poisson's Ratio	
Axial	Radial	Vertical	Horizontal	Shear	Vertical	Horizontal
40.0	25.0	75.5	11.8	13.2	0.217	0.222
50.0	25.0	116.0	23.3	24.1	0.166	0.216
70.0	40.0	163.0	41.4	38.9	0.208	0.240
130.0	60.0	331.7	74.9	63.7	0.152	0.361
150.0	70.0	389.0	97.7	80.4	0.154	0.354
170.0	100.0	357.0	129.7	100.7	0.198	0.317
220.0	120.0	468.0	156.7	117.3	0.176	0.362
250.0	140.0	522.3	200.3	144.0	0.175	0.375
250.0	120.0	553.7	174.3	135.3	0.157	0.343
250.0	105.0	627.7	168.3	132.3	0.146	0.404

Table 53. Moduli and Poisson's Ratios for Coarse Graded Texas Crushed Limestone at Optimum.

Stress (kPa)		Moduli (MPa)			Poisson's Ratio	
Axial	Radial	Vertical	Horizontal	Shear	Vertical	Horizontal
40.0	25.0	119.3	67.7	38.1	0.171	0.369
50.0	25.0	151.3	70.1	46.6	0.177	0.355
70.0	40.0	208.0	117.7	72.3	0.203	0.380
130.0	60.0	351.0	149.7	101.8	0.167	0.384
150.0	70.0	394.0	180.7	120.0	0.169	0.380
170.0	100.0	407.0	244.7	148.3	0.190	0.381
220.0	120.0	526.0	281.0	171.3	0.173	0.467
250.0	140.0	543.7	327.0	190.7	0.187	0.382
250.0	120.0	547.7	283.7	180.3	0.164	0.355
250.0	105.0	570.0	262.7	171.0	0.160	0.415

Table 54. Moduli and Poisson's Ratios for Well Graded Texas Gravel at Optimum.

Stress (kPa)		Moduli (MPa)			Poisson's Ratio	
Axial	Radial	Vertical	Horizontal	Shear	Vertical	Horizontal
40.0	25.0	173.5	120.0	58.6	0.180	0.375
50.0	25.0	205.5	116.5	69.8	0.187	0.427
70.0	40.0	261.0	149.0	90.6	0.216	0.408
130.0	60.0	383.0	164.0	108.0	0.180	0.427
150.0	70.0	416.5	199.0	128.0	0.166	0.393
170.0	100.0	452.5	232.0	157.0	0.199	0.409
220.0	120.0	507.5	252.5	161.5	0.174	0.378
250.0	140.0	557.0	300.5	187.0	0.177	0.387
250.0	120.0	562.0	274.0	178.5	0.158	0.352
250.0	105.0	601.0	259.0	173.5	0.150	0.424

Table 55. Moduli and Poisson's Ratios for Well Graded Texas Gravel at Dry of Optimum.

Stress (kPa)		Moduli (MPa)			Poisson's Ratio	
Axial	Radial	Vertical	Horizontal	Shear	Vertical	Horizontal
40.0	25.0	195.0	250.0	90.9	0.200	0.453
50.0	25.0	250.0	264.0	112.0	0.198	0.429
70.0	40.0	305.0	333.0	146.0	0.199	0.425
130.0	60.0	434.0	368.0	174.0	0.180	0.392
150.0	70.0	489.0	450.0	199.0	0.204	0.382
170.0	100.0	519.0	493.0	235.0	0.188	0.389
220.0	120.0	537.0	533.0	244.0	0.165	0.348
250.0	140.0	612.0	583.0	274.0	0.167	0.351
250.0	120.0	607.0	572.0	268.0	0.148	0.304
250.0	105.0	621.0	555.0	266.0	0.148	0.406

Table 56. Moduli and Poisson's Ratios for Well Graded Texas Gravel at Wet of Optimum.

Stress (kPa)		Moduli (MPa)			Poisson's Ratio	
Axial	Radial	Vertical	Horizontal	Shear	Vertical	Horizontal
40.0	25.0	48.2	25.6	14.3	0.160	0.212
50.0	25.0	88.1	36.1	26.1	0.140	0.250
70.0	40.0	106.0	50.5	36.9	0.145	0.109
130.0	60.0	240.0	82.9	59.7	0.138	0.362
150.0	70.0	261.0	135.0	83.1	0.125	0.250
170.0	100.0	238.0	121.0	85.4	0.155	0.132
220.0	120.0	294.0	198.0	115.0	0.162	0.169
250.0	140.0	318.0	298.0	142.0	0.152	0.053
250.0	120.0	376.0	464.0	188.0	0.152	0.174
250.0	105.0	470.0	546.0	238.0	0.118	0.406

Table 57. Moduli and Poisson's Ratios for Fine Graded Texas Gravel at Optimum.

Stress (kPa)		Moduli (MPa)			Poisson's Ratio	
Axial	Radial	Vertical	Horizontal	Shear	Vertical	Horizontal
40.0	25.0	104.0	56.1	30.0	0.193	0.348
50.0	25.0	147.0	76.6	48.1	0.162	0.236
70.0	40.0	192.0	107.0	69.2	0.180	0.168
130.0	60.0	308.0	123.0	81.1	0.137	0.299
150.0	70.0	356.0	157.0	101.0	0.141	0.278
170.0	100.0	310.0	199.0	121.0	0.165	0.147
220.0	120.0	393.0	202.0	125.0	0.147	0.259
250.0	140.0	428.0	251.0	148.0	0.159	0.289
250.0	120.0	455.0	210.0	141.0	0.134	0.280
250.0	105.0	504.0	201.0	137.0	0.119	0.332

Table 58. Moduli and Poisson's Ratios for Fine Graded Texas Gravel at Dry of Optimum.

Stress (kPa)		Moduli (MPa)			Poisson's Ratio	
Axial	Radial	Vertical	Horizontal	Shear	Vertical	Horizontal
40.0	25.0	172.0	192.0	74.1	0.266	0.571
50.0	25.0	196.0	208.0	90.0	0.239	0.502
70.0	40.0	255.0	253.0	114.0	0.251	0.487
130.0	60.0	319.0	238.0	118.0	0.213	0.486
150.0	70.0	356.0	260.0	132.0	0.215	0.501
170.0	100.0	392.0	304.0	159.0	0.219	0.463
220.0	120.0	422.0	300.0	158.0	0.212	0.483
250.0	140.0	457.0	340.0	176.0	0.211	0.485
250.0	120.0	466.0	304.0	165.0	0.205	0.455
250.0	105.0	478.0	281.0	161.0	0.190	0.513

Table 59. Moduli and Poisson's Ratios for Coarse Graded Texas Gravel at Optimum.

Stress (kPa)		Moduli (MPa)			Poisson's Ratio	
Axial	Radial	Vertical	Horizontal	Shear	Vertical	Horizontal
40.0	25.0	152.0	90.9	49.3	0.202	0.469
50.0	25.0	181.5	101.5	62.4	0.173	0.380
70.0	40.0	230.5	128.0	83.3	0.191	0.382
130.0	60.0	337.0	124.0	88.8	0.162	0.388
150.0	70.0	385.0	158.5	111.0	0.160	0.371
170.0	100.0	396.0	186.0	129.0	0.189	0.370
220.0	120.0	465.0	211.0	142.5	0.172	0.362
250.0	140.0	505.5	245.5	161.5	0.173	0.372
250.0	120.0	507.5	224.5	151.5	0.162	0.337
250.0	105.0	541.0	229.5	153.0	0.158	0.401

Table 60. Moduli and Poisson's Ratios for Well Graded Minnesota Gravel at Optimum.

Stress (kPa)		Moduli (MPa)			Poisson's Ratio	
Axial	Radial	Vertical	Horizontal	Shear	Vertical	Horizontal
40.0	25.0	110.0	43.2	29.6	0.175	0.403
50.0	25.0	131.0	41.7	32.2	0.168	0.324
70.0	40.0	186.0	72.4	52.4	0.191	0.347
130.0	60.0	276.0	87.0	63.9	0.168	0.389
150.0	70.0	308.0	108.0	77.9	0.164	0.378
170.0	100.0	318.0	146.0	99.3	0.192	0.389
220.0	120.0	371.0	165.0	109.0	0.182	0.389
250.0	140.0	420.0	199.0	129.0	0.182	0.398
250.0	120.0	431.0	164.0	117.0	0.165	0.366
250.0	105.0	449.0	145.0	107.0	0.156	0.423

Table 61. Moduli and Poisson's Ratios for Well Graded Minnesota Gravel at Dry of Optimum.

Stress (kPa)		Moduli (MPa)			Poisson's Ratio	
Axial	Radial	Vertical	Horizontal	Shear	Vertical	Horizontal
40.0	25.0	106.0	65.4	36.6	0.178	0.385
50.0	25.0	137.0	69.1	44.1	0.168	0.336
70.0	40.0	192.0	110.0	68.2	0.188	0.354
130.0	60.0	282.0	122.0	81.1	0.160	0.380
150.0	70.0	318.0	151.0	95.3	0.170	0.371
170.0	100.0	333.0	198.0	119.0	0.198	0.394
220.0	120.0	383.0	221.0	131.0	0.180	0.388
250.0	140.0	422.0	267.0	149.0	0.186	0.386
250.0	120.0	428.0	229.0	140.0	0.165	0.354
250.0	105.0	438.0	189.0	125.0	0.155	0.420

Table 62. Moduli and Poisson's Ratios for Well Graded Minnesota Gravel at Wet of Optimum.

Stress (kPa)		Moduli (MPa)			Poisson's Ratio	
Axial	Radial	Vertical	Horizontal	Shear	Vertical	Horizontal
40.0	25.0	47.3	10.6	10.6	0.209	0.281
50.0	25.0	75.3	17.1	16.9	0.166	0.186
70.0	40.0	102.0	19.3	20.2	0.193	0.242
130.0	60.0	195.0	30.2	29.2	0.142	0.314
150.0	70.0	226.0	37.9	36.5	0.136	0.303
170.0	100.0	206.0	45.6	42.0	0.170	0.282
220.0	120.0	268.0	63.4	54.7	0.145	0.299
250.0	140.0	304.0	77.0	64.4	0.149	0.305
250.0	120.0	312.0	66.7	60.2	0.135	0.281
250.0	105.0	361.0	67.3	61.5	0.127	0.358

Table 63. Moduli and Poisson's Ratios for Fine Graded Minnesota Gravel at Optimum.

Stress (kPa)		Moduli (MPa)			Poisson's Ratio	
Axial	Radial	Vertical	Horizontal	Shear	Vertical	Horizontal
40.0	25.0	85.9	21.9	18.9	0.169	0.287
50.0	25.0	122.0	30.6	28.0	0.142	0.208
70.0	40.0	166.0	46.6	41.7	0.174	0.245
130.0	60.0	275.0	60.2	51.6	0.143	0.314
150.0	70.0	304.0	75.5	62.8	0.148	0.344
170.0	100.0	293.0	105.0	82.0	0.176	0.318
220.0	120.0	362.0	123.0	93.4	0.157	0.341
250.0	140.0	407.0	154.0	112.0	0.166	0.355
250.0	120.0	418.0	127.0	98.6	0.150	0.320
250.0	105.0	446.0	123.0	97.7	0.138	0.373

Table 64. Moduli and Poisson's Ratios for Fine Graded Minnesota Gravel at Dry of Optimum.

Stress (kPa)		Moduli (MPa)			Poisson's Ratio	
Axial	Radial	Vertical	Horizontal	Shear	Vertical	Horizontal
40.0	25.0	116.0	63.2	37.1	0.161	0.362
50.0	25.0	148.0	66.5	45.1	0.162	0.344
70.0	40.0	200.0	102.0	65.3	0.185	0.330
130.0	60.0	288.0	105.0	75.0	0.161	0.408
150.0	70.0	323.0	127.0	87.5	0.168	0.404
170.0	100.0	324.0	173.0	110.0	0.183	0.369
220.0	120.0	372.0	184.0	117.0	0.177	0.391
250.0	140.0	419.0	223.0	136.0	0.188	0.400
250.0	120.0	419.0	192.0	127.0	0.164	0.371
250.0	105.0	446.0	170.0	117.0	0.156	0.428

Table 65. Moduli and Poisson's Ratios for Well Graded California Granite at Optimum.

Stress (kPa)		Moduli (MPa)			Poisson's Ratio	
Axial	Radial	Vertical	Horizontal	Shear	Vertical	Horizontal
40.0	25.0	99.0	41.8	26.9	0.171	0.419
50.0	25.0	126.0	45.2	34.1	0.158	0.310
70.0	40.0	178.0	79.8	55.1	0.179	0.319
130.0	60.0	261.0	85.2	64.1	0.157	0.383
150.0	70.0	297.0	105.0	76.6	0.166	0.393
170.0	100.0	307.0	146.0	95.7	0.183	0.368
220.0	120.0	365.0	166.0	109.0	0.177	0.388
250.0	140.0	400.0	204.0	127.0	0.177	0.372
250.0	120.0	401.0	174.0	118.0	0.162	0.348
250.0	105.0	430.0	154.0	109.0	0.157	0.411

Table 66. Moduli and Poisson's Ratios for Well Graded California Granite at Dry of Optimum.

Stress (kPa)		Moduli (MPa)			Poisson's Ratio	
Axial	Radial	Vertical	Horizontal	Shear	Vertical	Horizontal
40.0	25.0	105.0	64.6	36.9	0.157	0.309
50.0	25.0	136.0	66.9	44.7	0.148	0.255
70.0	40.0	185.0	105.0	67.3	0.173	0.269
130.0	60.0	282.0	110.0	76.3	0.143	0.328
150.0	70.0	324.0	131.0	90.4	0.168	0.359
170.0	100.0	340.0	181.0	116.0	0.171	0.327
220.0	120.0	391.0	198.0	126.0	0.161	0.341
250.0	140.0	429.0	237.0	145.0	0.159	0.330
250.0	120.0	444.0	201.0	133.0	0.150	0.312
250.0	105.0	462.0	178.0	125.0	0.151	0.411

Table 67. Moduli and Poisson's Ratios for Well Graded California Granite at Wet of Optimum.

Stress (kPa)		Moduli (MPa)			Poisson's Ratio	
Axial	Radial	Vertical	Horizontal	Shear	Vertical	Horizontal
40.0	25.0	101.0	44.0	28.3	0.166	0.354
50.0	25.0	122.0	43.7	32.8	0.158	0.261
70.0	40.0	170.0	75.9	53.5	0.185	0.311
130.0	60.0	276.0	93.4	67.8	0.163	0.375
150.0	70.0	311.0	114.0	81.5	0.155	0.349
170.0	100.0	313.0	161.0	104.0	0.178	0.341
220.0	120.0	381.0	178.0	115.0	0.172	0.365
250.0	140.0	424.0	211.0	136.0	0.170	0.370
250.0	120.0	418.0	179.0	119.0	0.159	0.339
250.0	105.0	457.0	163.0	115.0	0.157	0.417

Table 68. Moduli and Poisson's Ratios for Fine Graded California Granite at Optimum.

Stress (kPa)		Moduli (MPa)			Poisson's Ratio	
Axial	Radial	Vertical	Horizontal	Shear	Vertical	Horizontal
40.0	25.0	88.9	74.2	35.9	0.177	0.374
50.0	25.0	116.0	77.2	43.8	0.169	0.300
70.0	40.0	164.0	117.0	65.2	0.196	0.364
130.0	60.0	258.0	132.0	79.5	0.169	0.383
150.0	70.0	293.0	155.0	94.1	0.158	0.356
170.0	100.0	308.0	203.0	116.0	0.186	0.355
220.0	120.0	364.0	229.0	128.0	0.184	0.378
250.0	140.0	378.0	222.0	129.0	0.193	0.403
250.0	120.0	383.0	192.0	121.0	0.170	0.366
250.0	105.0	419.0	188.0	122.0	0.165	0.420

Table 69. Moduli and Poisson's Ratios for Fine Graded California Granite at Dry of Optimum.

Stress (kPa)		Moduli (MPa)			Poisson's Ratio	
Axial	Radial	Vertical	Horizontal	Shear	Vertical	Horizontal
40.0	25.0	138.0	86.2	48.1	0.170	0.363
50.0	25.0	164.0	92.1	58.6	0.144	0.280
70.0	40.0	210.0	134.0	80.9	0.170	0.297
130.0	60.0	318.0	145.0	94.0	0.162	0.361
150.0	70.0	359.0	175.0	109.0	0.166	0.364
170.0	100.0	362.0	212.0	133.0	0.167	0.334
220.0	120.0	425.0	242.0	143.0	0.171	0.357
250.0	140.0	471.0	283.0	166.0	0.173	0.363
250.0	120.0	463.0	236.0	149.0	0.152	0.337
250.0	105.0	498.0	209.0	142.0	0.154	0.421

Table 70. Moduli and Poisson's Ratios for Fine Graded California Granite at Dry of Optimum.

Stress (kPa)		Moduli (MPa)			Poisson's Ratio	
Axial	Radial	Vertical	Horizontal	Shear	Vertical	Horizontal
40.0	25.0	99.0	37.9	26.1	0.197	0.443
50.0	25.0	124.0	46.7	33.5	0.171	0.272
70.0	40.0	166.0	72.6	52.0	0.173	0.312
130.0	60.0	272.0	91.6	65.6	0.153	0.338
150.0	70.0	298.0	108.0	75.9	0.157	0.353
170.0	100.0	299.0	147.0	96.6	0.177	0.311
220.0	120.0	372.0	162.0	108.0	0.170	0.354
250.0	140.0	402.0	195.0	127.0	0.163	0.350
250.0	120.0	422.0	170.0	117.0	0.159	0.330
250.0	105.0	442.0	151.0	110.0	0.146	0.398

APPENDIX C

VERTICAL AND HORIZONTAL STRESS DISTRIBUTION

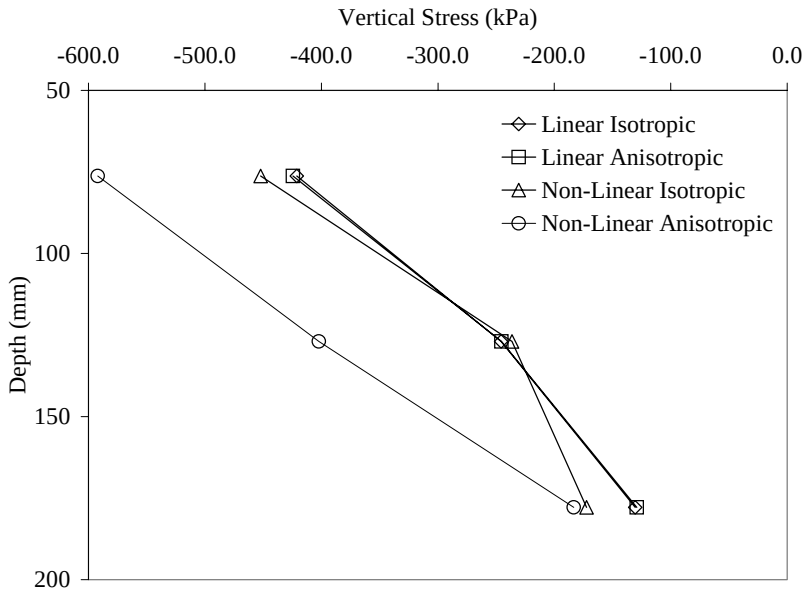

Figure 49. Vertical Stress for 50-mm HMA, 150-mm Base, and 20.7-MPa Subgrade.

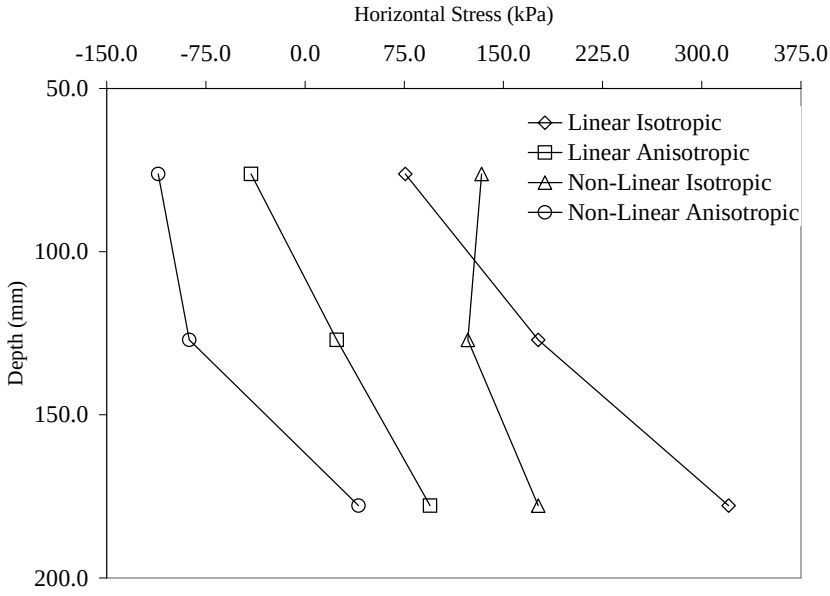

Figure 50. Horizontal Stress for 50-mm HMA, 150-mm Base, and 20.7-MPa Subgrade.

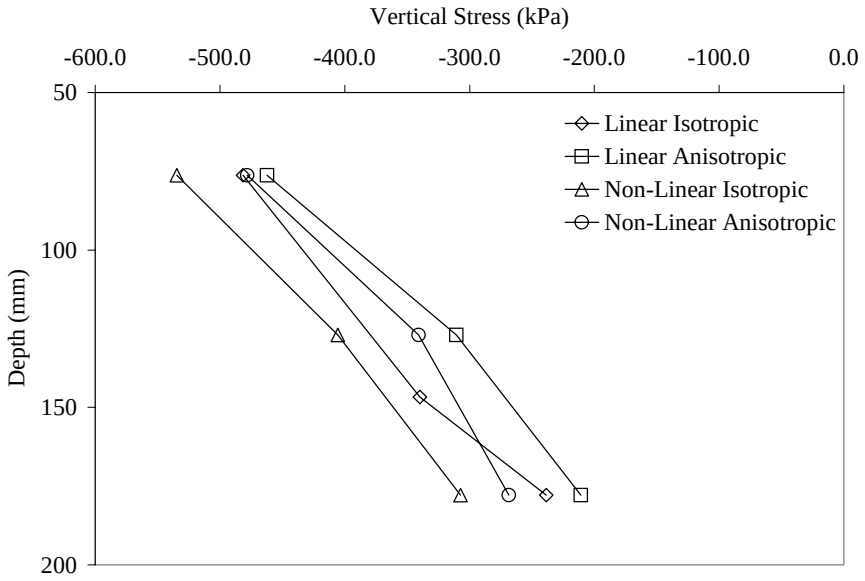

Figure 51. Vertical Stress for 50-mm HMA, 150-mm Base and 103.4-MPa Subgrade.

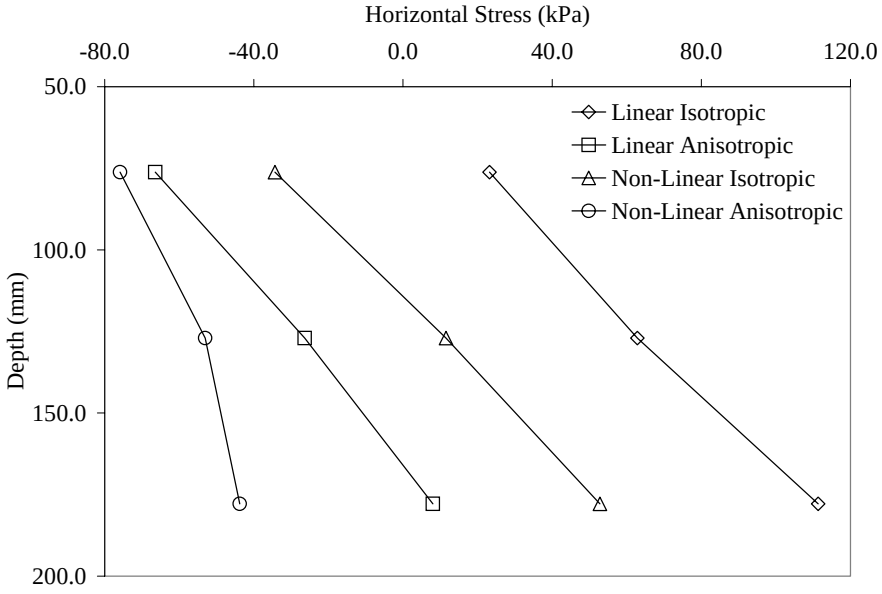

Figure 52. Horizontal Stress for 50-mm HMA, 150-mm Base and 103.4-MPa Subgrade.

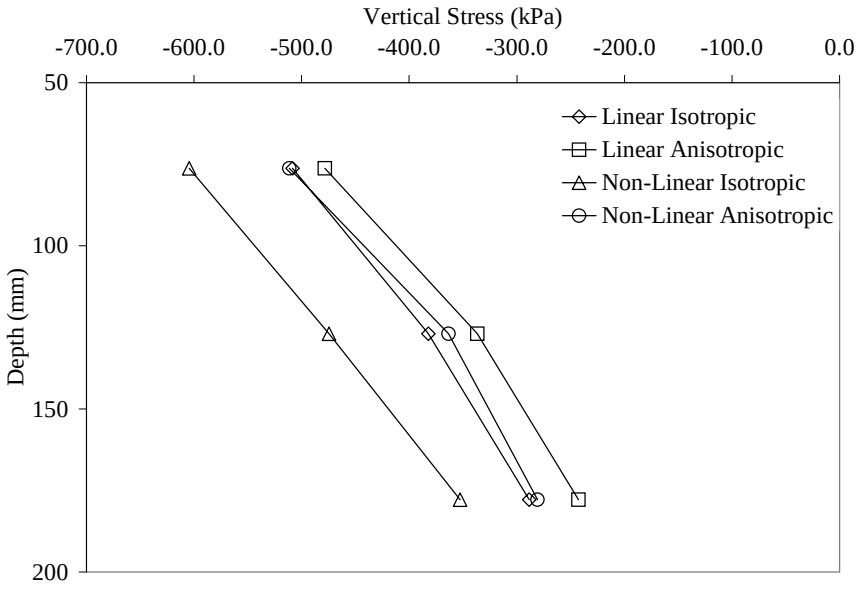

Figure 53. Vertical Stress for 50-mm HMA, 150-mm Base and 206.8-MPa Subgrade.

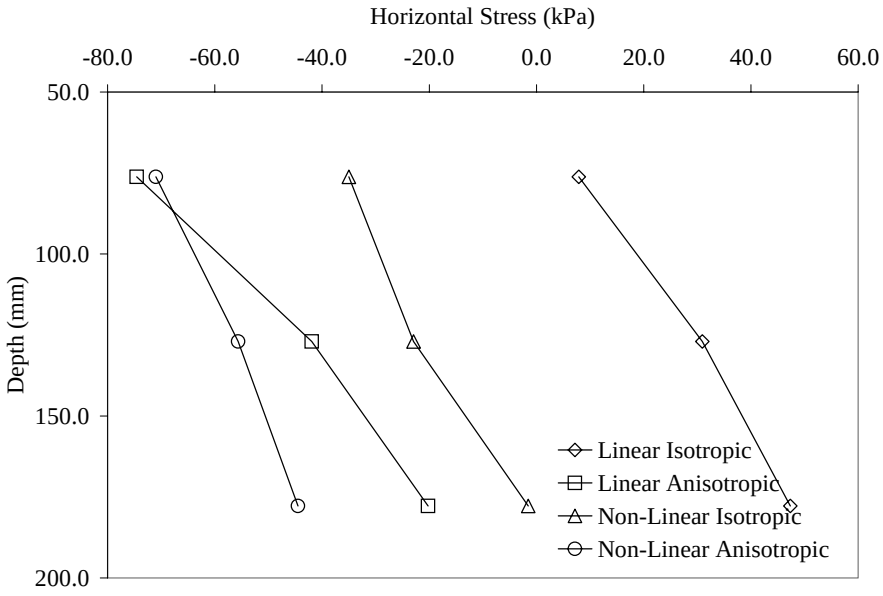

Figure 54 Horizontal Stress for 50-mm HMA, 150-mm Base and 206.8-MPa Subgrade.

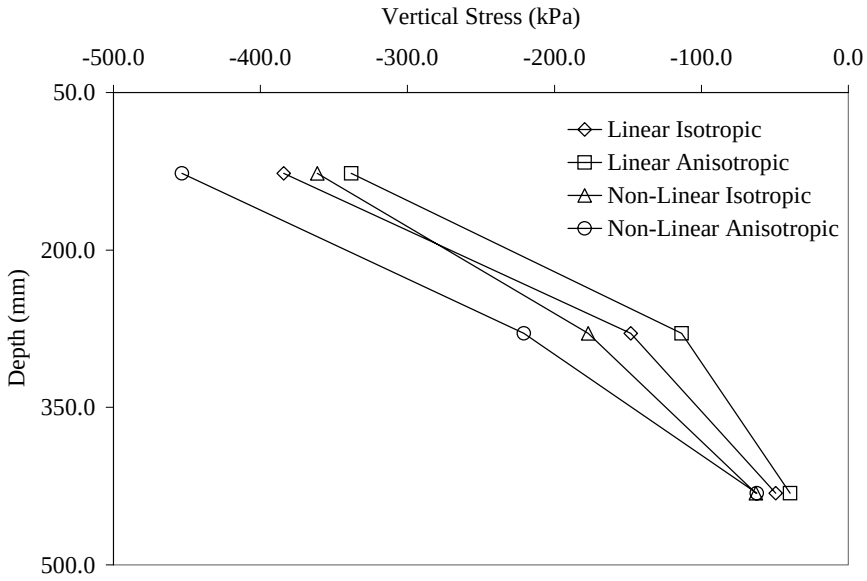

Figure 55. Vertical Stress for 50-mm HMA, 450-mm Base and 20.7-MPa Subgrade.

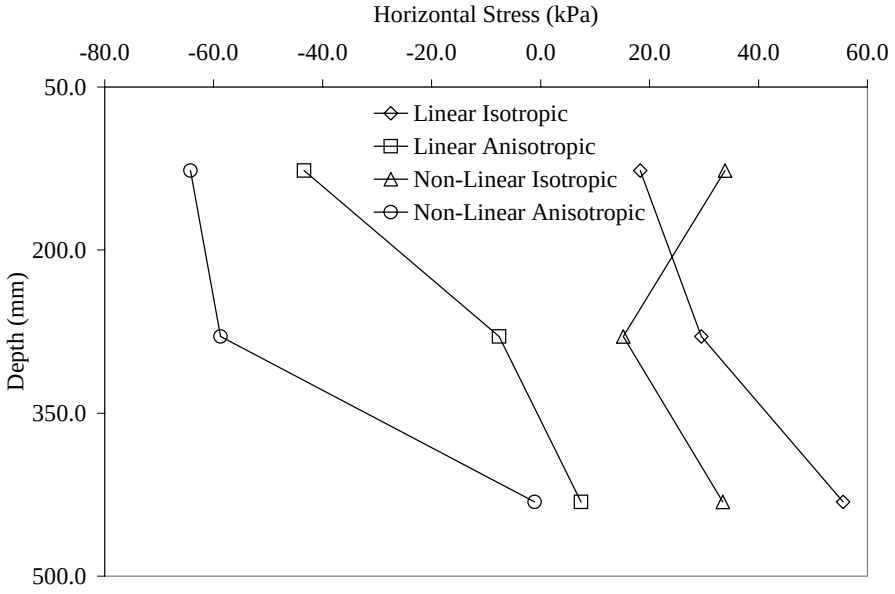

Figure 56. Horizontal Stress for 50-mm HMA, 450-mm Base and 20.7-MPa Subgrade.

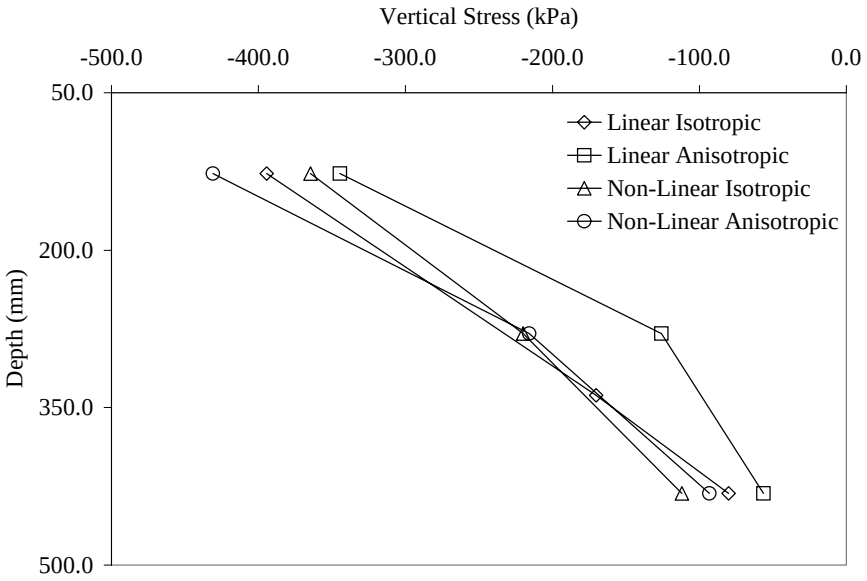

Figure 57. Vertical Stress for 50-mm HMA, 450-mm Base and 103.4-MPa Subgrade.

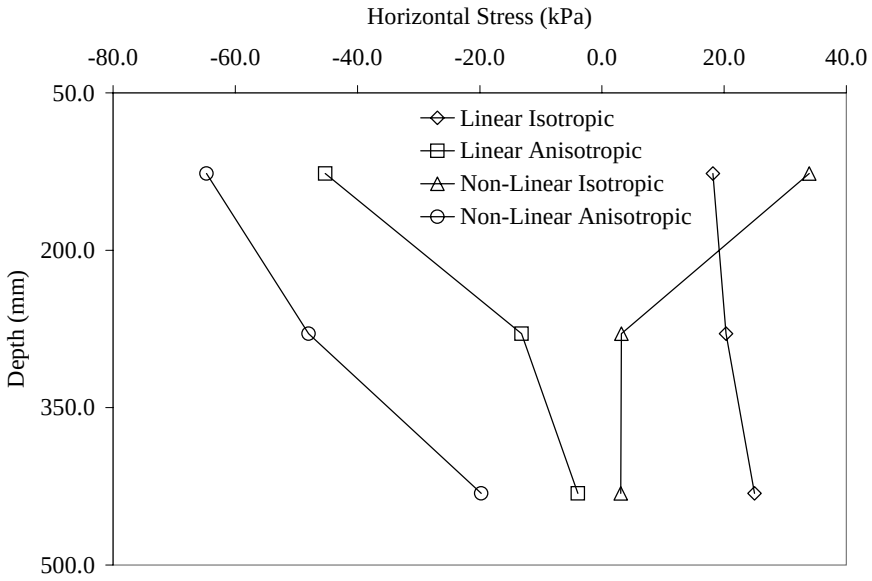

Figure 58. Horizontal Stress for 50-mm HMA, 450-mm Base and 103.4-MPa Subgrade.

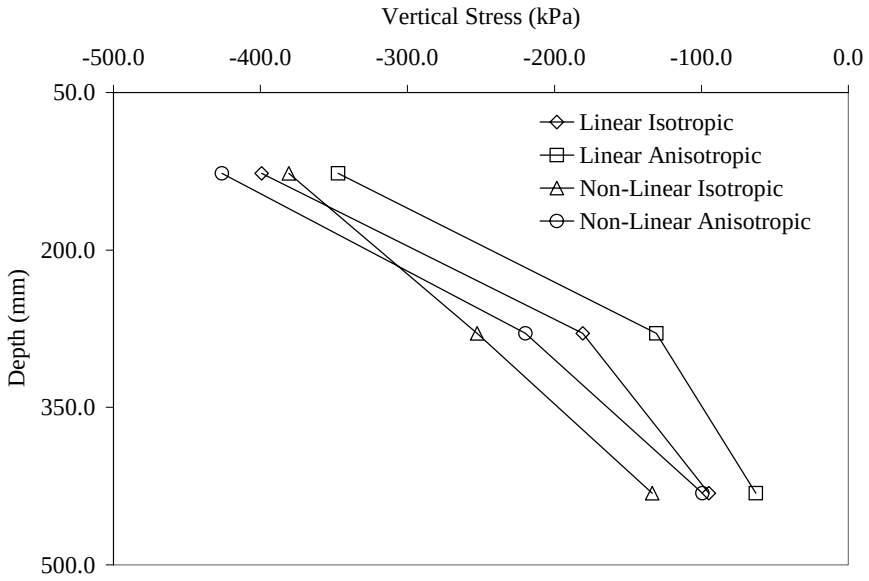

Figure 59. Vertical Stress for 50-mm HMA, 450-mm Base and 206.8-MPa Subgrade.

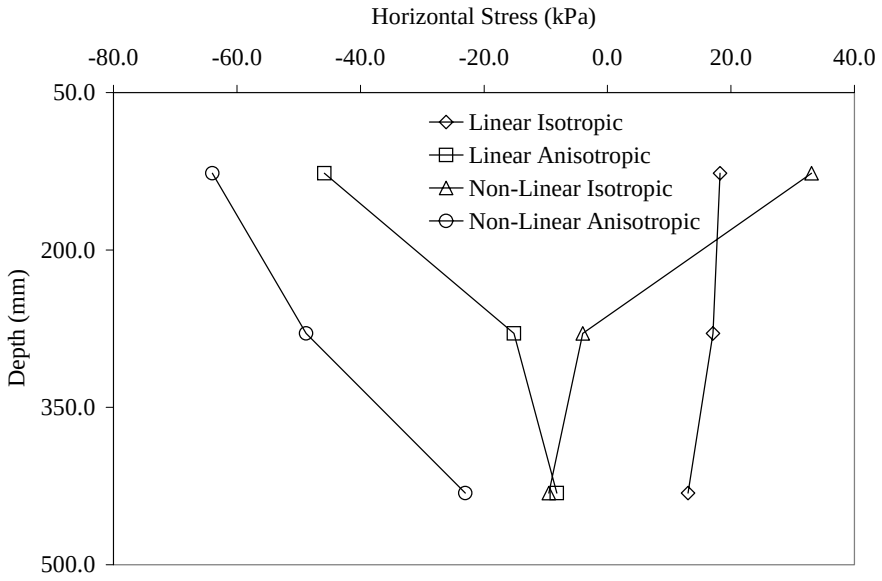

Figure 60. Horizontal Stress for 50-mm HMA, 450-mm Base and 206.8-MPa Subgrade.

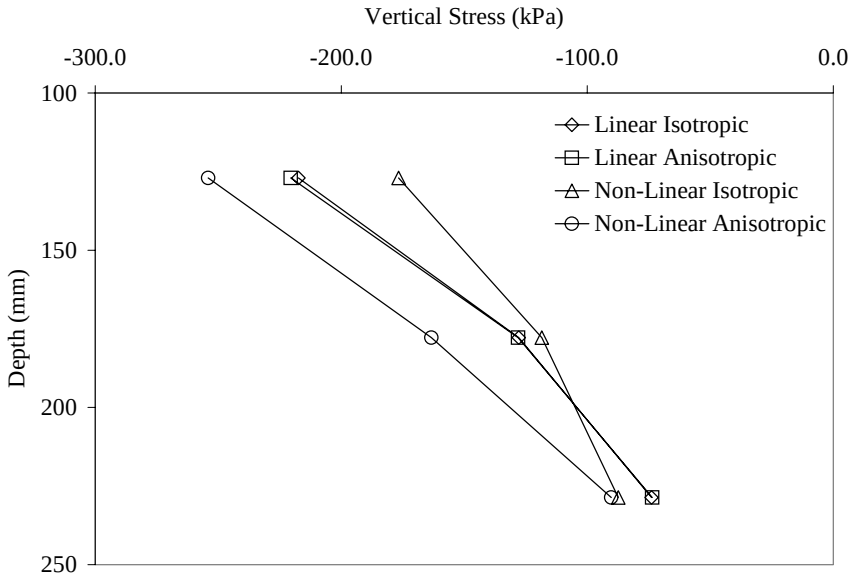

Figure 61. Vertical Stress for 100-mm HMA, 150-mm Base and 20.7-MPa Subgrade.

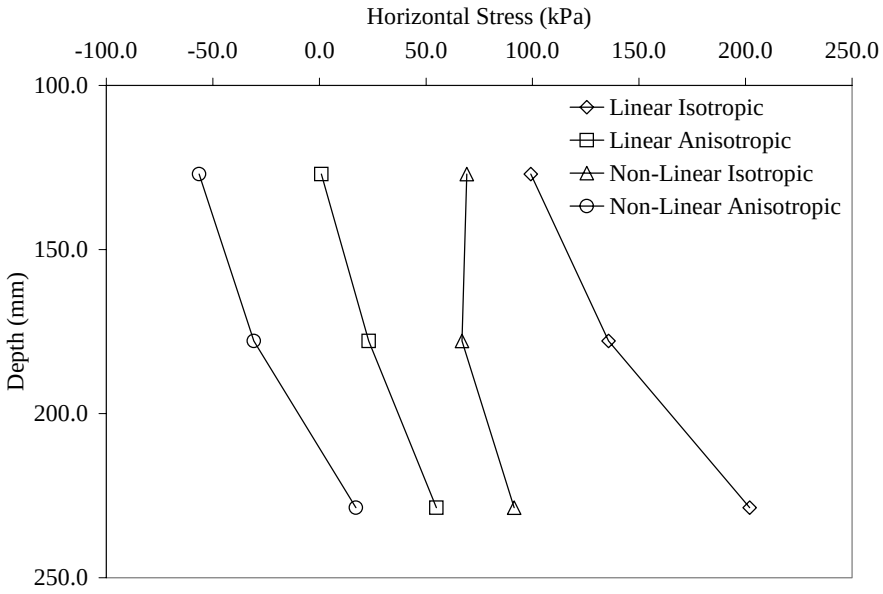

Figure 62. Horizontal Stress for 100-mm HMA, 150-mm Base and 20.7-MPa Subgrade.

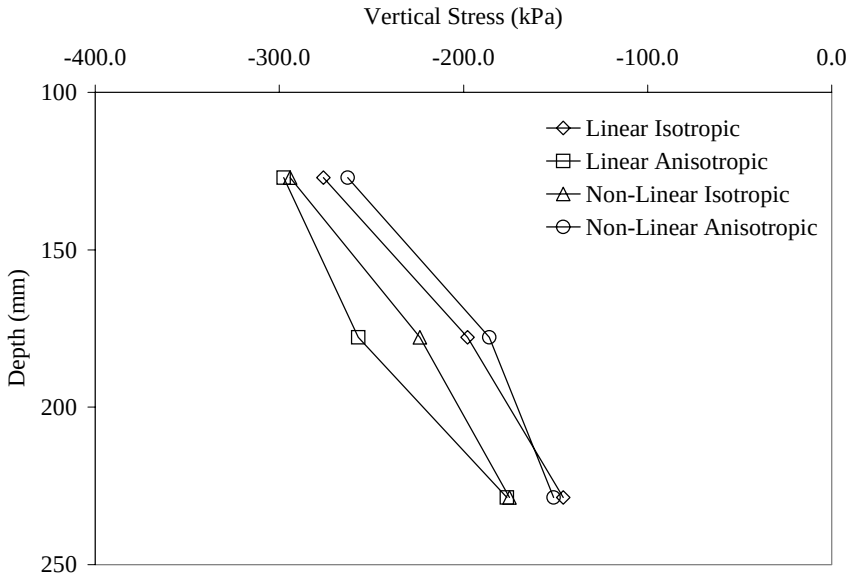

Figure 63. Vertical Stress for 100-mm HMA, 150-mm Base and 103.4-MPa Subgrade.

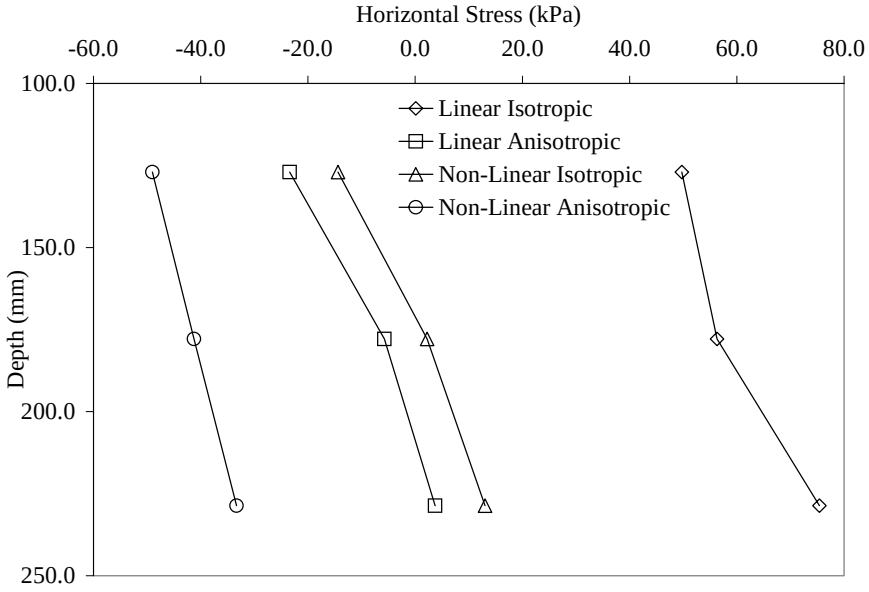

Figure 64. Horizontal Stress for 100-mm HMA, 150-mm Base and 103.4-MPa Subgrade.

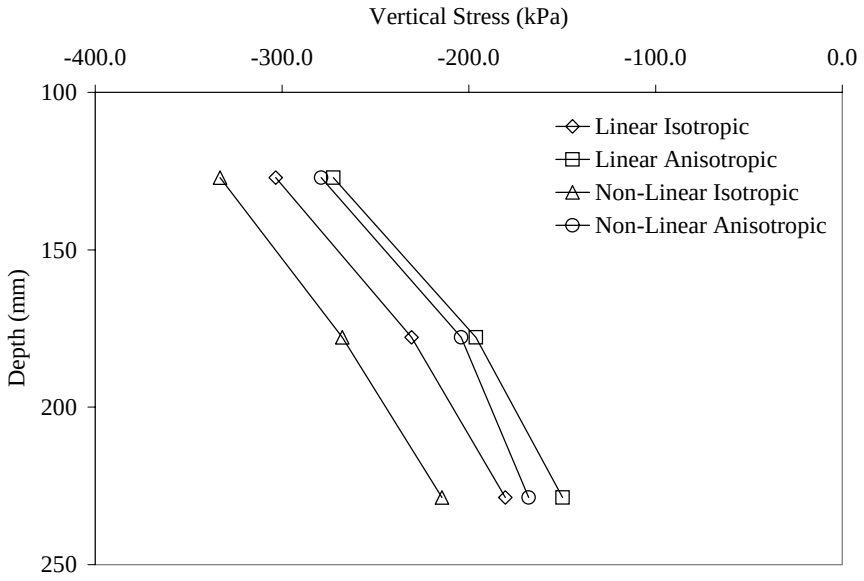

Figure 65. Vertical Stress for 100-mm HMA, 150-mm Base and 206.8-MPa Subgrade.

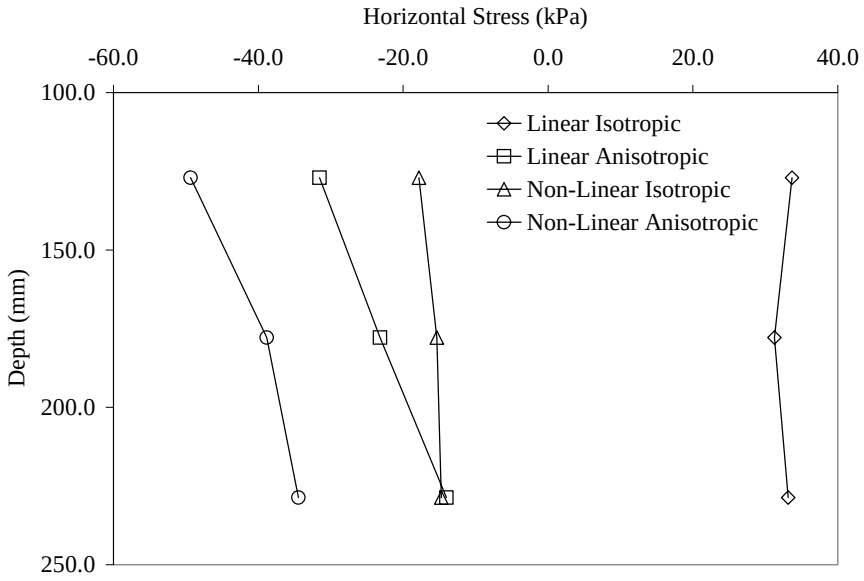

Figure 66. Horizontal Stress for 100-mm HMA, 150-mm Base and 206.8-MPa Subgrade.

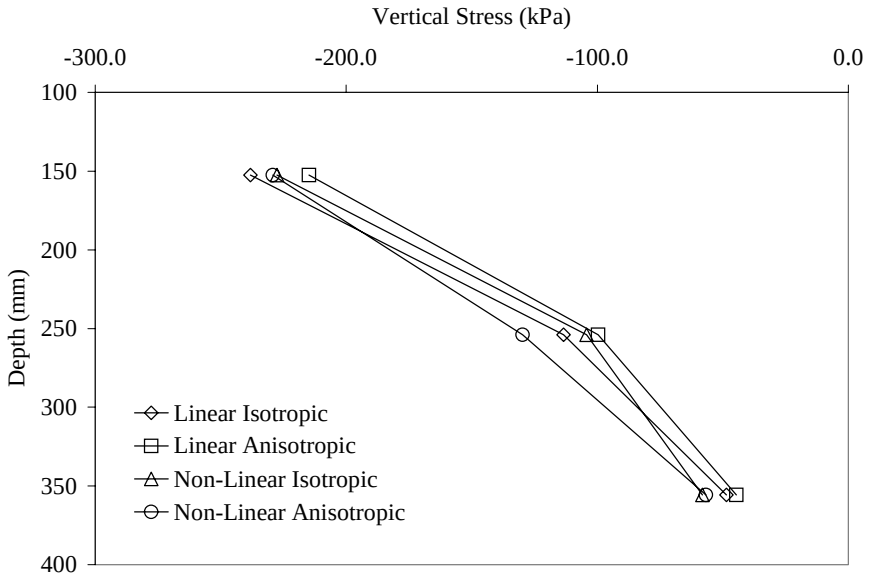

Figure 67. Vertical Stress for 100-mm HMA, 300-mm Base and 20.7-MPa Subgrade.

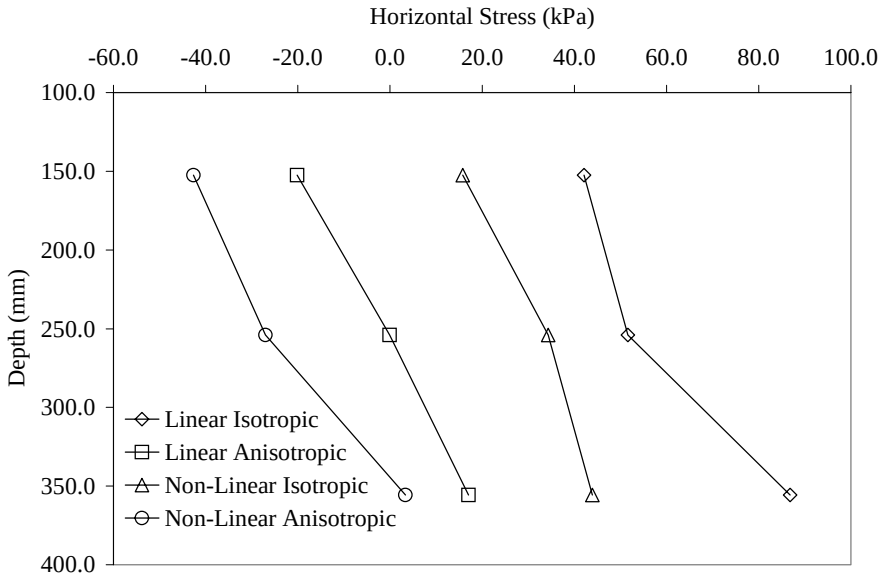

Figure 68. Vertical Stress for 100-mm HMA, 300-mm Base and 20.7-MPa Subgrade.

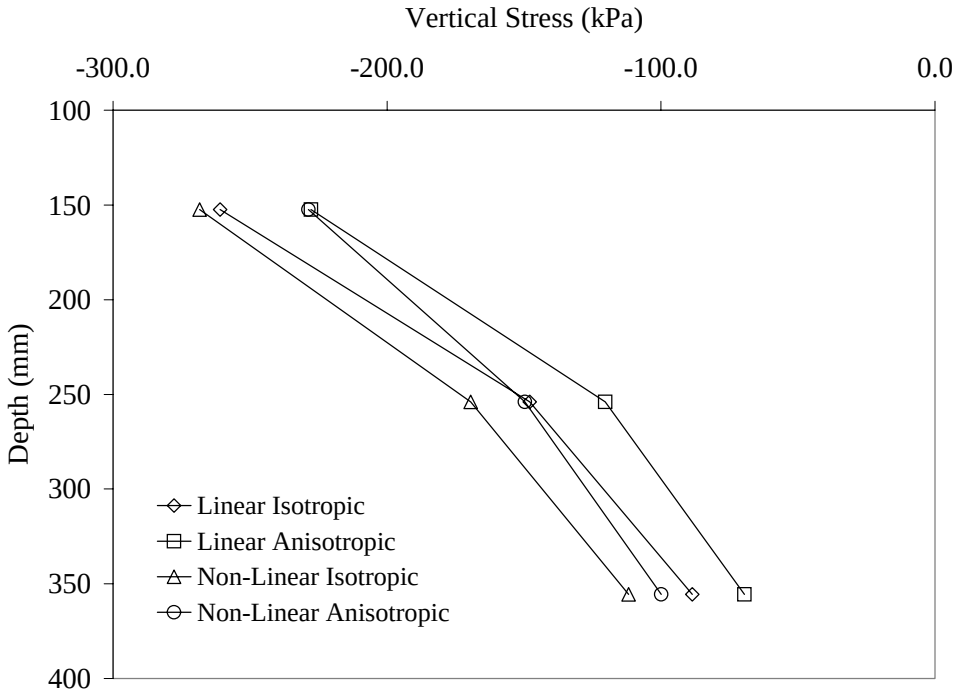

Figure 69. Vertical Stress for 100-mm HMA, 300-mm Base and 103.4-Mpa Subgrade.

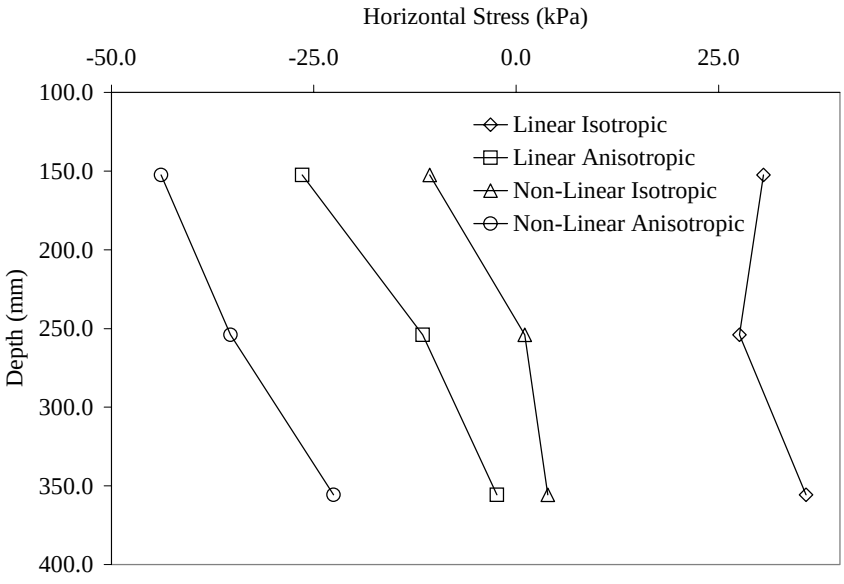

Figure 70. Horizontal Stress for 100-mm HMA, 300-mm Base and 103.4-MPa Subgrade.

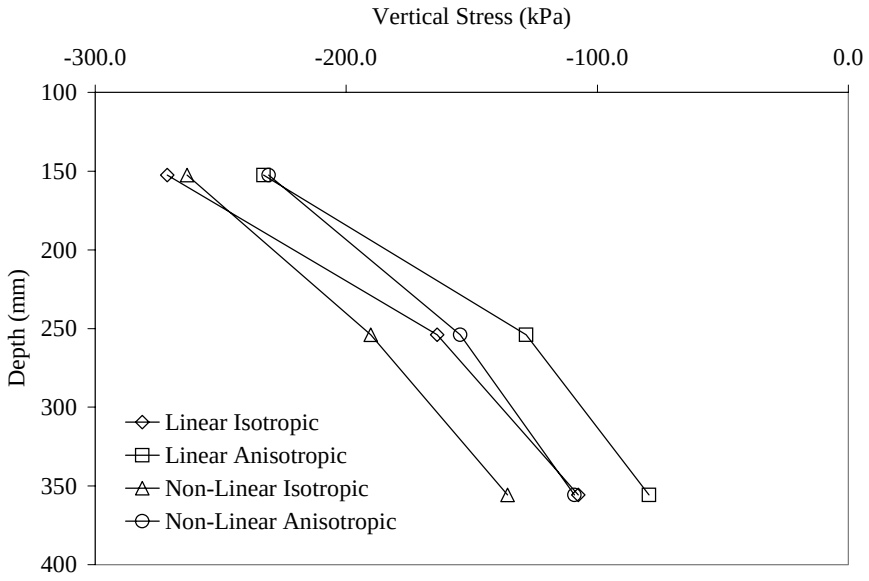

Figure 71. Vertical Stress for 100-mm HMA, 300-mm Base and 206.8-MPa Subgrade.

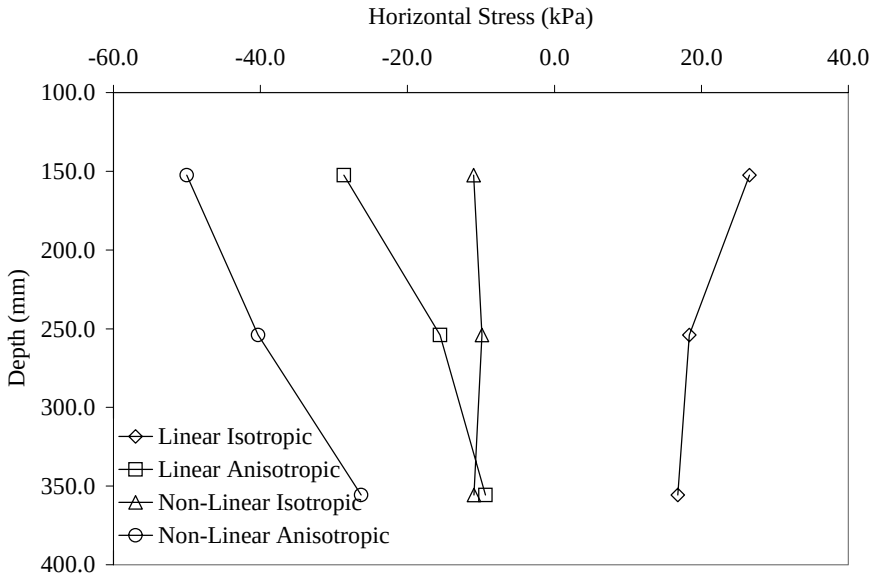

Figure 72. Horizontal Stress for 100-mm HMA, 300-mm Base and 206.8-MPa Subgrade.

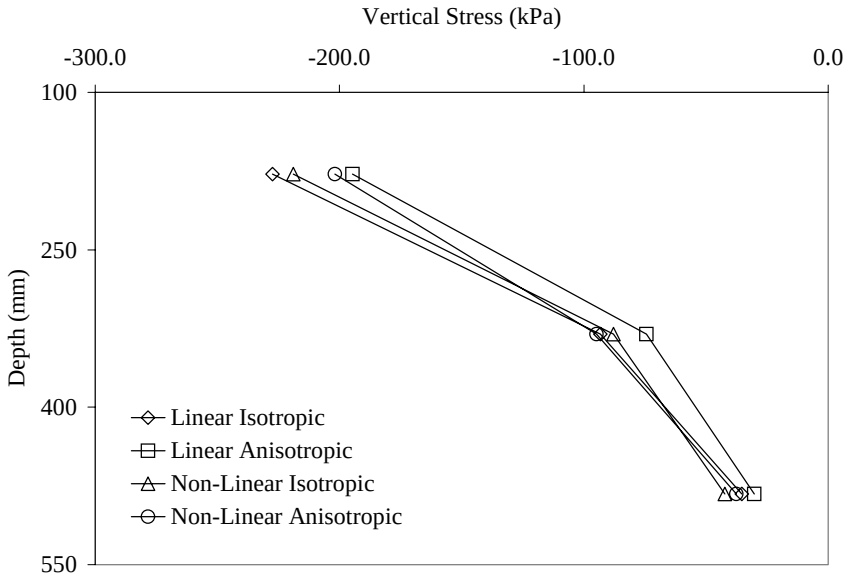

Figure 73. Vertical Stress for 100-mm HMA, 450-mm Base and 20.7-MPa Subgrade.

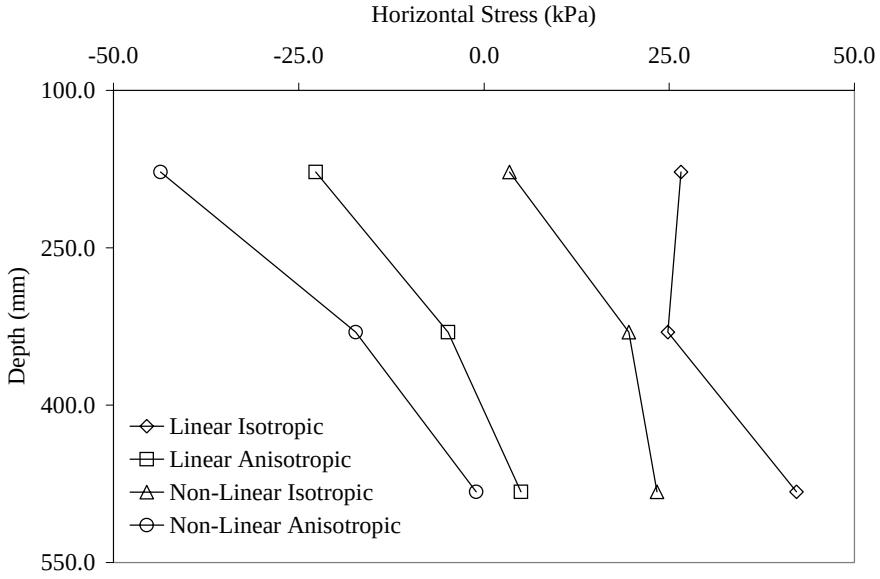

Figure 74. Horizontal Stress for 100-mm HMA, 450-mm Base and 20.7-MPa Subgrade.

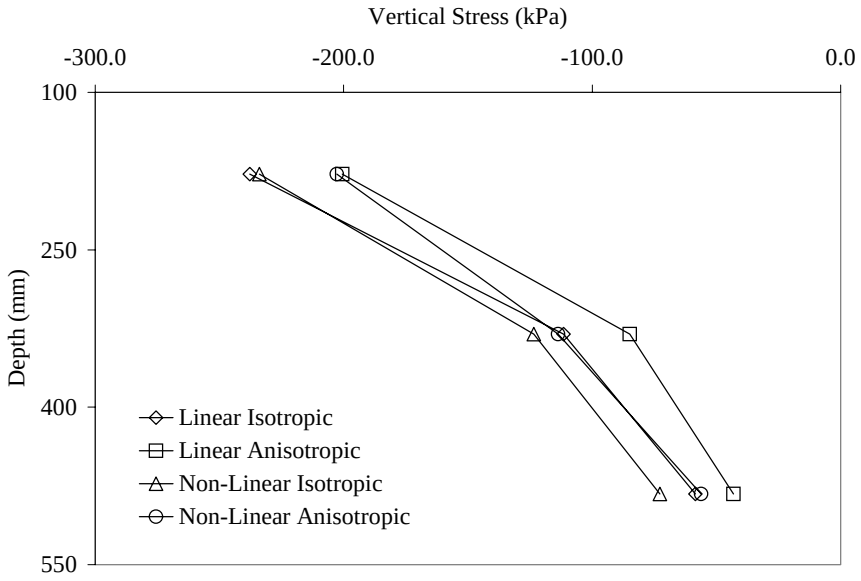

Figure 75. Vertical Stress for 100-mm HMA, 450-mm Base and 103.4-MPa Subgrade.

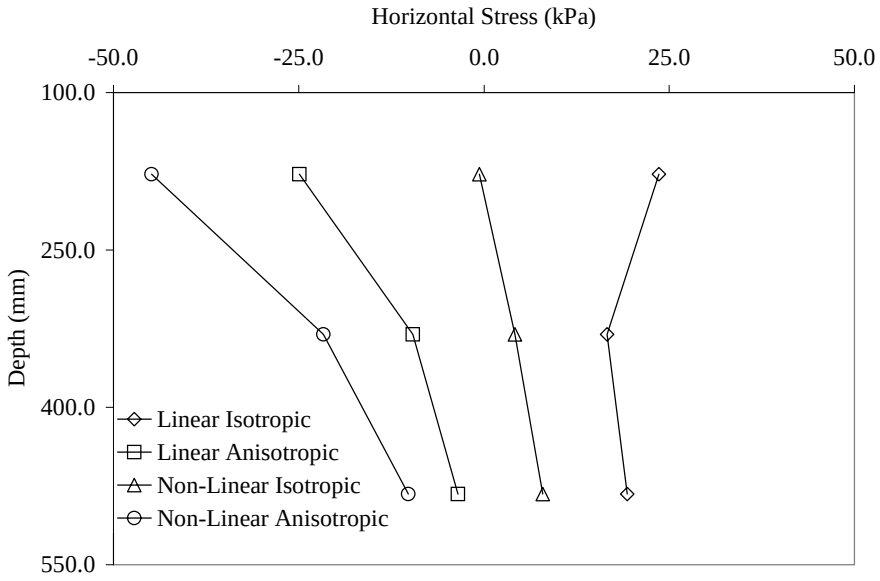

Figure 76. Horizontal Stress for 100-mm HMA, 450-mm Base and 103.4-MPa Subgrade.

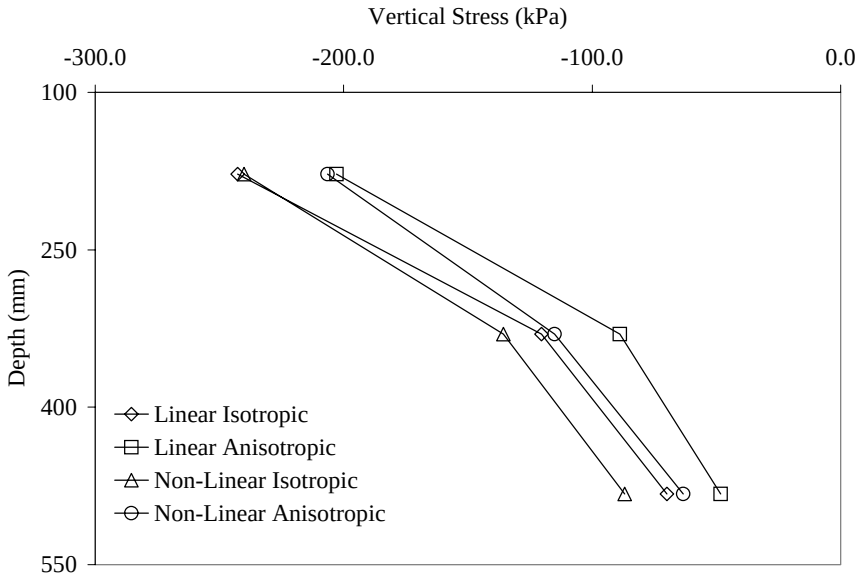

Figure 77. Vertical Stress for 100-mm HMA, 450-mm Base and 206.8-MPa Subgrade.

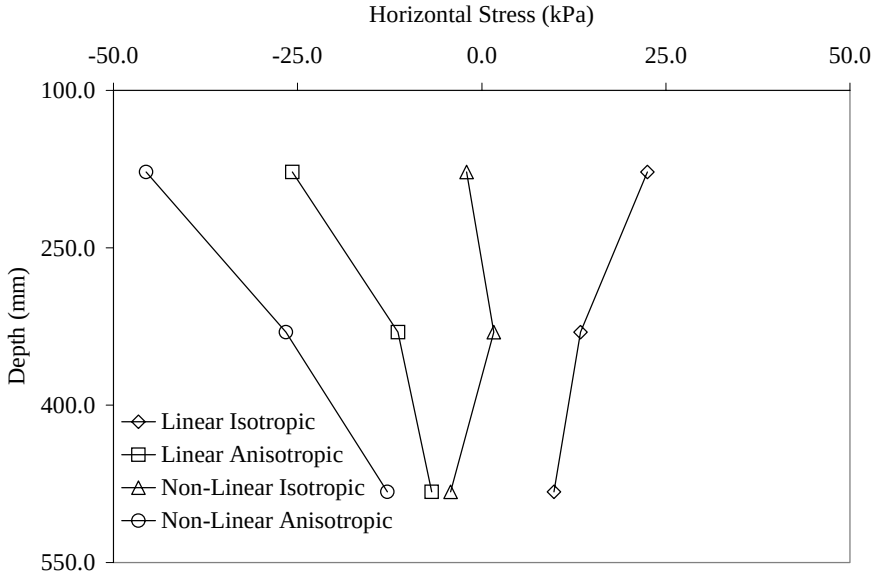

Figure 78. Horizontal Stress for 100-mm HMA, 450-mm Base and 206.8-MPa Subgrade.

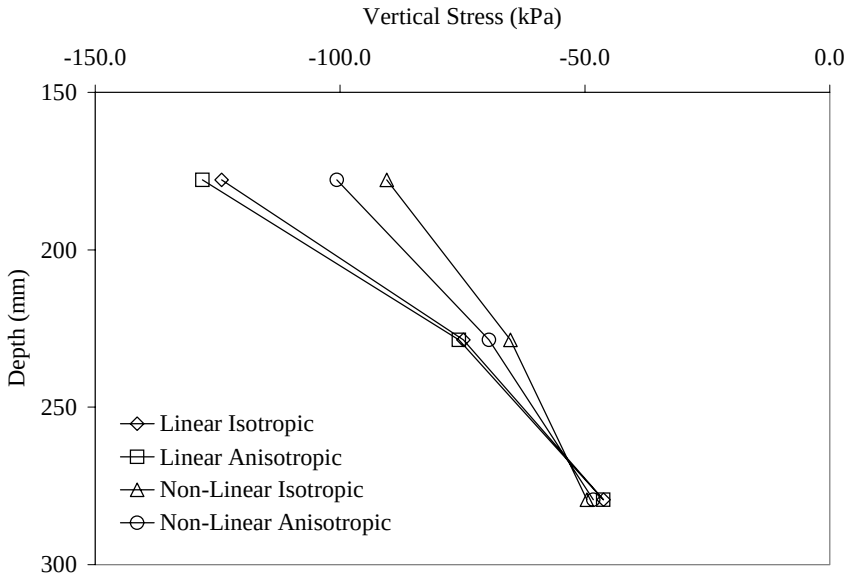

Figure 79. Vertical Stress for 150-mm HMA, 150-mm Base and 20.7-MPa Subgrade.

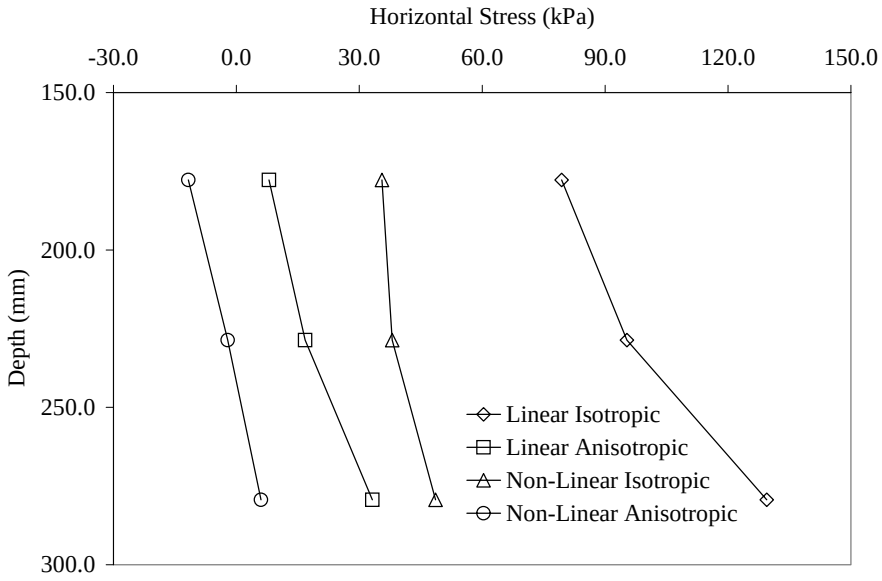

Figure 80. Horizontal Stress for 150-mm HMA, 150-mm Base and 20.7-MPa Subgrade.

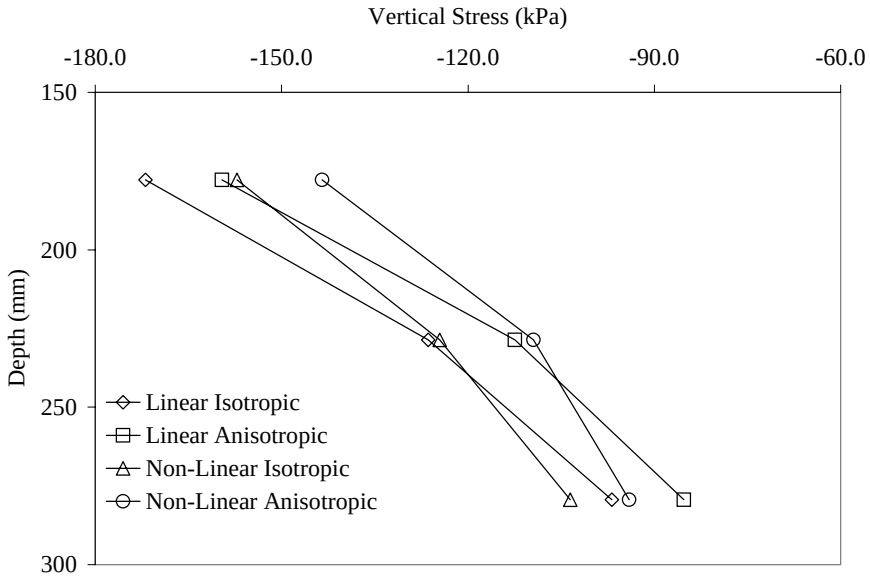

Figure 81. Vertical Stress for 150-mm HMA, 150-mm Base and 103.4-MPa Subgrade.

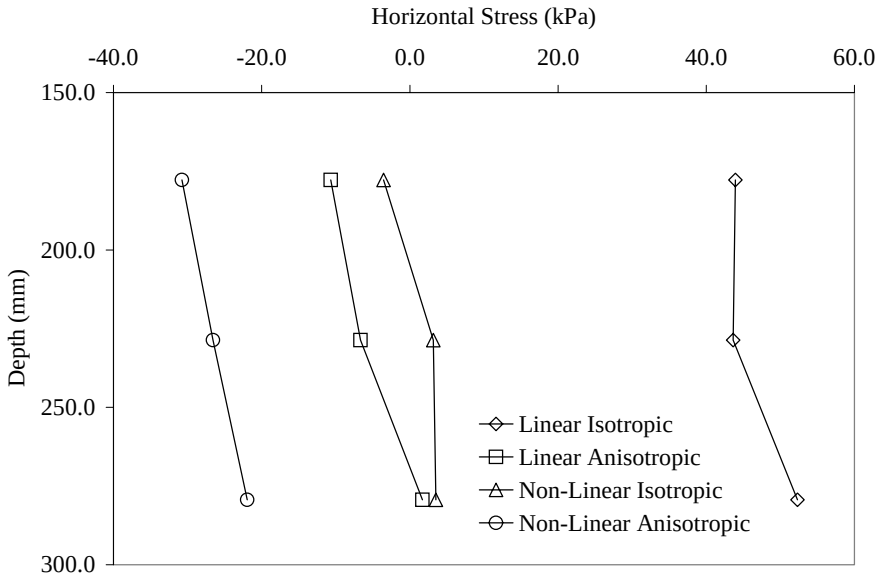

Figure 82. Horizontal Stress for 150-mm HMA, 150-mm Base and 103.4-MPa Subgrade.

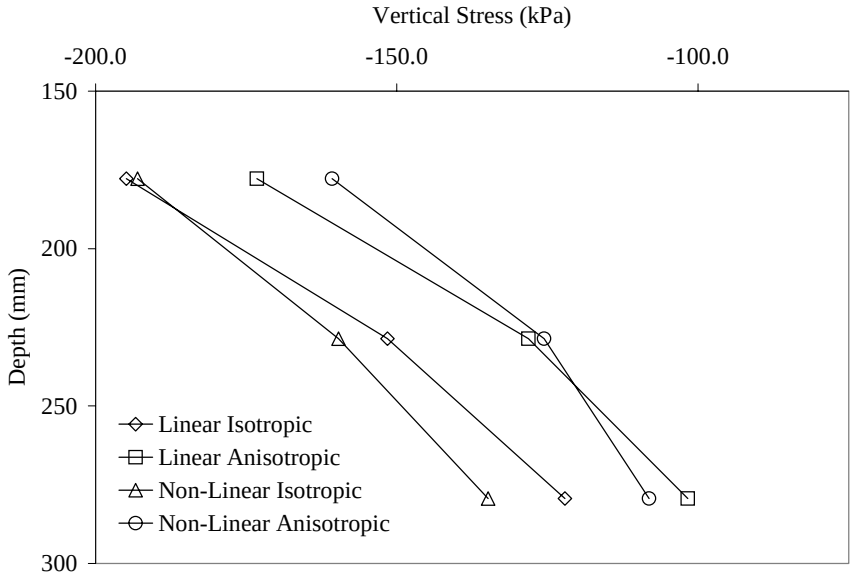

Figure 83. Vertical Stress for 150-mm HMA, 150-mm Base and 206.8-MPa Subgrade.

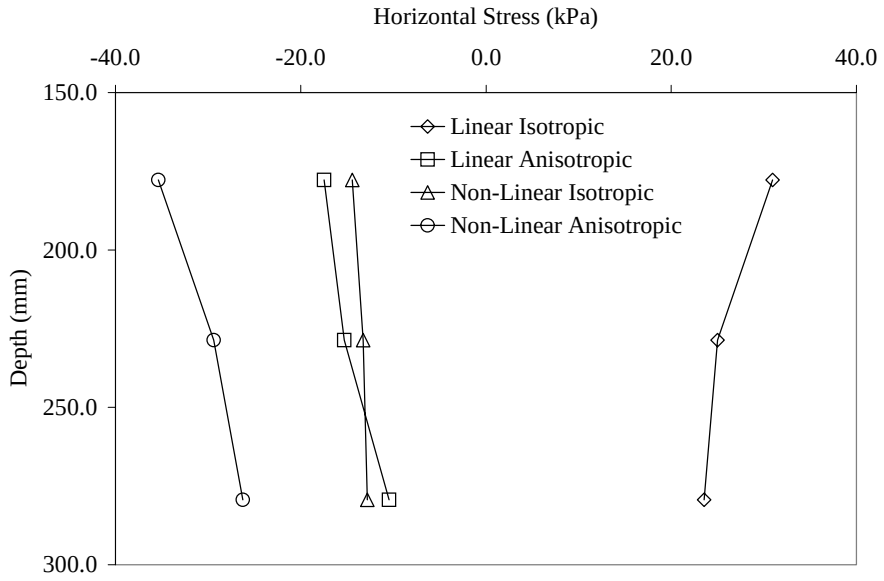

Figure 84. Horizontal Stress for 150-mm HMA, 150-mm Base and 206.8-MPa Subgrade.

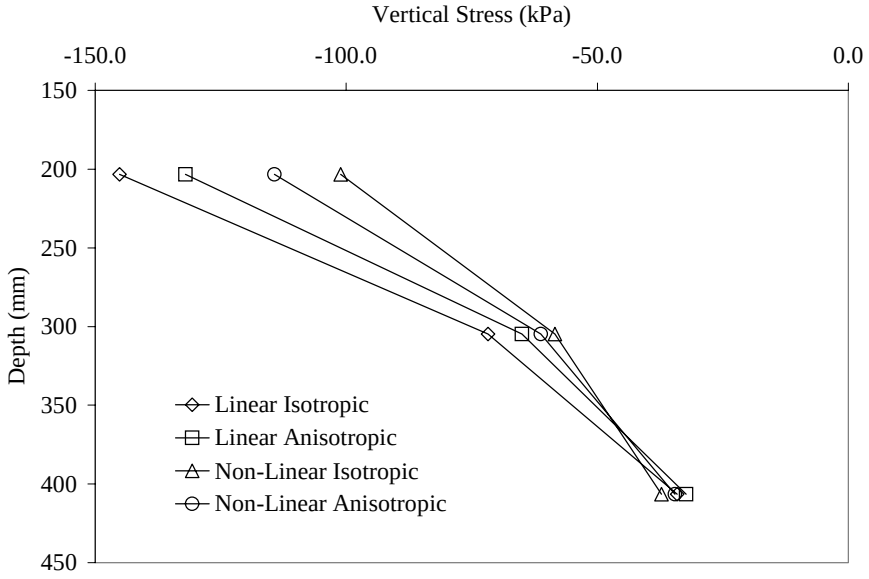

Figure 85. Vertical Stress for 150-mm HMA, 300-mm Base and 20.7-MPa Subgrade.

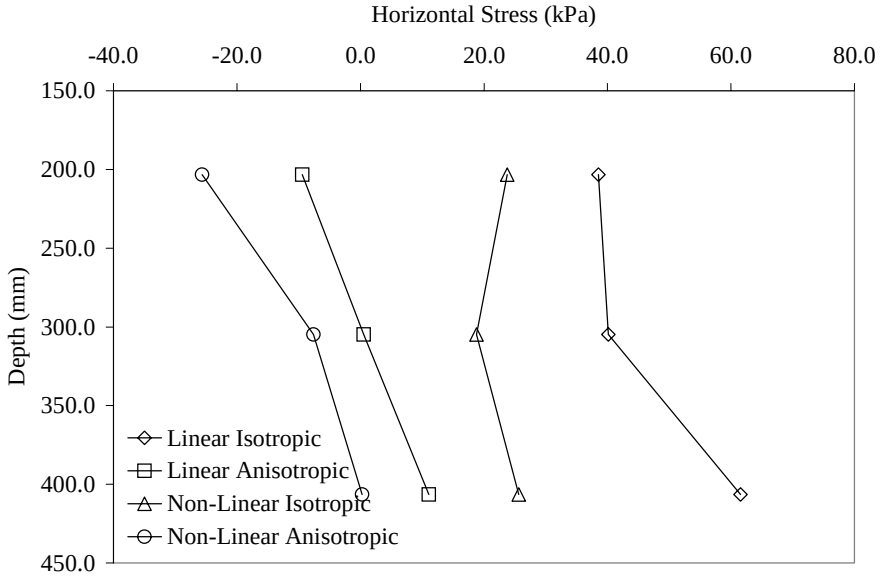

Figure 86. Horizontal Stress for 150-mm HMA, 300-mm Base and 20.7-MPa Subgrade.

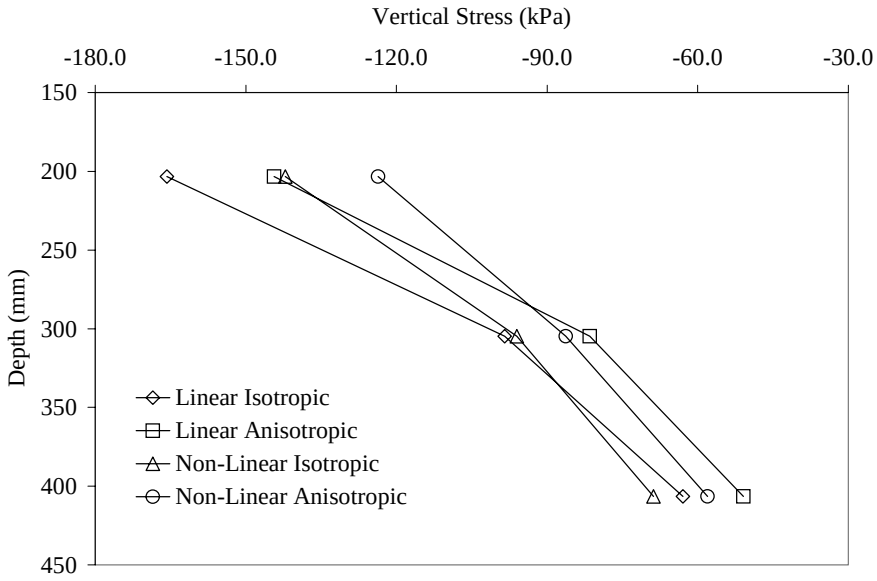

Figure 87. Vertical Stress for 150-mm HMA, 300-mm Base and 103.4-MPa Subgrade.

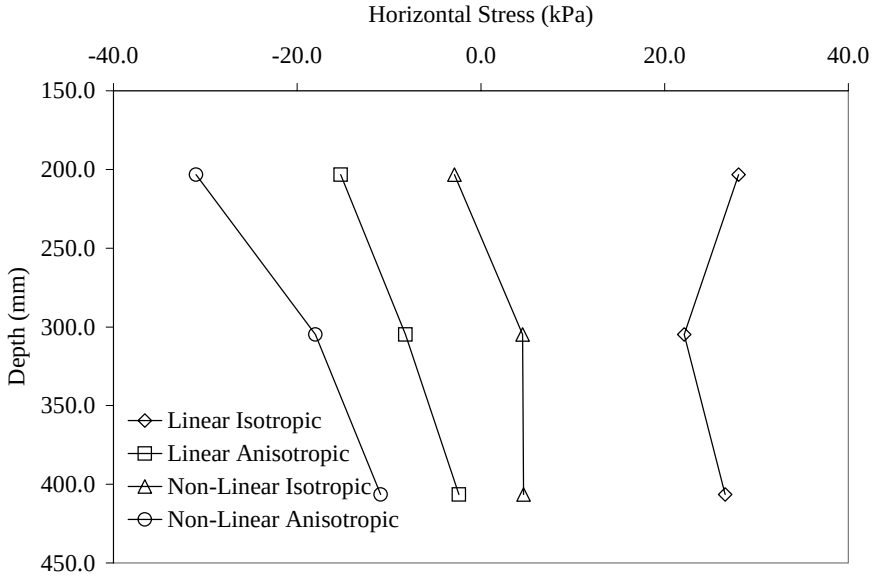

Figure 88. Horizontal Stress for 150-mm HMA, 300-mm Base and 103.4-MPa Subgrade.

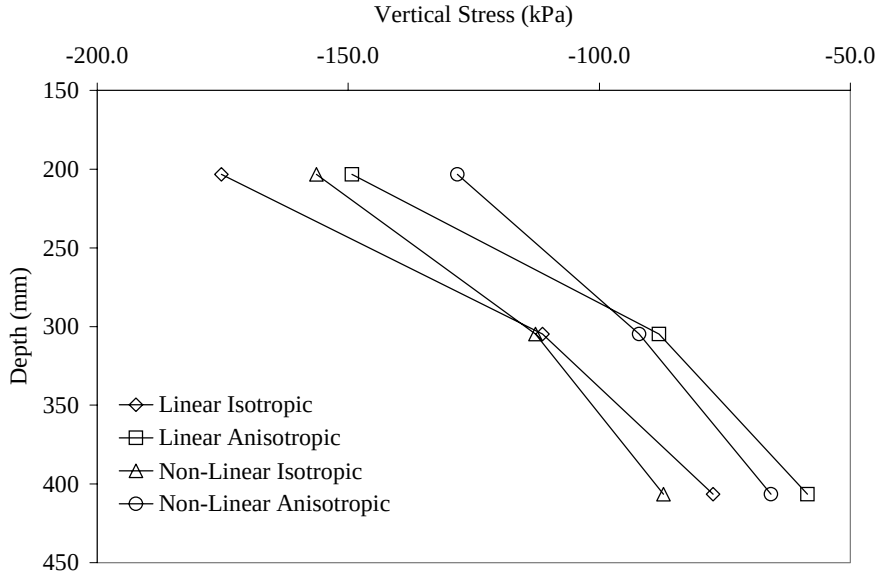

Figure 89. Vertical Stress for 150-mm HMA, 300-mm Base and 206.8-MPa Subgrade.

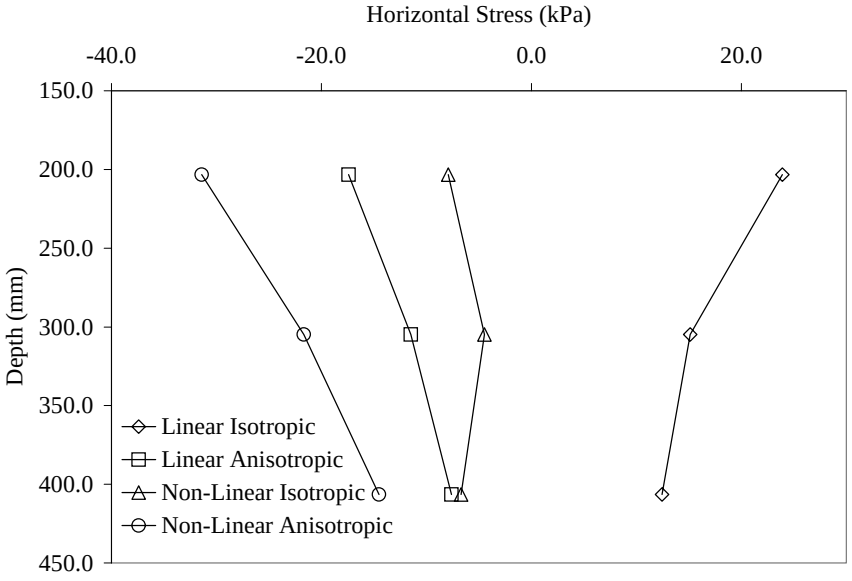

Figure 90. Horizontal Stress for 150-mm HMA, 300-mm Base and 206.8-MPa Subgrade.

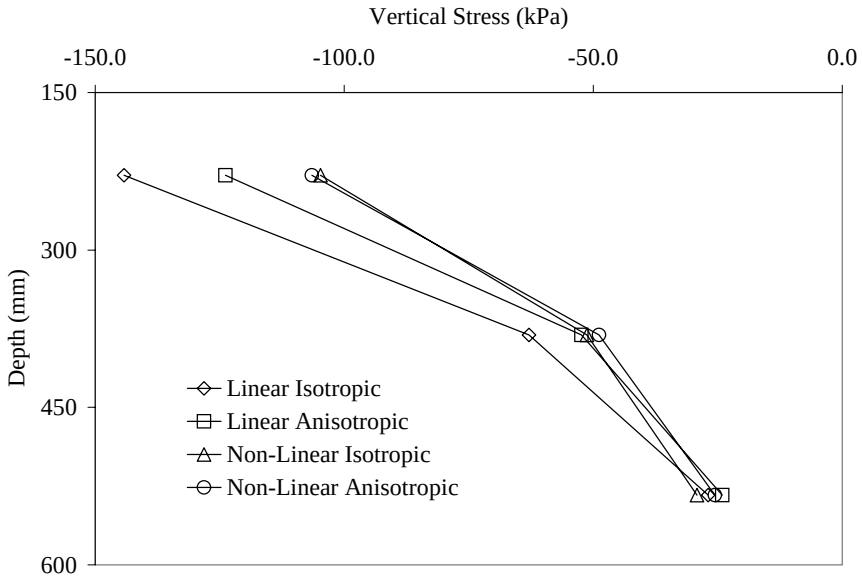

Figure 91. Vertical Stress for 150-mm HMA, 450-mm Base and 20.7-MPa Subgrade.

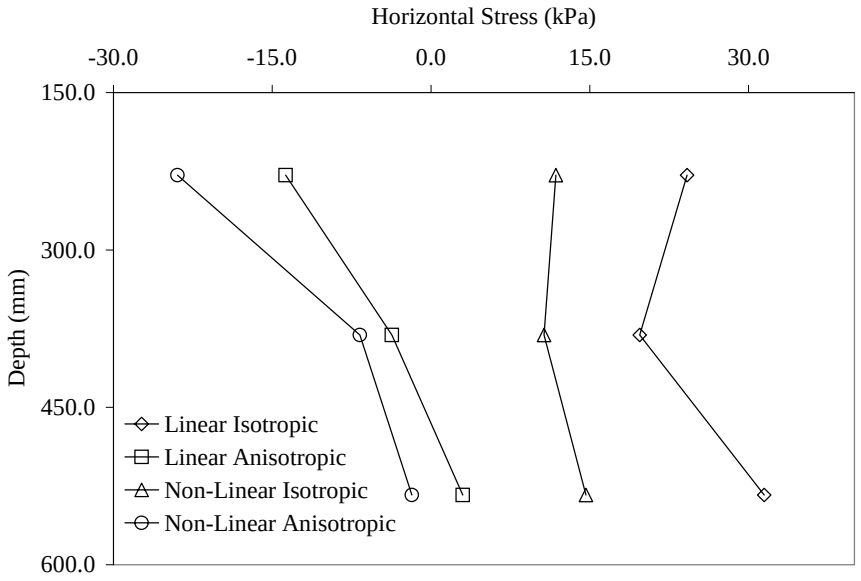

Figure 92. Horizontal Stress for 150-mm HMA, 450-mm Base and 20.7-MPa Subgrade.

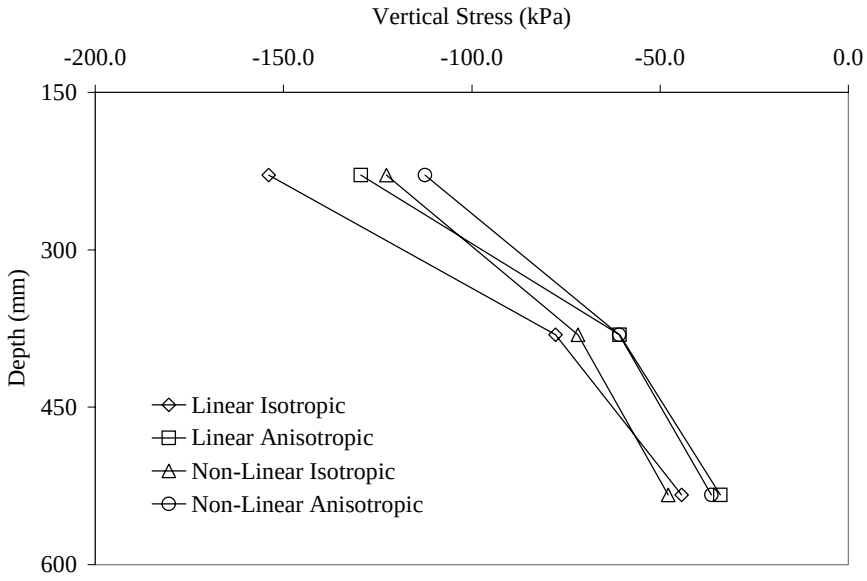

Figure 93. Vertical Stress for 150-mm HMA, 450-mm Base and 103.4-MPa Subgrade.

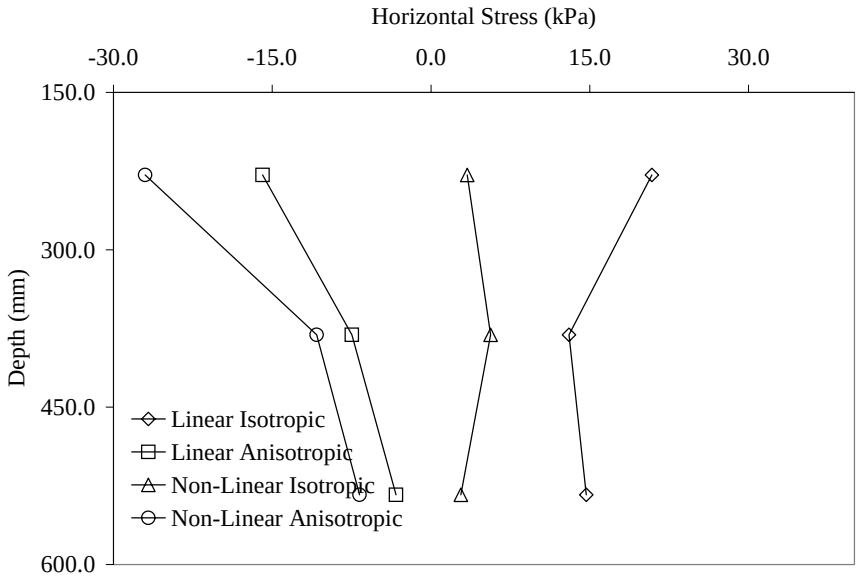

Figure 94. Horizontal Stress for 150-mm HMA, 450-mm Base and 103.4-MPa Subgrade.

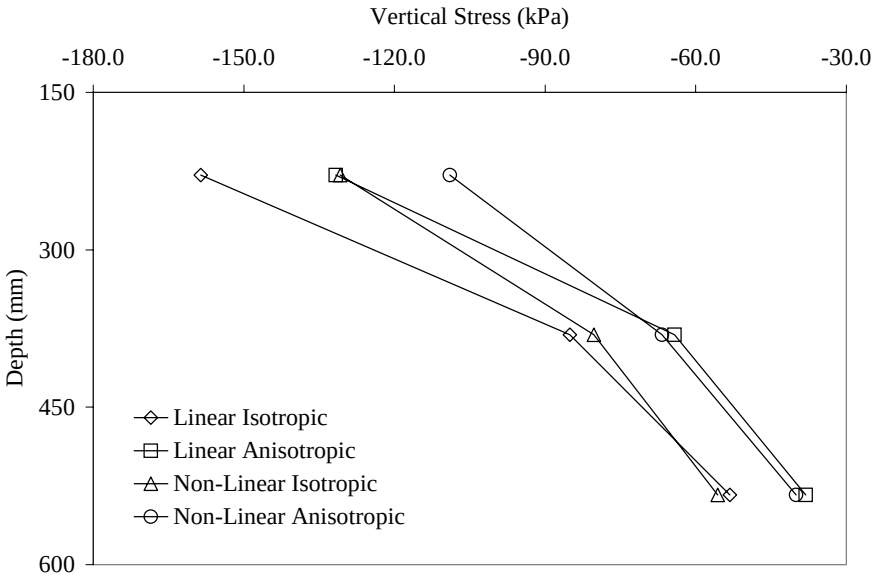

Figure 95. Vertical Stress for 150-mm HMA, 450-mm Base and 206.8-MPa Subgrade.

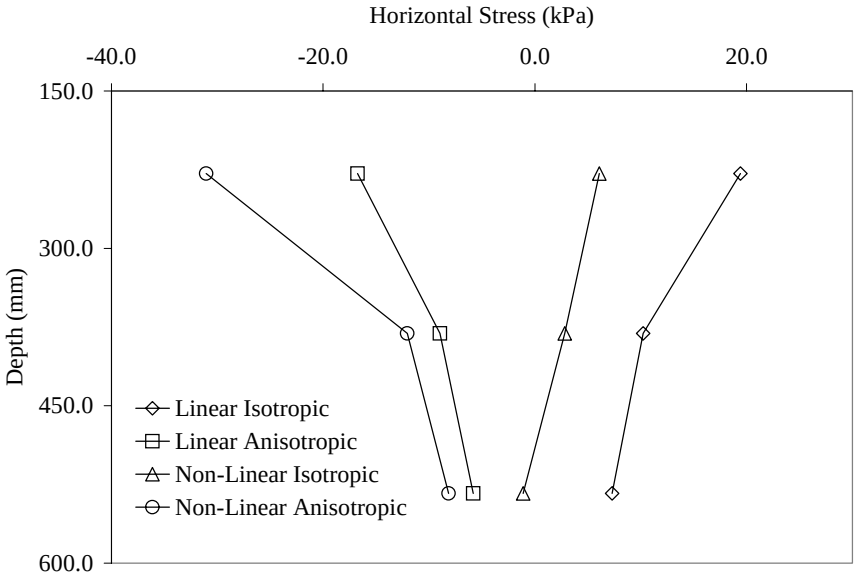

Figure 96. Horizontal Stress for 150-mm HMA, 450-mm Base and 206.8-MPa Subgrade.